THESIS

3D LOCALIZATION OF CYTOSKELETON IN MOUSE SPERMATIDS USING STOCHASTIC OPTICAL RECONSTRUCTION MICROSCOPY

Submitted by

Reshma Sunny

Department of Electrical and Computer Engineering

In partial fulfillment of the requirements

For the Degree of Master of Science

Colorado State University

Fort Collins, Colorado

Fall 2022

Master's Committee:

Advisor: Diego Krapf

Mahdi Nikdast
Ashok Prasad

ABSTRACT

3D LOCALIZATION OF CYTOSKELETON IN MOUSE SPERMATIDS USING STOCHASTIC OPTICAL RECONSTRUCTION MICROSCOPY

It is estimated by the World Health Organization that globally 186 million individuals live with infertility. Studies have shown that cause of male infertility is unknown in 30 to 50% of the cases. Over the last several years teratozoospermias have been investigated and have been backtracked to events in spermatogenesis. The development of the acrosome and the manchette, protein and vesicle transport in spermatids, and sperm head shaping are crucial steps in the formation of healthy sperms. The cytoskeleton in spermatids plays a crucial role in shaping the sperm head. The acroplaxome exerts forces on the nucleus and gives the mammalian sperm head its species-specific shape, and also facilitates the proper attachment of the nuclear cap called the acrosome, containing the enzymes required for sperm penetration of the oocyte. The manchette should be intact and formed properly to have shortened diameter as spermatids differentiate so that it can constrict the base of the nucleus to shape the head, and also facilitate the transport of cargo to the base of the cell. Thus as studies have confirmed, the disruption in the organization of the cytoskeleton is a concern for infertility. Hence it is crucial to learn more about the cytoskeletal structures in spermatids. The goal of this thesis is to 3D localize these structures.

The major structures we are interested in are the acroplaxome and the manchette. For this, we use a super-resolution microscopy method called Stochastic Optical Reconstruction Microscopy to image spermatid cytoskeleton. Our experiments confirmed the presence of α-tubulin in the manchette and that of F-actin in the manchette and the acroplaxome, as previously observed by researchers with 2D confocal images. We observed that the manchette reduces in diameter and progresses to the caudal portion of the cell at the later steps of differentiation and that the structure forms completely at step 10 and disassembles after step 14.

ACKNOWLEDGEMENTS

I would like to express my sincere gratitude to Dr. Diego Krapf for granting me the opportunity to be a part of his lab and work on an exciting project. Thank you for your kind guidance, for sharing your knowledge and guiding me through my research journey.

To Carsten, thank you for being a wonderful mentor, for being patient with me and for lifting my spirits when things go south.

I would not have made this far without the love and support of my dear friends. Thank you, Pratiksha Baishya, Daniela Ramos, Aundrea Dugas, Dale Grenfell, Laurel Bond, Marcie Stewart, Majka Philips and Neetha John.

A huge thanks to Dr. Maria Eugenia Teves for collaborating with me and helping me during the period of research and writing my thesis. I would like to thank Dr. Mahdi Nikdast and Dr. Ashok Prasad for being part of my committee and for their patience and support.

My deepest gratitude goes to my family for listening to my rants irrespective of the time difference and for not losing their faith in me.

DEDICATION

I would like to dedicate this thesis to my sister Mahima. You are my guiding light and role model

TABLE OF CONTENTS

ABSTRACT ii
ACKNOWLEDGEMENTS iii
DEDICATION iv
LIST OF FIGURES vii

Chapter 1 Introduction 1
- 1.1 Spermatogenesis 1
- 1.2 Cytoskeleton in spermatids 5
  - 1.2.1 Acroplaxome 5
  - 1.2.2 Manchette 7
  - 1.2.3 Role of cytoskeleton in nuclear remodeling and shaping of sperm head . 8
- 1.3 Super-resolution imaging 10
  - 1.3.1 Diffraction limit 10
  - 1.3.2 Stochastic Optical Reconstruction Microscopy 11
  - 1.3.3 Astigmatism method 15

Chapter 2 3D Localization of α tubulin in spermatids 16
- 2.1 Introduction 16
- 2.2 Materials and methods 17
  - 2.2.1 Sample collection 17
  - 2.2.2 Fixing samples 17
  - 2.2.3 Immunostaining samples by indirect immunofluorescence 18
- 2.3 Instrumentation and software 19
  - 2.3.1 Aligning TIRF microscope 19
  - 2.3.2 3D STORM imaging set-up 19
  - 2.3.3 Calibrating the MicAO 20
  - 2.3.4 Image acquisition 22
  - 2.3.5 Obtaining look-up table 22
  - 2.3.6 3D STORM Reconstruction of images 23
- 2.4 Results 24

Chapter 3 3D Localization of phalloidin stained actin in spermatids 31
- 3.1 Introduction 31
- 3.2 Materials and methods 33
  - 3.2.1 Sample collection 33
  - 3.2.2 Immunostaining samples by indirect immunofluorescence 33
- 3.3 Instrumentation and software 33
- 3.4 Results 33

Chapter 4 Conclusion and Future work 37

Bibliography 39
Appendix A Coating coverslips with Poly-L-lysine 48
Appendix B Preparing GLOX 49
Appendix C Collecting and fixing spermatid cells from mice 50
Appendix D Labelling the cells- Immunostaining protocol 53
Appendix E Protocol for aligning a TIRF microscope 56
Appendix F 3D STORM Calibration Protocol 62
Appendix G Finding and imaging spermatid 72
Appendix H Obtaining look up tables for Astigmatism method 77
Appendix I STORM 3D Reconstruction Protocol 83

LIST OF FIGURES

1.1 Schematic representation of the mouse spermatogenic process from the base to the lumen of the seminiferous tubule 2
1.2 Schematic representation of mouse spermatogenesis 3
1.3 Schematic representation of the processes during spermiogenesis that are involved in sperm head shaping 6
1.4 Schematic representation of the manchette during spermiogenesis 9
1.5 Principle of STORM 11

2.1 Calibration curve generated for a group of 0.1 μm Tetraspeck microspheres 23
2.2 α tubulin structure in a mouse spermatid at step 10 25
2.3 Confocal images of step 10 spermatid 25
2.4 α tubulin structure in a mouse spermatid at step 11 26
2.5 Confocal images of step 11 spermatid 26
2.6 α tubulin structure in the captured section of a mouse spermatid at step 12 28
2.7 Confocal images of step 12 spermatid 28
2.8 α tubulin structure in a mouse spermatid at step 14 29
2.9 Confocal images of step 14 spermatid 29
2.10 α tubulin structure in a mouse spermatid at step 15 30

3.1 2D confocal image of F-actin in step 14 spermatid 34
3.2 Actin structure in mouse spermatid at step 10 35
3.3 Actin structure in mouse spermatid at step 11 35
3.4 Actin structure in mouse spermatid at step 12 35
3.5 Actin structure in mouse spermatid at step 13 36

E.1 Components of TIRF microscope. 56
E.2 The shared path of LASERs – “main line” 58
E.3 Positioning the crosshair for reference 59
E.4 Laser beam in close to TIRF 60

F.1 Imaging settings for obtaining PSF 64
F.2 MicAO settings to obtain PSF without aberrations 65
F.3 Gain and exposure settings for calibration 66
F.4 Mirror shape in MicAO 67
F.5 Settings for obtaining PSF 68
F.6 Astigmatism settings in MicAO 68
F.8 Settings to capture calibration movies 70

G.1 Time series settings for imaging cells 72
G.2 CRISP Autofocus settings 74
G.3 ASI MFC 2000 75

H.1 Coverting .nd2 to .tiff file 78

H.2 Importing tiff files for calibration 79
H.3 Navigating to cylindrical lens calibration 79
H.4 Camera settings for calibration 80
H.5 Settings to run 3D calibration 80
H.6 Calibration preview 81
H.7 Path to save .yaml file 82
H.8 Sigma curve 82

I.1 Importing data to ThunderSTORM 83
I.2 Path to Run analysis 84
I.3 Camera setup for reconstruction 85
I.4 General settings for 3 D reconstruction 85
I.5 Normalized Gaussian 86
I.6 Preprocessing Look-up-table 87
I.7 Removing duplicates from the initial reconstruction data 88
I.8 Plot histogram of reconstructed data 88
I.9 z distribution of the reconstructed data 88
I.10 Coarse z filtering 89
I.11 Visualization of filtered data with stacks in different z height 89
I.12 Drift correction 91
I.13 Density filter settings 92
I.14 Merging of post processed data 92
I.15 Exporting post processed data 92
I.16 Exporting post processed stack of data viewed as Normalized Gaussian as .tiff file . . . 93
I.17 3D projection settings 93

Chapter 1

Introduction

It is imperative to have good quality and quantity of sperm for successful fertilization. Conditions that cause abnormal sperm shapes solely or simultaneously in the head, neck, midpiece and tail are called teratozoospermia [1]. One of the most common and severe cases of teratozoospermia in humans is globozoospermia where the sperm head is round instead of the typical oval shape. This condition may also accompany by a complete lack of acrosome. The acrosome contains the necessary enzymes to penetrate the zona pellucida layer of the female oocyte. It is difficult for a round sperm head to penetrate the egg, especially without the enzymes to traverse through the membranes of the oocyte [2]. Several events of spermatogenesis have to be perfectly aligned to ensure a typically shaped and healthy sperm. The process of spermatogenesis occurs in the testis in a compartment called the seminiferous tubule, which has a complex epithelium and fluids. Sertoli cells are a group of its epithelial cells that provide support and nutrition to the developing germ cells. Due to its crucial role in the normal progression of spermatogenesis, germ cells cannot be successfully developed in vitro in a culture dish. Since mice have a very similar genome to humans and hence have many genetic defects identical to humans, mouse models are used to study the causes of male infertility [3]. It is to be noted that mouse spermatids have hook-shaped heads, unlike human spermatids.

The following sections discuss the process of spermatogenesis, the cytoskeletal structures that are crucial in ensuring fertility, and the super-resolution method we use to localize the cytoskeleton in spermatids.

1.1 Spermatogenesis

Spermatogenesis is a complex process by which primordial germ cells develop into spermatozoa. The process advances from the base of the seminiferous tubule to its lumen while in constant contact with Sertoli cells, as seen in fig1.1. Spermatogenesis is initiated at puberty and is characterized into three distinct phases. The first phase is the proliferative phase, where spermatogonial stem cells (SSC) undergo mitotic division to form undifferentiated spermatogonia to replenish its population and differentiated spermatogonia for the production of sperm cells. The self-renewing ability of SSCs ensure continuous production of spermatozoa [3]. Proliferation ends in a premeiotic DNA replication resulting in primary spermatocytes.

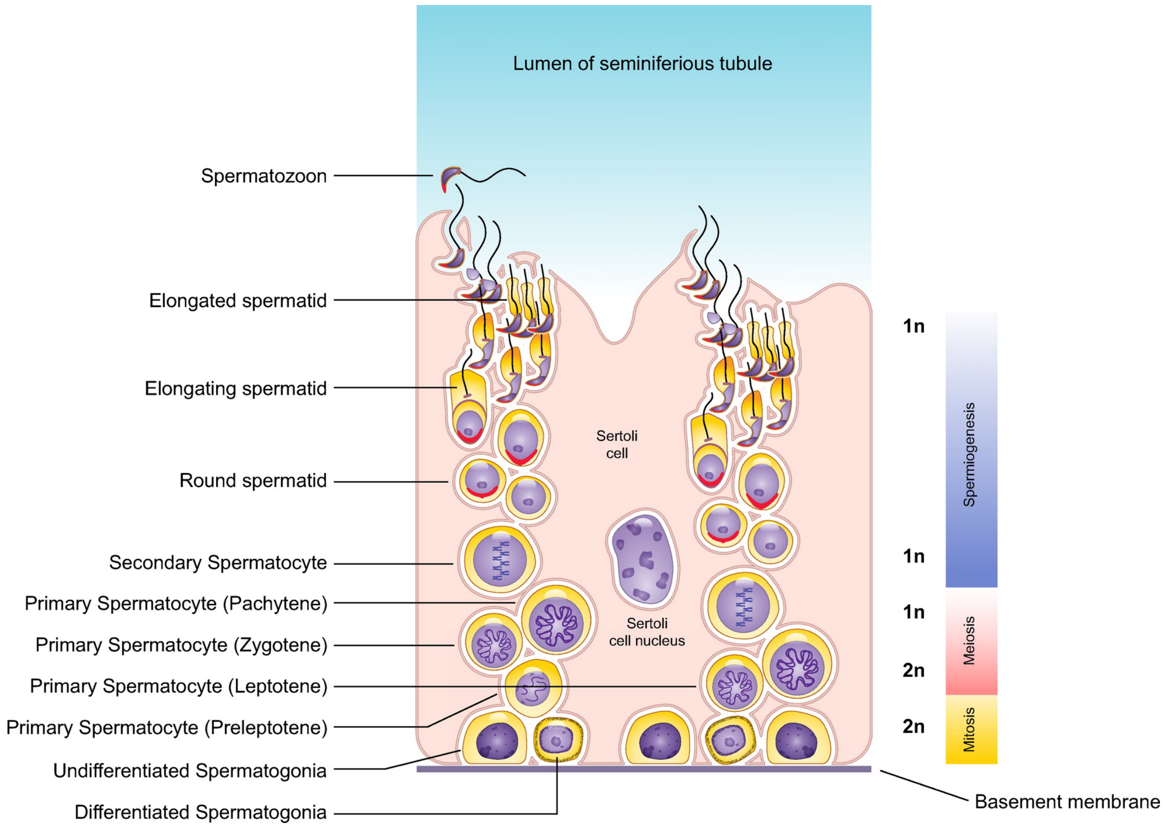

Figure 1.1: Schematic representation of the mouse spermatogenic process from the base to the lumen of the seminiferous tubule. Spermatogonia lies in the base and by proliferating produces different types of primary spermatocytes. The secondary spermatocytes are further down towards the lumen and undergo two meiosis to become round spermatids. Spermiogenesis occurs next and spermatids differentiate. From step 8, the spermatids elongate and towards the end of spermiation, most of the cytoplasm is removed from the cell, and fully developed spermatozoa leave the lumen of the seminiferous tubule. The figure was taken from Teves and Rolden 2021 [4] and used under Creative Commons Attribution CC by 4.0.

The second phase of spermatogenesis is meiosis. In the first meiotic division, the primary spermatocyte goes through a long prophase including preleptotene, leptotene, zygotene and pachytene stages, each later stage occurring farther down the seminiferous tubule than the one before. The

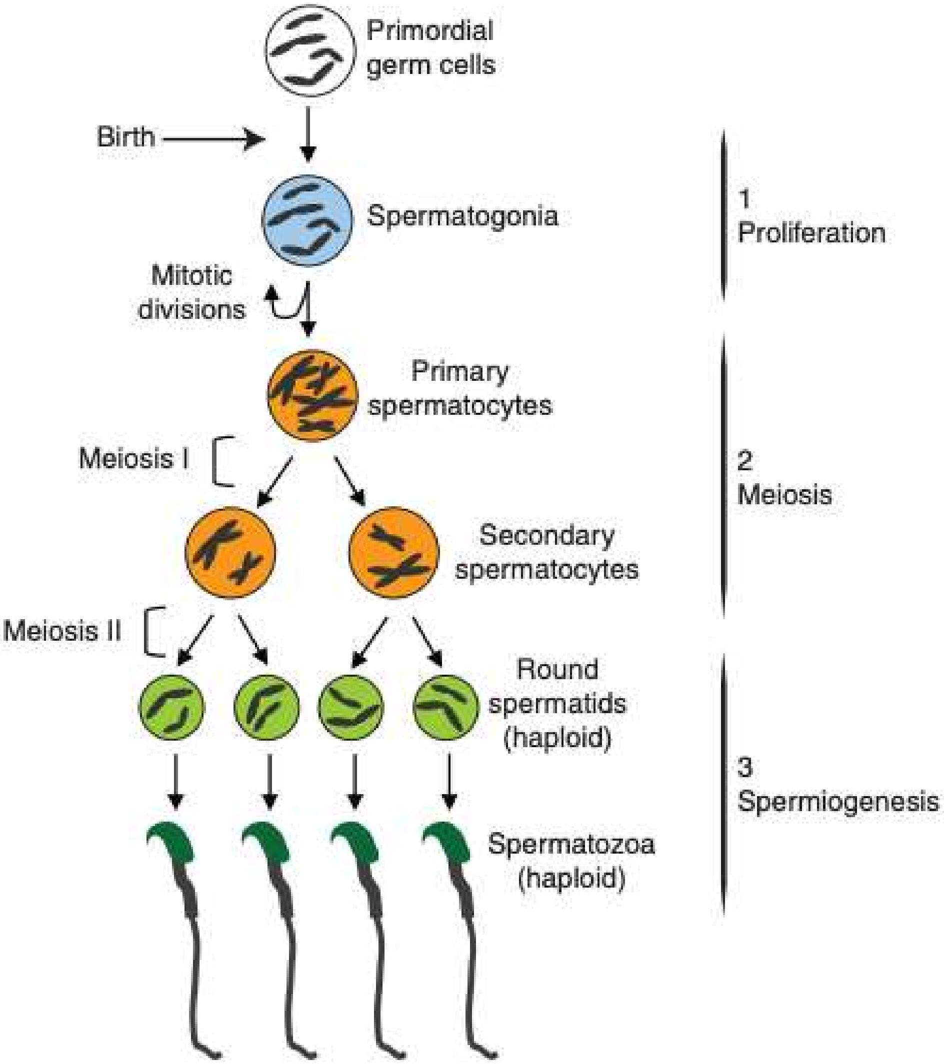

Figure 1.2: Schematic representation of mouse spermatogenesis. Spermatogonial stem cells undergo mitosis and both self renews its population as well as provide cells for further differentiation. Spermatocytes undergo multiple meiotic divisions to generate haploid round spermatids, which undergo differentiation and remodels into streamlined spermatozoa with a species-specific head shape and acrosome and flagella [3]

chromosomes condense, pairs, synapses and undergo genetic recombination. At the end of the first meiosis, two tetraploid secondary spermatocytes are formed. They undergo a shorter meiosis and produces two haploid round spermatids, as shown in fig 1.2. The third and last phase of spermatogenesis is called spermiogenesis or spermatid differentiation. There are 16 steps in mouse spermiogenesis, where steps 1-7 is the round spermatid phase and 8-16 is the spermatid elongation phase. The elongated spermatids follow spermiation and leave the lumen of the seminiferous tubule, as shown in fig 1.1. The spermatid differentiation consists of many complex events that structurally and functionally change the cell [3, 4]. The formation of acrosome is one of the earliest events and is called acrosome biogenesis. It is divided into different phases. The first phase called the Golgi phase extends from steps 1-3. During the Golgi phase, the pro-acrosomal vesicles are trafficked from trans-Golgi sacs and the endocytic pathway forming the acrosomal granule near the nucleus. Studies have shown that the correct spatial orientation of the Golgi sacs is facilitated by microtubules. This coincides with our knowledge of eukaryotic vesicle trafficking that it is mediated by microtubules for long-range movements and actin-based networks for short-range [5]. The next phase that extends in steps 4-7 is called the cap phase, where the acrosomal granule grows and spreads over one-third of the nuclear membrane. Next is the acrosomal phase, where the acrosome migrates to the ventral side of the nucleus, condenses and binds to the inner acrosomal membrane. The last phase that extends from steps 13-16 is called the maturation phase [6]. Here, the acrosomal granule spreads throughout the acrosomal membrane and the acrosome differentiates to form the acrosome apex at the anterior, and cover the width of the nuclear surface at the posterior. These four phases that involve in the formation of each pro-acrosomal vesicle, transport, attaching to the nuclear region and expansion of acrosome, all depend on the F-actin and microtubule-based networks and the proteins associated with them, and the failure in any of these steps lead to globozoospermia [7, 8]. Another event that occurs during spermatogenesis is the nuclear modeling. The round spermatids in steps 1-7 have a central spherical nucleus and de-condensed chromatin. The shaping of the nucleus is done by the actin hoops of the Sertoli cell and cytoskeletal structures called the acroplaxome and the manchette, both of which will be discussed in the next section. Flagellar formation starts simultaneously with acrosome formation. The centrosome inherited during meiosis migrates to the caudal pole of the cell and one of its two centrioles forms the axoneme structure at the ventral portion of the cell [9]. Mitochondria from the cytoplasm forms the helix at the middle piece of the flagellum and a fibrous sheath forms at the principal piece of the cell after the axoneme growth is completed. The proteins are moved to the base of the sperm tail by intramanchette transport.

1.2 Cytoskeleton in spermatids

In eukaryotes, the cytoskeleton is composed of microtubules, intermediate filaments and microfilaments or actin filaments, all of which provide infrastructure for biological function and motility. The filaments form a vast geometrical network by cross-linking and undergo deformation to establish cell connections and participate in cellular activities. Microtubules are made of α and β tubulin heterodimers bound together to form clusters of straight and polar trusses. Various microtubule-associated proteins like kinesin and dynein are present to ensure the timely performance of functions such as cross-linking and cargo transport. Microfilaments are assembled by globular actin forming a bifilar helix called F-actin or filamentous actin and along with their microfilament proteins like myosin, impact cellular functions and multiple stages of spermatogenesis [2].

1.2.1 Acroplaxome

Kierszenbaum et al. [10] first observed that a cytoskeletal plate containing F-actin and keratin anchors the developing acrosome to the nuclear envelope in rat spermatids. They designated the plate as acroplaxome and observed that it consists of a marginal ring made of 10 nm thick intermediate filaments that inserts into a dense plaque associated with the leading edge of the inner acrosomal membrane. It contains a second plaque opposite to the intermediate filament-plaque complex and is linked to the nuclear lamina [11, 12]. Linker of nucleoskeleton and cytoskeleton (LINC) complexes bridge the nuclear lamina to the F-actin in the acroplaxome [8]. It was observed in later experiments [11] that during the nuclear modelling, the acroplaxome fastens the caudal re-

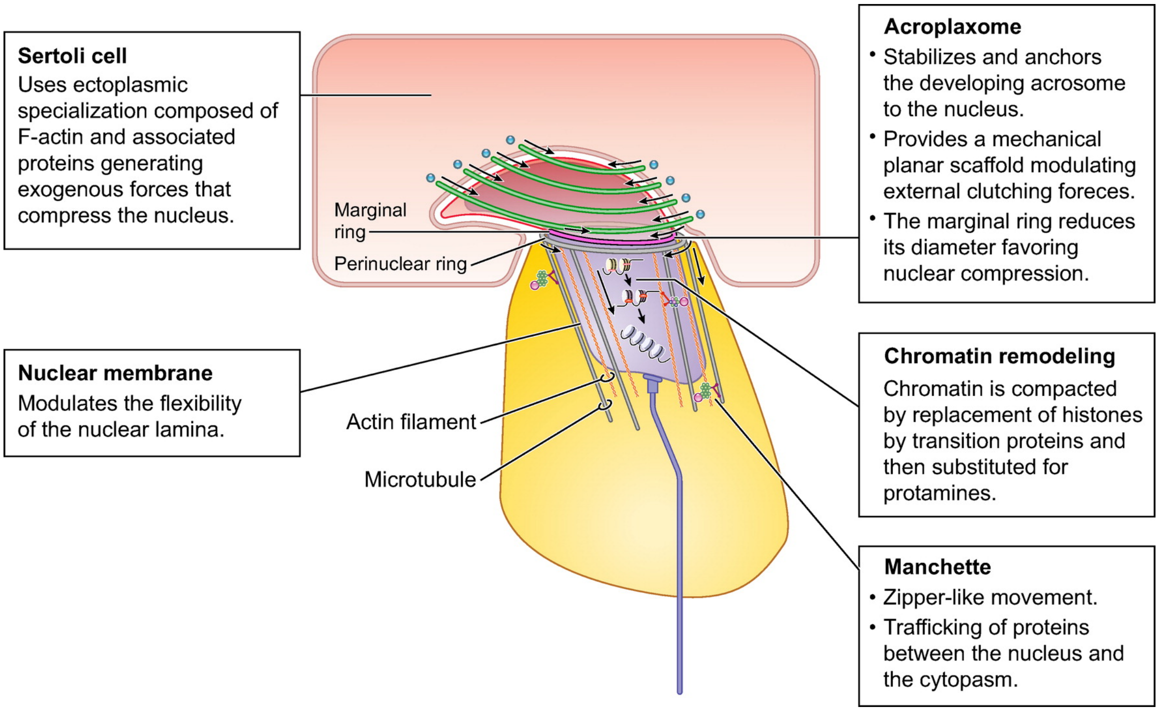

Figure 1.3: Schematic representation of the processes during spermiogenesis that are involved in sperm head shaping. The figure was taken from Teves and Rolden 2021 [4] and used under Creative Commons Attribution CC by 4.0. The F-acting containing hoops are ectoplasmic specializations in the Sertoli cell and generates external forces. The structure covers more than one-third of the spermatid head. The acroplaxome modulates the forces generated by the F-acting containing hoops. The manchette encircles the remaining two-thirds of the nuclear region and generates internal forces due to zipper-like movement. The molecular composition of the nuclear membrane is restructured to allow the nuclear membrane to be flexible to the external and internal forces.

gion of the developing acrosome to the nuclear envelope. As discussed in the previous section, during acrosome biogenesis the acroplaxome facilitates the adhesion of pro-acrosomal vesicles to the nuclear membrane and their transverse spreading in the cap phase. Disruption in the production, transport or adhesion of these pro-acrosomal vesicles is a leading cause of male infertility like globozoospermia. It was also found by Kierszenbaum and collaborators [11] that myosin Va is a component of the acroplaxome and hypothesized that it drives the expansion of the leading edge of the acrosome and that during nuclear shaping, it facilitates in connecting the acrosome to the F-actin network. It also avoids the DNA damage during acrosome reaction by restraining forces [2]. Since its discovery, only few advances have been made to characterize the structure of the acroplaxome and its molecular mechanisms and is hence deserving further investigation [4].

1.2.2 Manchette

The manchette comprises of microtubules and actin filaments, as can be observed in fig 1.3. It assembles at the caudal site of acrosome-acroplaxome complex at spermatid step 8 after the acrosome formation starts and spermatids enter the elongation phase. It disappears at step 14 as the spermatid elongation is about to end and prior to the sperm tail mid-piece formation [13, 14]. The structure comprises of a dense perinuclear ring consisting of keratin and tubulin that assembles caudally to the proximity of the acroplaxomal marginal ring. Linear arrays of microtubules extend from the perinuclear ring, in parallel to the long axis of the nucleus, and cover the lower side of the nucleus [2, 5]. The short manchette microtubules that lie close to the nuclear membrane and the long ones that extend radially are periodically attached to each other through linkers to form a skirt-like structure [7]. The inner microtubules attach to the nuclear membrane through LINC complexes. The manchette assembly begins after the acroplaxomal marginal ring starts to organize. A groove forms at the circumference of the overlapping marginal ring and perinuclear ring, which also serves as the boundary for the F-actin grooves of Sertoli cells that holds the elongating spermatid head. The manchette encircles the lower portion of this elongating head, from the end of the acrosome to the region of the flagellum that is covered by the mitochondrial sheath [8]. The manchette performs three major tasks. Firstly, it expands by assembling diffused microtubules. Secondly, the microtubule-associated proteins cooperate with myosin to perform intramanchette transport (IMT). IMT provides tracks for the transport of proteins within the cytoplasm as well as between the nucleus and the cytoplasm [6]. Thirdly, it exerts contractive forces to shape the spermatid head, which will be discussed in the next subsection [2]. Intramanchette transport is bidirectional since kinesin act as the plus end and dynein act as the minus end directed motors on the manchette. The minus end motors serve for vesicle and protein movement down the manchette, as required in acrosome biogenesis and axoneme formation, and plus end motors for the movement up the manchette. Several experiments [10,15] confirmed β-actin and myosin-based vesicles in the manchette, thus leading to the speculations that F-actin-based transport also contributes to IMT. The cargos ferry for long distance (manchette to centrosome and axoneme) through microtubule-based tracks and short distance (Golgi to the acrosome) through actin-based tracks [11]. The manchette functions for flagellar formation by transporting the vesicles and proteins by IMT and also perform nuclear-cytoplasmic trafficking by connecting to the nuclear membrane by LINC complexes [2].

1.2.3 Role of cytoskeleton in nuclear remodeling and shaping of sperm head

The importance of sperm head shaping lies in the biological necessity of preserving the genome until the end of fertilization. During the spermatid differentiation or elongation process, the round spermatids will undergo a change in the nuclear shape and attain their species-specific head shape [2]. Kierszenbaum et al. [13] found a mouse model for head shaping and recognized two elements that the model relies on. The first one is the exogenous clutch which is the spatial arrangement of F-actin containing parallel hoops of the Sertoli cells that embrace one-third of the sperm head at its apex. The F-actin containing plaques can be mobilized in an up-and-down manner by the molecular motors linked to the microtubules at the ectoplasmic specialization site, thus generating exogenous forces that compress the nucleus. Fig 1.3 shows the F-actin hoop structures of the Sertoli cell. The second element in the mouse model is an endogenous clutch formed by the acrosome-acroplaxome-manchette complex. The links between the nuclear membrane and the manchette microtubules are crucial for the manchette movement and shaping of the sperm. As spermatids elongate, the links at the apex disengage and those at the distal ends engage in a ratchet-like manner. The perinuclear ring and the entire manchette structure move toward the tail region of the cell in a zipper-like movement and constrict [14]. Thus as shown in fig 1.4, the manchette sculpts and tapers the head of the spermatid as it migrates caudally down the nucleus while reducing its diameter progressively as the spermatogenesis progresses. The acroplaxome is anchored to the nuclear envelope of the elongating spermatid and the acrosome is bound to the acroplaxome. Both the perinuclear ring and the marginal ring encircle two-thirds of the spermatid head at the caudal site, as can be seen in fig 1.3. The diameter of the marginal ring gradually reduces, mimicking the constrictive migration of the manchette perinuclear ring as they descend along the nucleus toward the spermatid tail and thus steers the elongation of the spermatid head and facilitates in the nuclear shaping. The acroplaxome is stress-resistant and restrains the exogenous and endogenous forces acting on the spermatid head from excessively deforming the nucleus [5].

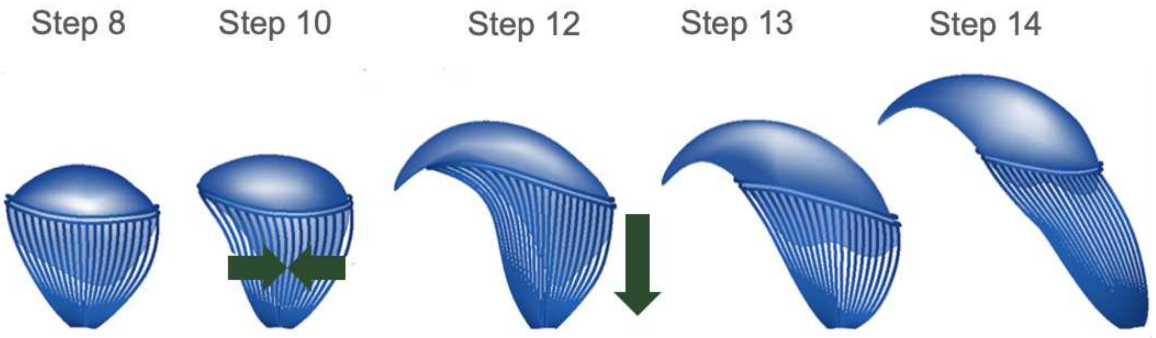

Figure 1.4: Schematic representation of the manchette during spermiogenesis. The manchette develops at the 8th step of spermatid and it constricts and sculpts the base of the nucleus while also progressing towards the caudal portion of the cell. Adapted from [5]

1.3 Super-resolution imaging

Fluorescence microscopy is a tool that is extensively used in molecular and cellular biological research. It allows to image biological samples, their components and cellular processes non-invasively. Techniques like immunofluorescence, in situ hybridization can be performed by the use of a wide range of fluorescent probes that are available in different colors [16, 17]. However, conventional fluorescent microscopy has a limited lateral resolution of approximately 200 nm and an axial resolution of around 500 nm, which is larger than many intracellular structures. Hence images of such structures obtained by a conventional fluorescent microscope are blurred or not resolved. To overcome this issue, a series of methods were developed called 'super-resolution' fluorescence microscopy. This section discusses the limit in fluorescent microscopy called the diffraction limit, a super-resolution technique called Stochastic Optical Reconstruction Microscopy (STORM) and the use of astigmatism in extending STORM from 2D to 3D.

1.3.1 Diffraction limit

In 1873, Ernst Abbe recognized that when the objective of the microscope converges light, the rays do not converge into a sharp focus but has a finite width. The size of that width is proportional to the wavelength of light and inversely proportional to the numerical aperture of the objective. The resolution of the microscope is depended on this spot as its intensity profile is of the same width of the spot. Hence the minimum width between two fluorophores such that they do not produce overlapping images and be considered a single image, is the width of the point spread function(PSF) [18]. This limit of resolution of far-field microscopic imaging is called Abbe's limit, which is given by d= λ/(2NA) where d is the minimum distance between the objects at that they can be resolved, λ is the wavelength of light and NA the numerical aperture of the objective [19]. In the experiments conducted for this thesis, λ is 641 nm, NA is 1.49, thus the lateral resolution limit according to the formula is 215 nm.

To overcome this diffraction limit some experiments used near field scanning microscopy and achieved a resolution of 100 nm but the application to conduct imaging needs a scanning probe close to the sample [20]. Far field methods that exploit the physical properties of fluorescent probes to determine positions of neighboring molecules in a diffraction limited region were developed in the recent years and were found to improve resolution to 20 nm [17, 18, 21]. These distinguished emissions of neighboring fluorescent molecules using spatially patterned illumination like stimulated emission depletion microscopy (STED) and saturated structured illumination microscopy (SSIM) or performed single molecular imaging by stochastic activation of photoswitchable molecules like stochastic optical reconstruction microscopy (STORM), photoactivated localization microscopy (PALM) and fluorescence photoactivation localization microscopy (FPALM). Both the methods exploit the fluorescent molecules chemically or physically to maintain nearby molecules in on or off states so that they can be individually resolved [18].

1.3.2 Stochastic Optical Reconstruction Microscopy

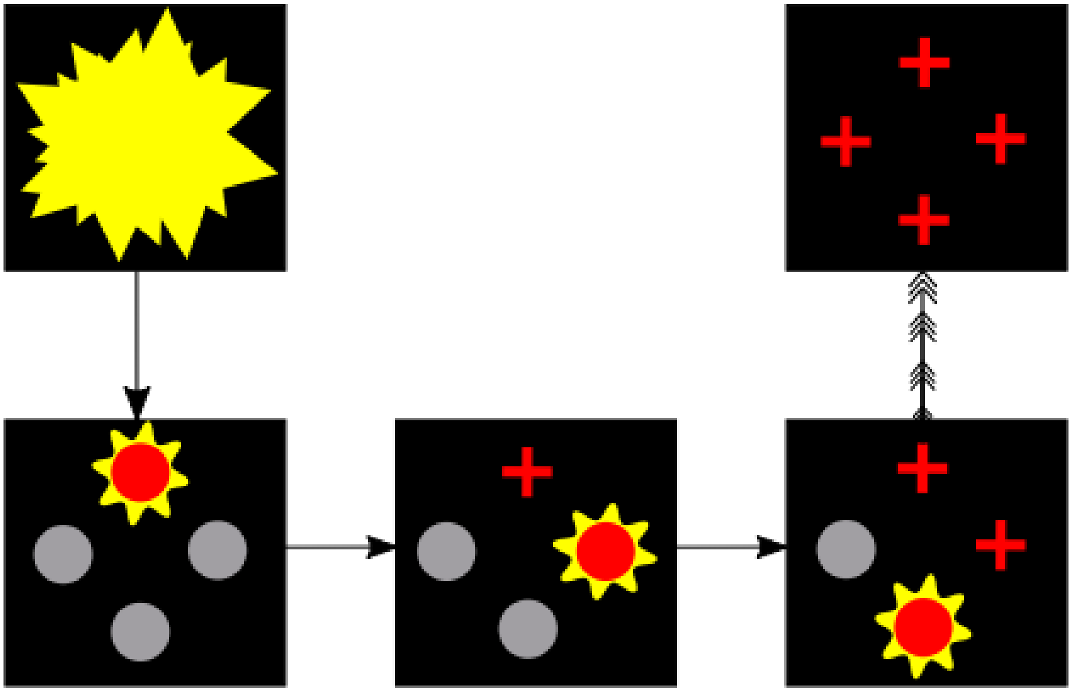

Figure 1.5: Principle of STORM. This image is taken from the PhD dissertation of Xinran Xu who is a previous student in Krapf lab [22]. Only one fluorescent molecule is activated at a given time in the diffration-limited region. The accumulation of these individual localization of molecules form the STORM reconstructed image

In STORM technique fluorescent molecules are stochastically activated individually from dark state (ON) to emission state (OFF) and the process is repeated several times. Individual molecules within a diffracted limited space can be precisely localized by this exploition of their photoswitchable nature. The image of a fluorescent molecule reflects the point spread function(PSF) of the microscope and appears as a diffraction-broadened peak. The center of this peak gives the position of the fluorophore. In biological samples, a single molecule can be localized by a precision of up to 1 nm [16, 23, 24]. This nano scale precision does not translate into image resolution. As long as the fluorophores are separated by a distance greater than the PSF width, they can be resolved but if they are positioned closer, their images overlap and the overall image will be a blur.

Hence, in STORM the emission from a region is controlled such that in a diffraction limited region, at a point of time, only one fluorophore is activated [25]. This fluorophore goes into dark state and another one in the same region gets activated and localized. This principle is illustrated in fig 1.3. The activation light applied to the sample has to be sufficiently low to achieve a low density of activated molecules such that only a sparse set of fluorophores are activated to emission state, allowing each of them to be individually localized. This repeated cycle of activation-imaging-deactivation leads to a super-resolved image reconstructed from several thousands of single fluorescent molecule localizations [16–18, 21, 26]. Consequently, the image resolution is limited not by diffraction but by the number of fluorescent molecules localized [25, 26].

STORM process requires the use of photo-switchable fluorophores for the proper labeling of the target molecules, stochastic activation of the fluorophores we labeled with and collection of large number of the fluorophores by the camera with nanoscale precision of localization of individual fluorophores [27, 28].

1. Immunofluorescence: The labeling of target proteins with organic proteins or dyes is done by immunofluorescence. The labelling density should be large so as to image sub-diffraction limited intracellular structures and functions.The molecules that we label with should satisfy a few conditions to generate a good STORM image. They should give out emission at a particular range of wavelengths and should otherwise be in a non-emitting dark state, which

by extension means that the contrast ratio between fluorescent and dark state should be high. This parameter allows high label density in samples without much background fluorescence [17]. In addition they should emit large number of photons. Furthermore, they should have a low spontaneous emission rate to limit to avoid thermally induced activation [18]. Another important parameter is that the rate of transition from the ON state to the OFF state (k_{off}) is larger than the rate of transition into the ON state (k_{on}). Alexa Fluor 647 matches all these criteria. They are very bright, detect about 6000 photons per activation cycle, have a contrast ratio of 1000, and high duty cycles to ensure repeated localizations [17, 29]. In the experiments discussed in this thesis we have used Alexa 647 dye.

The term photoswitchable or photoactivable is used only for the fluorescent molecules that can be converted to two or more distinct states when illuminated by an external light source [16]. Standard fluorophores like Alexa Fluor and ATTO belong to the rhodamine and oxazine classes and have energetically stabilized triplet states, hence are photoswitchable [30]. In the presence of potent donors like thiols and aromatic amines these dyes are photoreduced from the triplet state forming stable radical anions [27, 31, 32]. (k_{off}) is controlled by the concentration of thiols. Because of these reasons we add 2-mercaptoethanol which is a thiol compound, to the imaging buffer that we add to the sample right before imaging. In the presence of molecular oxygen, the rhodamine dyes survive for hundred of milliseconds and they get trapped in radical ion state for several hours on the removal of oxygen. (k_{on}) depends on the concentration of oxygen [27]. Oxygen scavengers improve the reversibility of photoswitching and reduces photobleaching [21, 33, 34]. Therefore we add an oxygen scavenger- GLOX to the imaging buffer.

2. Image Acquisition: STORM imaging set-up consists of an illumination source, a light collector and an image detector. The source of illumination in our experiment is a laser. To ensure that most fluorescent molecules are in OFF state than in ON state at a given time, the laser should be of high power. For the experiments discussed in this thesis, we used a laser of an output power of 150 mW. High powered laser increases background fluorescence

and that should be mitigated, for example, while imaging phalloidin-stained actin, sodium borohydride is added in the immunostaining process to reduce autofluorescence. A total internal reflected microscope (TIRF) with an oil immersion objective of high aperture is used as the light collector. Since TIRF mode limits the fluorophore excitation to a thin field of 100-200 nm and since in our experiment the target molecules lie above 200 nm from the objective, the microscope is aligned close to TIRF but not at TIRF. An electron-multiplying charge controlled device (EMCCD) camera with high quantum efficiency and low noise is used for image detection. The pixel size is set as 2.3 times smaller than Abbe's limit in order to preserve the information of fluorophore position. Pixel size is in the range of 80 nm to 160 nm for visible light [21]. In our experiments, the optical system we use has a pixel size of 130 nm (camera has a pixel size of 13 nm and the 100x objective magnifies it by 100 times).

3. STORM Reconstruction: The collected data is processed by a series of steps. Firstly, a smoothing filter is applied to each image to locate the pixels with intensity values, which are the pixels with the highest number of photons detected in that PSF sized region. These locations translate to probable fluorophore positions [35]. Secondly, a 2D gaussian window is fitted with the PSF model to localize fluorophores. The amplitude translates to the number of photons, center in X and Y gives an estimate of position of fluorophore or localization [21, 36]. Mathematical computation models like least square fitting or maximum likelihood estimation is performed to fit the gaussian to PSF model. During these steps, a photon threshold is applied to ensure that multiple fluorophores in a diffraction limited space are not localized at a time, thus avoiding overlapping PSFs. As STORM uses reversible photoswitchable fluorophores, it is very likely that the same fluorophore has been individually localized multiple times. So discarding duplicates does not adversely affect the structural information. Post processing steps include duplicate removal, filtering, drift correction and merging. Drift correction is a crucial step. Axial drift is corrected online with ASI MS 2000 device during image acquisition (refer 2.3.6 for details and Appendix G- Finding and imaging spermatid for procedure) while lateral shift can be corrected using cross-correlation

methods in the post-processing step. Merging is done at the end of post-processing to combine all the single molecular localizations to a super-resolved image.

1.3.3 Astigmatism method

The experiments conducted in this thesis aim to 3D localize cytoskeleton in spermatids. To expand the STORM technique to 3D capability, the lateral as well as axial positions of the fluorophores are required [17]. Methods using double helical PSFs, interferometers and defocusing by dual or multi-focal plane or astigmatism, are the most popular for this purpose [37, 38]. Defocusing methods are easier to implement than the others. In astigmatism method, a cylindrical lens is introduced to the optical pathway in x and y directions forming two different focal planes that reshape PSF with different ellipticity [22]. This is because light propagating in perpendicular planes have different focal points. A single molecule appears elliptical and hence by its ellipticity we can determine axial position and from its center the lateral position can be found [16]. By fitting the image with a 2D elliptical Gaussian function, z coordinate of the fluorophore can be determined. Although the method is easier to implement and has about 50 - 60 nm axial resolution, astigmatism approach does not correct optical aberrations within the system and also induces aberrations with the addition of the cylindrical lens causing deformations in PSF. To overcome these issues, MicAO 3DSR adaptive optics device was introduced to our optical system. It contains a deformable mirror that corrects the aberrations introduced in the system by the optical elements and biological sample [39]. The mirror adds the perfect amount of astigmatism to the system, allowing precise 3D localization of fluorophores.

Chapter 2

3D Localization of α tubulin in spermatids

2.1 Introduction

The eukaryotic cytoskeleton comprises of three filament systems- microtubules, actin filaments and intermediate filaments. Microtubules are larger than actin filaments and are hollow tubes of about 25 nm in diameter. They are made of alpha and beta tubulin heterodimers which polymerize into linear protofilaments [7, 40]. The head-to-tail arrangement of α or β heterodimers results in structural polarization, with α tubulin located at the minus end and β tubulin at the plus end. The plus end is characterized by state of rapid growth and the minus end has slow growth because it is the end that anchors the microtubule. Microtubules undergo polymerization and depolymerization, thus rapidly alternating between shrinkage and growth. This dynamic instability is a unique feature of microtubules. [41]. In certain cells, microtubules radiate from the centrosome and form an organized network but haploid male germ cells have non-centrosomal microtubule arrays that perform various cell functions such as cytoplasmic transport of proteins and vesicles, chromosome alignment during meiosis and mitosis, and beating of flagella. The trafficking of proteins to specific cellular regions plays a crucial role in the proper sperm development. Two such cellular regions are the region between the endoplasmic reticulum, the Golgi apparatus and the acrosome-acroplaxome complex, and the manchette. As discussed in section 1.1 , during acrosome biogenesis, the pro-acrosomal vesicles are trafficked via microtubule and actin tracks. As discussed in section 1.2.2, the manchette is formed at step 8 during spermatid elongation and is made of microtubules and actin filaments. it plays a vital role in nuclear modelling and cytoplasmic transport as well as transport between the nucleus and cytoplasm via IMT.

The experiment discussed in this chapter uses 3D STORM technique to visualize α tubulin in the cytoskeleton of spermatids. Based on experiments conducted by our collaborator Dr Maria E. Teves and her research team at Virginia Commonwealth University, we know that α tubulin is localized in the manchette. Since the manchette assembles at step 8 and completely disassemble after step 14, we focus on steps 10-14. We find that manchette is rich in α tubulin and the structure radiates from the base of the nuclear region and moves caudally as spermatid elongation progresses. Also, the experiments confirmed that machette is assembled to form its rigid cytoskeletal network in step 10 and disassembles into constituent structures after step 14.

2.2 Materials and methods

2.2.1 Sample collection

Detailed protocol for sample collection is in Appendix C - Collecting and fixing spermatid cells from mice.

Mice that are at least 5 weeks old were purchased from Charles River Laboratories (Wilmington,MA). Animals were euthanized according to the guidelines of Institutional Animal Care and Use Committee (IACUC) of Colorado State University. Two testes were collected and stored at 4°C in Dulbecco's Modified Eagle Medium (DMEM) which has vitamins, amino acids and glucose to maintain cells in its environment. The testes were dissected and its contents were collected in an isolation buffer made of DMEM, and the digestion enzymes- collagenase and DNAse. DNAse reduces clumping of cells. The sample is incubated at 32°C and is mechanically digested to break the tissue. This process is done with care so that the cells do not break. The flagella and acrosome are not fully formed structures in many spermatid stages and they may be broken or displaced from the cells. The sample then undergoes multiple centrifugation processes to separate the spermatid cells from other cells and debris in the sample, and gets suspended in Phosphate-Buffered Saline (PBS) before sample fixation.

2.2.2 Fixing samples

Detailed protocol for sample fixation is in Appendix C - Collecting and fixing spermatid cells from mice. Freshly prepared fixative solution made of Sucrose and Paraformaldehyde in PBS is added to the cells. Paraformaldehyde is a fixative and is added to preserve the cellular structure without changes in protein structure [42]. It is an important step before permeabilizing and immunostaining the cells as cells that are not fixed will lyse and diffuse away before antibody incubation step. The sample is then centrifuged and suspended in PBS. The sample density is checked by adding 8 μl of sample to a coverslip and mounting the sample on a microscope. If the cells are too crowded, dilute the remaining sample by adding 1 to 2 μl of PBS. Check the sample again and correct the density so that the sample has enough density but the cells are not clumped. Once it reaches the desired density, transfer the cells to Poly-L-lysine coated coverslips.

2.2.3 Immunostaining samples by indirect immunofluorescence

The protocol for immunostaining is explained in detail in Appendix D- Labelling the cells.

Imunofluorescence can be achieved by two methods- direct and indirect. In direct immunofluorescence, fluorescent label is conjugated directly to an antibody, and this identifies and binds to the target molecule. This method is faster and has less issues related to non-specific binding that causes background signal but, each target requires specific antibodies and hence it is experiment specific, reducing the flexibility of the experiment design. Also, fluorescence-coupled primary antibodies are expensive [43]. Indirect immunofluorescence uses two antibodies- a primary that is unconjugated and recognize and attach to the target, and a secondary antibody that is tagged with fluorescent dye and recognizes and binds to the primary antibody [44, 45]. This method is slightly more complex than the direct method but more flexible for the experiments as the secondary antibody conjugates can be easily available in the market. Each protocol needs to be tweaked according to the cell type and antibody.

Immunostaining process requires the cell membrane to be more porous than usual so that larger molecules like antibodies and fluorescent dyes can pass into the cytoplasm and reach the targeted intracellular structures [46]. This can be achieved by removing lipids from the cell membrane by use of organic solvents or detergents. In our method, we use Triton X-100 which is a detergent. After a couple of PBS washes, a blocking buffer made of goat serum, Bovine Serum Albumin and Triton is added to the sample [47]. Goat serum contains antibodies that bind to the non-specific sites of the target molecule. Blocking is an important step in reducing the background interference and improving signal-to-noise ratio. After incubating the sample with blocking buffer, primary antibody is added [48]. The samples are incubated for 12 hours. The samples are washed with PBS three times to remove any cells that are not bound to the coverslip and also wash any primary antibody that is unbounded. The secondary antibody solution is added to the coverslip and incubated for an hour and then washed with PBS. Before imaging, an imaging buffer made of 2-mercaptoethanol and GLOX is added. 2-mercaptoethanol is a thiol compound that induces stochastic blinking of fluorophores, which is the fundamental idea of STORM. GLOX removes oxygen from the sample, thus preventing photobleaching.

2.3 Instrumentation and software

2.3.1 Aligning TIRF microscope

For imaging we use a Total Internal Reflection Fluorescence (TIRF) microscope. The target molecules are located more than 200 nm from the coverglass surface and hence instead of TIRF, the imaging set-up is only set to close to TIRF [28]. For that the system is aligned to TIRF and adjusted. The laser and microscope alignment protocol is detailed in Appendix E- Protocol for aligning a TIRF microscope. The alignment has to be done before every imaging to ensure good quality images.

2.3.2 3D STORM imaging set-up

STORM imaging set-up consists of a LASER for illumination, objective lens for light collection and camera for image detection.

1. Laser:

   STORM requires a high power laser so that most of the fluorophores are in the OFF state and only few are ON. In Krapf lab we use a 641 nm laser (CW Diode laser DL640-150-O, CrystaLaser, Reno, NV). A violet laser- 405 nm was used to photo-switch the photo-bleached fluorophores.

2. Objective lens:

   STORM technique employs precise localization of individual fluorophores from detecting photons at every activation, hence identifying their position coordinates. The precision of this localization is proportional to the resolution of the objective and hence is inversely proportional to the numerical aperture of its objective [28]. Also, higher the numerical aperture (NA), higher the number of photons detected. The objective lens used in the image set-up is an Olympus PlanApo 100xNA 1.49 objective. It is an oil immersion objective. Oil immersion objectives reduces light loss from refraction by replacing air gap between the glass slide and objective lens with oil [49–51]. The oil becomes part of the objective system and improves the resolution and hence the NA is same as if the objective diameter was increased.

3. Camera:

   Super-resolution techniques require cameras with high quantum efficiency and low noise, and have deep cooling mechanism. We used Andor iXon DU-888, water cooled , back illuminated EMCCD camera. The cooling helps to reduce the dark current in the device and hence the system is maintained at -70 °C. Since the camera is back illuminated high number of photons are preserved, thus increasing quantum efficiency. As all the pixels in the camera share a gain register as well as an analog to digital converter and has on-chip multiplication technology, an EMCCD camera has low fixed pattern noise and low read noise. The camera captures images at the rate of 50 frames/second.

2.3.3 Calibrating the MicAO

STORM technique uses the principle of stochastically activating individual fluorophores that are photo-activable and spatially resolves localization of these individual fluorophores with high precision [52]. The process is repeated over and over to capture most fluorophores. As experiments, such as discussed in Yildiz et al., have shown that single fluorophores can be detected with a signal to noise ratio about 100, thus limiting the localization precision at 1nm in lateral dimensions [23,28,53]. The centroid of an image of a fluorophore gives the information about its lateral position and shape of that image gives its axial position. Since the PSF is symmetrical along the z axis, regular STORM techniques has poor axial resolution. To combat this issue many experiments have employed the astigmatism method where a weak cylindrical lens is introduced in the image pathway, thus creating a focal plane in x and one in y direction. Because of these slightly different focus planes, the point spread function (PSF) appears to be round when fluorophore is in focus (point of equal distance from x and y planes or average focal plane), ellipsoidal in y with its long axis in x when it is above the average focal plane and ellipsoidal in x when it is below the average focal plane [24]. To obtain the centroid with precision in x and y planes, the image is approximated by a 2D Gaussian function. From this, the peak widths and the coordinates of the peak and hence the z position can be obtained. Although this method has more accuracy than regular STORM technique, adding a weak cylindrical lens introduces optical aberrations to the system, reducing the number of photons collected and the shape of PSF [39, 54]. In addition to this, the components of microscope and the biological sample themselves cause optical aberrations. The adaptive optic device- MicAO 3D-SR developed by Imagine Optic consists of wavefront sensor and deformable mirror that precisely detects and corrects these aberrations [39]. The device has the 52 actuator deformable mirror with the capability of inducing small amounts of 2D astigmatism in PSF [54]. During the first installation, an initial optimization was conducted for the microscope. The aberrations were measured by wavefront sensors and corrected using the deformable mirror and by using 3N algorithm. The mirror shape was stored in the computer as closed loop Casao.has in the lab computer. As explained in the Appendix F- 3D STORM Calibration Protocol, this mirror shape serves as the reference for obtaining PSF. Since it was found that an astigmatism of 60 nm gave the best PSF for the system, we set the astigmatism settings accordingly, as shown in figure F.2 in Appendix F. This method allows 3D reconstruction of images of individual fluorophores by accurate detection of single molecules over 1 μm axial range or thickness.

2.3.4 Image acquisition

The protocol for image acquisition of spermatids is detailed in Appendix G- Finding and imaging spermatid. The PSF used is the final PSF saved after calibrating the MicAO.

2.3.5 Obtaining look-up table

The sequence of super-resolution images obtained consists of 50 thousand frames. To process such large data with sub-diffraction precision, we use ThunderSTORM which is an open-source, interactive plug in for ImageJ that has a wide collection of processing and post-processing methods [55]. The calibration tool of the software is used to obtain calibration curves from the z stack of images obtained from 0.1 μm Tetraspeck microspheres, according to Appendix F- 3D STORM Calibration Protocol. These images range from a z height of 1 μm to -1 μm with 10 nm thickness. As mentioned in section 1.3.3, the obtained PSF is fitted by 2D Gaussian by which the peak widths and the coordinates of the peak are obtained. The spread of the Gaussian curve in x and y helps in determining the z position of the fluorophore. In ThunderSTORM, the image is filtered by wavelet filter and fluorophores are localized by determining the local maxima. The software uniquely allows setting a specific threshold for detecting molecules and previewing the resulting movie with the molecules detected according to the settings. The threshold is fixed based on the best estimation of molecules in the movies.

As the calibration curves that "are symmetric along z=0 and with noise levels of the the same order above and below the focus" gives the most precise axial localization, we use the configuration file from the calibration movie that produced the best sigma curve, for the 3D STORM reconstruction of the spermatid images [39]. Refer Appendix H for the protocol to obtain the configuration file.

2.3.6 3D STORM Reconstruction of images

The calibration file is obtained from the calibration tool of ThunderSTORM, according to Appendix H. The software allows selecting multiple parameters to detect single fluorophores with accuracy. To remove noise and improve the localization of individual fluorophores, wavelet filter (B-spline) is used. This is particularly useful when the background is not estimated. The next step is approximate localization of molecules which is done by recognizing the local maxima of the pixel as its center. This stage rejects all molecules that occur in distance less than PSF diameter, to avoid overlapping molecules and thus save computation time [28]. The sub-pixel localization of molecules is done by approximating the PSF model by an elliptical gaussian function. The raw

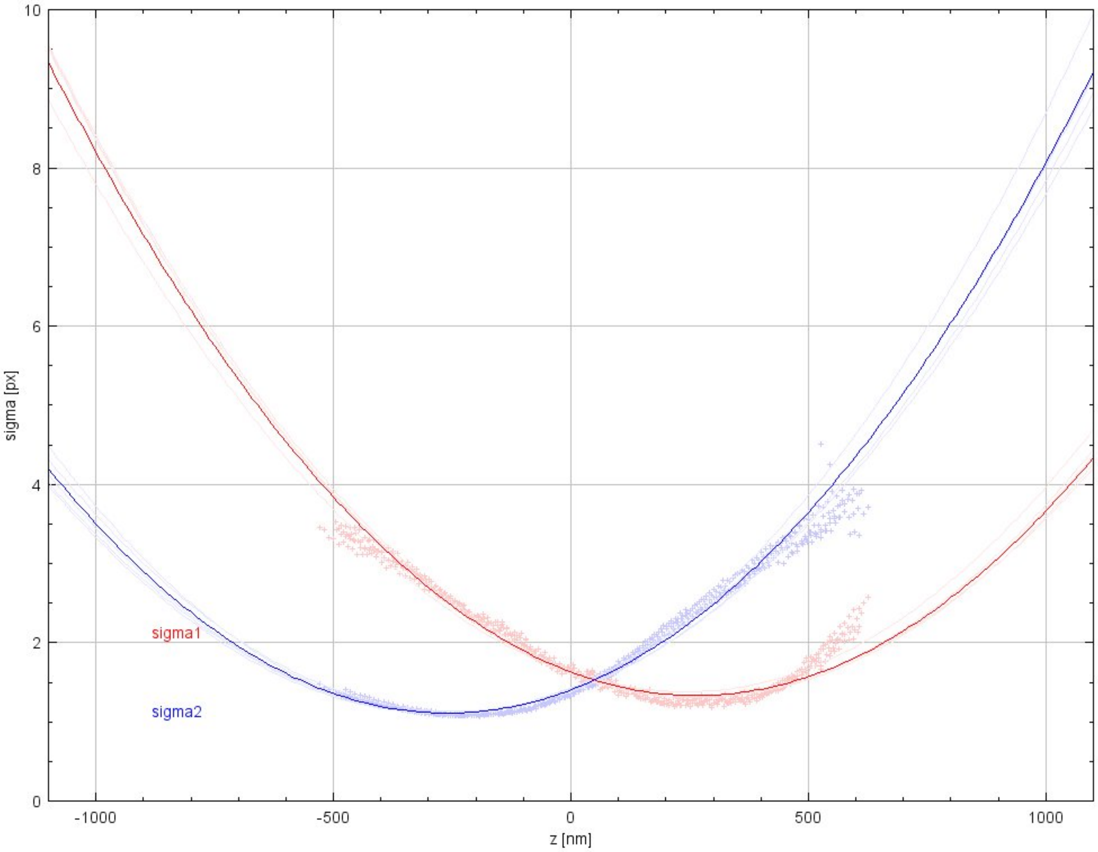

Figure 2.1: Calibration curve generated for a group of 0.1 μm Tetraspeck microspheres. The z stack is 2 μm with a step size of 10 nm

data is fitted to the PSF model by least square method. This method is robust to the distortions in PSF caused by optical aberrations, and is preferred over other mathematical optimization methods in cases where the exact information about the camera, PSF and noise model is not known. The visualization of data is set as normalized gaussian. Once the processing is done, post-processing routines are performed. ThunderSTORM allows removing duplicates obtained in the analysis. After that step, we filter out molecules outside 500 nm z height on either side of the focus because our calibration system has a localization precision over a z range of 1 μm [55]. The next step is drift correction. This is essential to avoid blurs in reconstructed images as a drift of even 10 nm distorts images [56]. This is corrected in some experiments by use of fiduciary markers, but since we do not wish to add new markers as it may interfere the imaging structures, and also the imaging parameters need to be changed to adapt to these markers, we correct lateral drift by cross-correlation methods [28]. The axial shift is corrected in our experiments by ASI- MS2000 which compensates drifts due to factors like thermal expansion and mechanical vibrations, by relying on the refractive index mismatch at the interface between coverglass and imaging medium. This autofocus system detects the smallest drift between the objective lens and coverslip of the sample, provides feed back to the focus controllers of the device and eliminates focus drift, thus enabling the sample to remain accurately in focus while being imaged for several hours. The focus accuracy is 5% of the objective depth of focus [57, 58]. Applying density filter removes isolated or poorly localized molecules. Merging of molecules is done next. We can specify the number of frames that the molecule should be repeatedly present to be considered a single molecule and the distance along x and y within which molecules should be merged. Appendix I contains the detailed step by step instruction for 3D STORM reconstruction.

2.4 Results

The 3D STORM images obtained showed that α tubulin is localized in the manchette of the elongating spermatids. Fig 2.2 (a) shows the bright field image of a step 10 spermatid. The entire cell could not be captured for 3D STORM reconstruction as the imaging system is limited at region

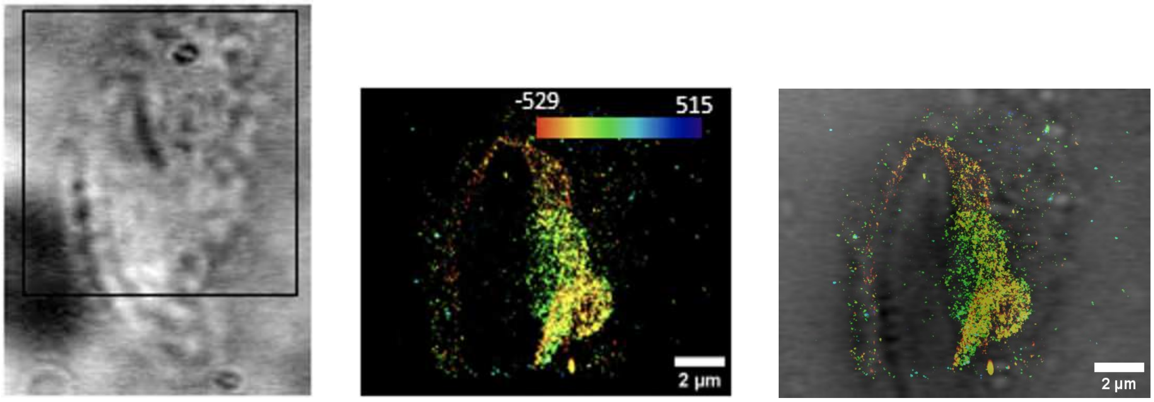

(a) (b) (c)

Figure 2.2: α tubulin structure in a mouse spermatid at step 10 (a) Bright field image of a step 10 spermatid with background subtracted. The height of the cell is longer than 100 pixels but the imaging set up limits the ROI height to 100 pixels to reduce the time taken to capture 50000 frames. The region of the cell captured by STORM imaging is marked with the black rectangle. (b) 3D STORM reconstructed image of α tubulin in cell shown in image a with the z-position information color coded. The reconstruction is colored according to the localization height as indicated in the color map. (c) Overlay of the bright field image a with the reconstructed image b. Scale bar is 2 μm

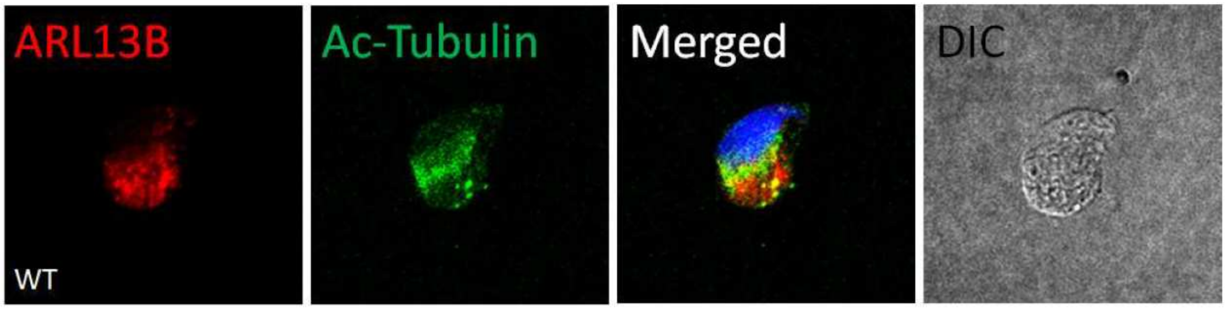

Figure 2.3: Confocal images of step 10 spermatid. This image was obtained by Virali Bhagat [59] of Dr Marie E Teves' research team at Virginia Commonwealth University. ARL13B (red) is localized in the acrosome and the manchette, acetylated tubulin is found in the manchette, DAPI is found in the nucleus (blue). The differential interference contrast (DIC) image shows the step 10 spermatid which was stained with ARL13B, acetylated tubulin and DAPI

of interest(ROI) height of 100 pixels. The ROI captured is marked with a rectangular black box. It can be seen from the overlay image fig 2.2(c) that the manchette microtubules start at the base of the nucleus and is extended towards the base of the cell in an almost diagonal fashion as seen in the acetylated tubulin confocal image in fig 2.3 obtained by Virali Bhagat at Virginia Commonwealth University. Moreover, the overlay of STORM reconstruction on the bright field image, fig 2.2(c) shows the cytoplasm and the axoneme is almost completely devoid of α tubulin.

The color coding shows the height of the localization of fluorophore in the spermatid cell, with red marking the z height at one end and blue at the other end of the cell. Unlike in the 2D confocal image, 3D STORM image shows that the localizations of α tubulin are points of 80 to 100 nm diameter and are connected in a mesh-like manner and from the color coding, it can be seen the manchette is present as mesh-like structures at the different depth of the cell and is present over half the length of the cell.

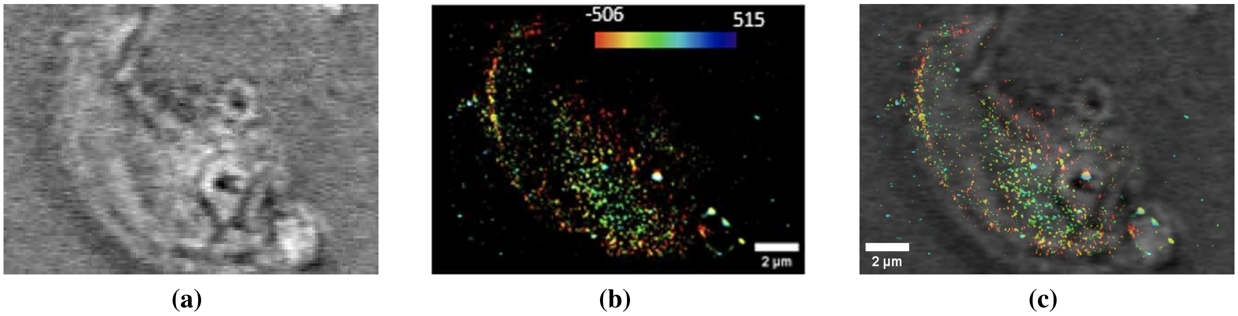

(a) **(b)** **(c)**

Figure 2.4: α tubulin structure in a mouse spermatid at step 11 (a) Bright field image of a spermatid of step 11 with background subtracted (b) 3D STORM reconstructed image of α tubulin in cell shown in image a with the z-position information color coded. The reconstruction is colored according to the localization height as indicated in the color map. (c) Overlay of the bright field image a with the reconstructed image b. Scale bar is 2 μm

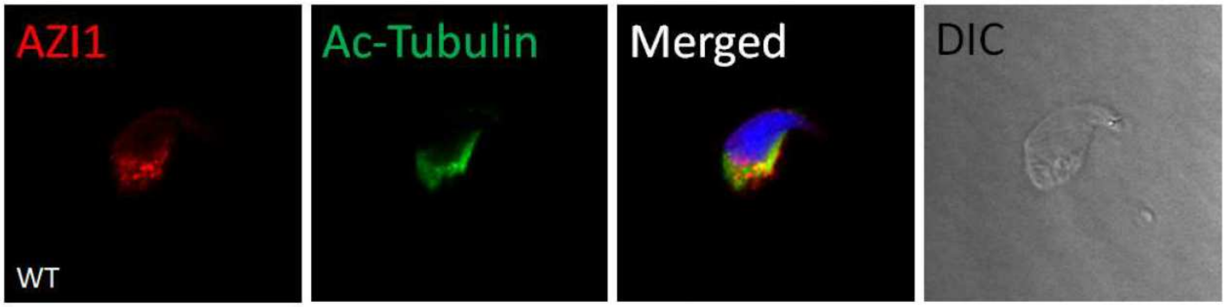

Figure 2.5: Confocal images of step 11 spermatid. This image was obtained by Virali Bhagat [59] of Dr Marie E Teves' research team at Virginia Commonwealth University. AZI1 (red) is localized in the acrosome, the manchette and centrosome, acetylated tubulin is found in the manchette, DAPI is found in the nucleus (blue). The differential interference contrast (DIC) image shows the step 11 spermatid which was stained with AZI1, acetylated tubulin and DAPI

Fig 2.4 (a) shows a step 11 spermatid. Fig 2.4(b) shows points of localizations of about 80 to 90 nm diameter with hints of meshes of α tubulin but there are not enough localization points. The larger points of specific localizations are about 310 to 460 nm in diameter. Again, the manchette are observed at different z positions. It can be observed that from fig 2.4 (c) that as seen in the acetylated tubulin image in fig 2.5, the manchette has moved further caudally down the cell.

The 3D reconstruction of step 12 spematid in fig 2.6 (b) shows an elaborate mesh network in the region that α tubulin is distributed. Fig 2.6 (d) is an enlarged image of the marked rectangular portion of the 3D reconstruction illustrating how extensive the mesh structure is. From our understanding of the observations in the 2D confocal images in fig 2.7, other research experiments [8,14], and literature survey [4, 13, 60], we know that the structure where the α tubulin localizations are interconnected is the manchette. Fig 2.6 (b) also shows the cell boundary clearly and it can be observed that manchette is present throughout the depth of the spermatid. The STORM image overlayed on the bright field, fig 2.6 (c) shows a further descent of the manchette. It can also be observed that cytoplasm is getting eliminated as spermatid differentiation progresses. In step 14 spermatid seen in fig 2.8 (b), α tubulin localizations in the spermatid are interconnected at various depths of the cell. Mesh-like structures can be observed, especially towards the caudal region of the cell, as can be seen in the zoomed image in fig 2.8 (d). In fig 2.8 (c), it can be observed that the manchette has extended from the acrosome to the base of the cell. The head of the spermatid has now be shaped and has begun to achieve the hook shape as is expected in a mouse spermatid. It can be observed from fig 2.8(c) that most of the cytoplasm has been drained from the spermatid. The flagella can be seen to the right of fig 2.8(c). From 2.10 (b), it can be seen that α tubulin is only present as points of localizations and not as defined structures. The manchette has disassembled to its constituents in step 15. This observation conforms our knowledge that the manchette disappears after step 14.

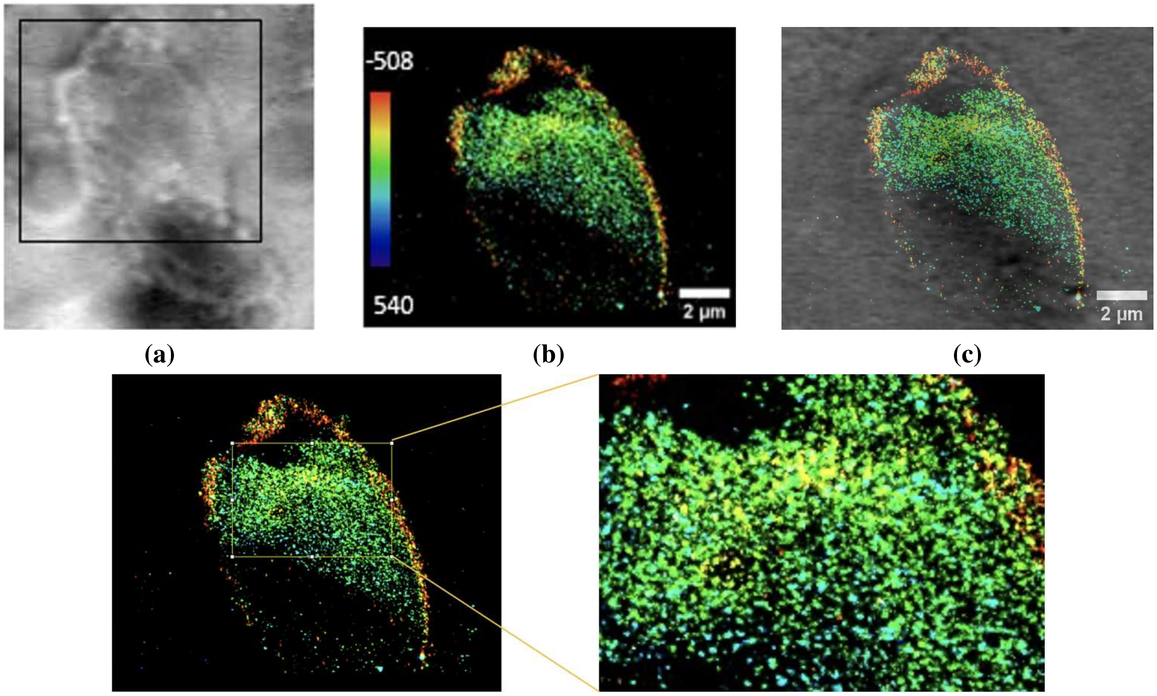

(a) (b) (c)

(d)

Figure 2.6: α tubulin structure in the captured section of a mouse spermatid at step 12 (a) Bright field image of a step 11 spermatid with background subtracted. The height of the cell is longer than 100 pixels but the imaging set up limits the ROI height to 100 pixels to reduce the time taken to capture 50000 frames. The region of the cell captured by STORM imaging is marked with the black rectangle. (b) 3D STORM reconstructed image of α tubulin in cell shown in image a with the z-position information color coded. The reconstruction is colored according to the localization height as indicated in the color map. (c) Overlay of the bright field image a with the reconstructed image b. (d) Enlarged picture of the area surrounded by the yellow rectangle in the 3D reconstruction. Scale bar is 2 μm

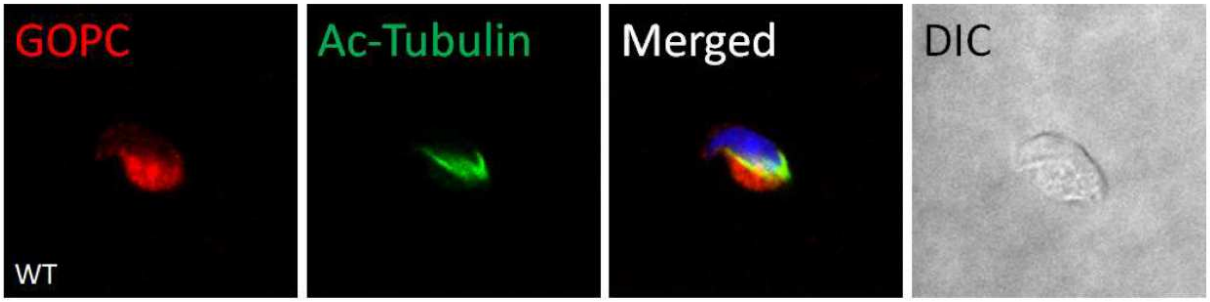

Figure 2.7: Confocal images of step 12 spermatid.This image was obtained by Virali Bhagat [59] of Dr Marie E Teves' research team at Virginia Commonwealth University. LRGUK (red) is localized in the acrosome vesicles and the manchette, acetylated tubulin is found in the manchette, DAPI is found in the nucleus (blue). The differential interference contrast (DIC) image shows the step 12 spermatid which was stained with LRGUK, acetylated tubulin and DAPI

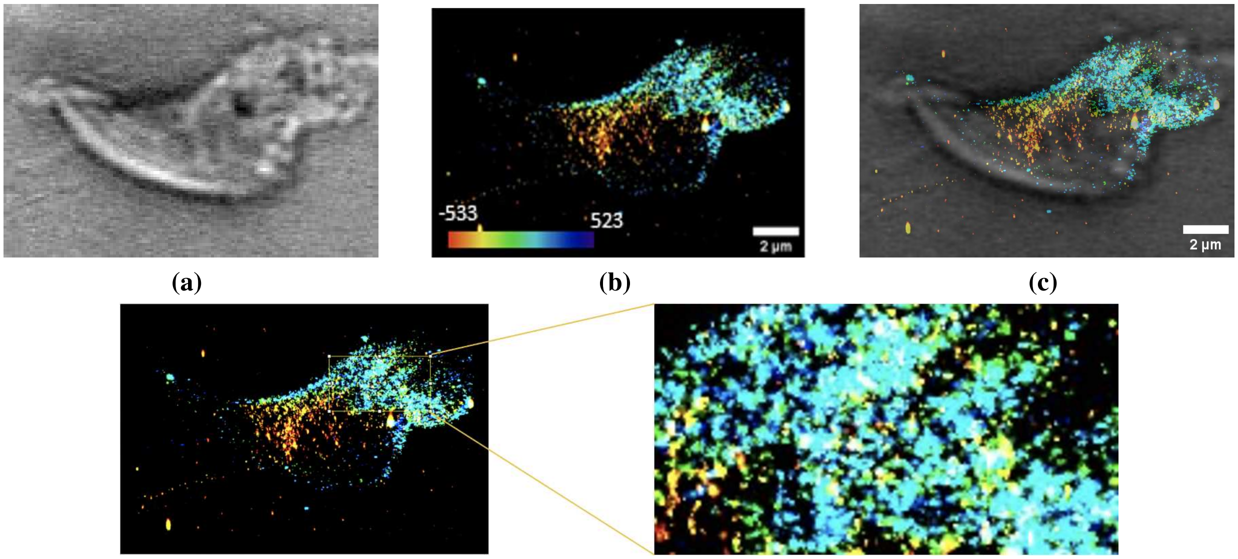

(a) (b) (c)

(d)

Figure 2.8: α tubulin structure in a mouse spermatid at step 14 (a) Bright field image of a step 14 spermatid with background subtracted. The flagella is visible on the right side of the image (b) 3D STORM reconstructed image of α tubulin in cell shown in image a with the z-position information color coded. The reconstruction is colored according to the localization height as indicated in the color map. (c) Overlay of the bright field image a with the reconstructed image b. d) Enlarged picture of the area surrounded by the yellow rectangle in the 3D reconstruction. Scale bar is 2 μm

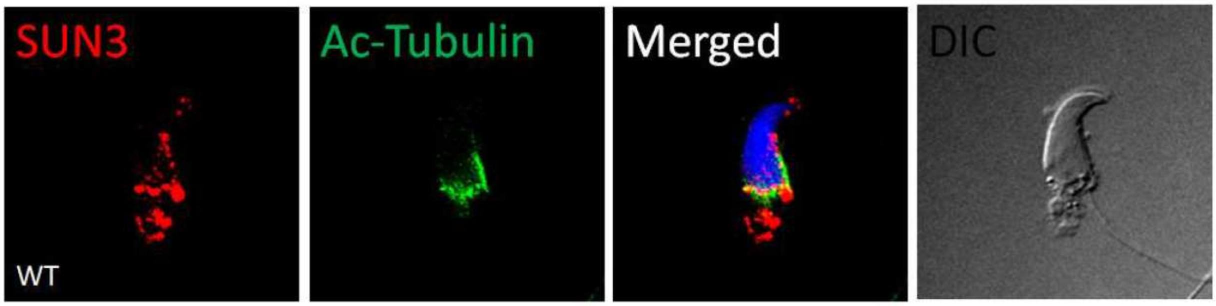

Figure 2.9: Confocal images of step 14 spermatid.This image was obtained by Virali Bhagat [59] of Dr Marie E Teves' research team at Virginia Commonwealth University. SUN3 (red) is localized in the manchette, acetylated tubulin is found in the manchette, DAPI is found in the nucleus (blue). The differential interference contrast (DIC) image shows the step 14 spermatid which was stained with SUN3, acetylated tubulin and DAPI

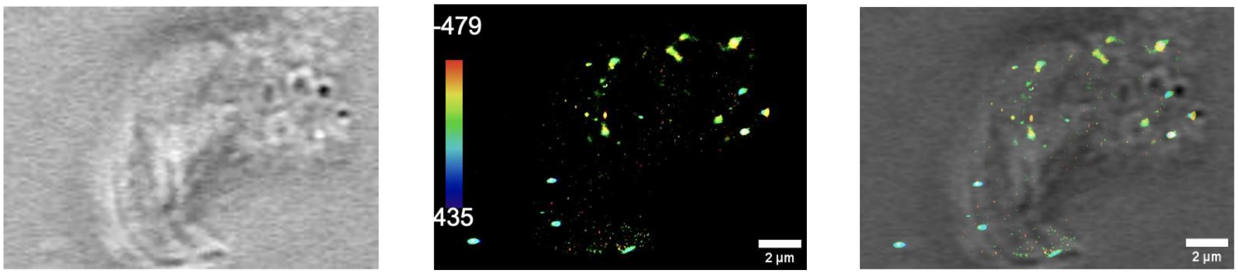

(a) **(b)** **(c)**

Figure 2.10: α tubulin structure in a mouse spermatid at step 15 (a) Bright field image of a step 15 spermatid with background subtracted. The flagella has been detached possibly during the mechanical agitation of the sample during preparation (b) 3D STORM reconstructed image of α tubulin in cell shown in image a with the z-position information color coded. The reconstruction is colored according to the localization height as indicated in the color map. (c) Overlay of the bright field image a with the reconstructed image b. Scale bar is 2 μm

Chapter 3

3D Localization of phalloidin stained actin in spermatids

3.1 Introduction

Actin was found to be encoded in ancestral genes from 3 billion years ago and is one of the most abundant proteins in the world. Actin filaments or F-actin, also known as microfilaments, provide mechanical support, move proteins, vesicles and intracellular materials and drive cell movements [61]. Animals have actin filaments, microtubules and intermediate filaments as their cytoskeletal polymers. Genes for actin are highly conserved in all eukaryotic cells and have many genes for the molecular motor myosin which on hydrolysing Adenosine Triphosphate (ATP) generate forces on microfilaments and assist in many functions such as cellular transport and cytokinesis [62, 63]. Actin and myosin were discovered in muscle cells in the 1940s and were found to be present in other cells in the 1960s. Globular actin or G-actin is the basic unit of actin filaments. When initiated by actin nucleators or nucleation complexes, G-actin monomers binds to ATP forming stable di- or trimers and by the addition of more monomers form a long stable double helical chain of F-actin [7, 60]. As actin monomers are oriented asymmetrically, actin filaments are polar with their two ends, called barbed end and pointed end, being biochemically and structurally different from each other [64]. The barbed end is the fast growing end due to ATP-dependent elongation and is called the plus end, and the pointed end shortened by dissociation and is called the minus end. This elongation at one end and shortening at the other is called actin filament treadmilling and generate forces for many cellular processes along with the forces generated by myosin [65]. Myosin molecules travel towards either of the two end of actin filaments and transport various cargo in the cell.

Actin filaments are concentrated in spermatogonic cells and Seroli cells. Sertoli cells have apical ectoplasmic specializations composed of actin filament bundles sandwiched between Sertoli cell plasma membrane and cistern of endoplasmic reticulum between Sertoli cell and the head of elongating spermatid [66, 67]. These F-actin containing hoops exert external forces that shapes the nucleus and hence the head of the elongating spermatid, as discussed in section 1.2.3. F-actin is also found in the acroplaxome of the cell, which as discussed in section 1.2.1, is an actin rich cytoskeletal plate connecting acrosome and spermatid nuclear membrane. It is also found in the manchette which is a temporary structure that assembles at step 8, during spermatid elongation, and disassemble at step 14. The manchette is located at the caudal region of the acrosome and as discussed in section 1.2.2 plays a major role in trafficking of cargo by facilitating IMT, thus critical for acrosome and axoneme formation, and also tapers and shapes the nuclear head.

To image actin many investigators have used phalloidin conjugated fluorescent molecules. Phalloidin belongs to a class of toxins found in death cap mushroom called phallotoxins. It binds and stabilizes F-actin and prevents the depolymerization of actin fibers [68]. Unlike antibodies, phalloidin does not bind to G-actin monomers and is permeable to aldehyde fixed cells [69]. This selective binding to F-actin makes phalloidin containing fluorescent tags an excellent tool in visualizing F-actin in microscopy methods.

In this chapter, we will discuss an experiment to image F- actin in the cytoskeleton of spermatids of step 10 to 14 by 3D STORM technique. As mentioned in chapter 2, we chose these steps to observe a fully developed manchette and acroplaxome. To image F-actin, phalloidin conjugated with Alexa Fluor 647 is used in immunostaining process. We confirmed in 3D that actin is localized in acroplaxome of spermatids and is also present in the manchette. In addition to this, as observed in the experiment in chapter 2, the manchette is found to descend to the caudal region of the spermatid head as the spermatid differentiation progresses. Moreover, manchette is found to be located at the base of the cell at step 14 and is found to have disassembled in the later steps.

3.2 Materials and methods

3.2.1 Sample collection

This section is explained section 1.2.1- Sample collection. Detailed protocol for sample collection and preparation is in Appendix C - Collecting and fixing spermatid cells from mice.

3.2.2 Immunostaining samples by indirect immunofluorescence

As explained in section 1.2.2- Fixing samples, fixing is a crucial step before immunostaining with molecules. The sample is fixed with a solution containing gluteraldehyde and Triton X-100. Triton is a detergent that removes lipids from the cell membrane to make it more porous for larger molecules. Freshly prepared sodium borohydride is added to reduce autofluorescence because of the aldehyde added to the sample [70]. The washes are done with cytoskeleton buffer to preserve the intracellular structure of the cells in the sample. This procedure uses direct immunofluorescence. Phalloidin is conjugated with Alexa 647 fluorescent dye [68]. It is used as it binds to filamentous actin (F-actin), thus in STORM imaging it helps in localizing actin filaments. The ideal time of incubation was found to be 10 hours. The samples are stored in PBS until imaged. As in section 1.2.3 the imaging buffer containing thiol (2-mercaptoethanol) and oxygen scavenger (GLOX) is added just before imaging. The protocol for immunostaining is explained in detail in Appendix D- Labelling the cells.

3.3 Instrumentation and software

This section is explained in section 1.3- Instrumentation and software. The protocol is the same for imaging actin as both experiments use STORM imaging and ThunderSTORM for reconstructing the images collected.

3.4 Results

Fig 3.1 is a 2D confocal image of F-actin obtained by Dr. Maria E. Teves and her research team and shows that F-actin is present in the acroplaxome but as it is not as sensitive as 3D STORM images, the structures in manchette are not visible. The 3D STORM images of phalloidin stained actin shows that F-actin is present in the acroplaxome and the manchette of the elongating spermatids. The blue and red red spots in fig 3.2 (c) are of about 50 to 70 nm in diameter and shows the localizations of F-actin in the acroplaxome in a step 10 spermatid and confirms in 3D that the acroplaxome is rich in F-actin. It can be observed that it is at the base of the nucleus and as per the color coding, it is seen to extend in depth from one end of the cell to atleast one-third of the cell. The exact depth is unknown as our system is limited to imaging 1 μm depth. The length of the acroplaxome in the image is 8.71 μm. The manchette is the region in green and is seen to extend from the acroplaxome region to the base of the cell. The larger ellipse-like yellow points of about 0.38 and 0.59 μm diameters are structures that have more specialized localizations. This proves that the manchette is also rich in F-actin. The region between the acroplaxome and the manchette is devoid of F-actin is the cytoplasm. Fig 3.3 (a) shows a step 11 spermatid. F-actin is more broadly distributed in the spermatid with larger localizations of about 0.5 to 1 μm size, as seen in fig 3.3 (b). It can be observed according to the color coding that manchette is present at the middle of the cell. The acroplaxome is rich in F-actin and hence is observed in yellow and green at the head portion of the cell as a uniformly distributed structure of about 8 μm in length.

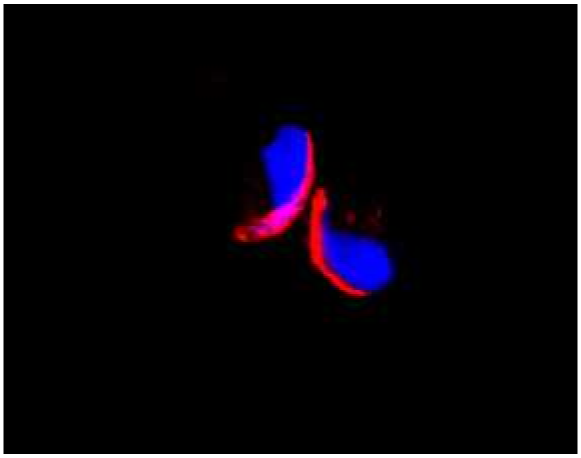

Figure 3.1: 2D confocal image of F-actin in step 14 spermatid. The region marked in the red shows the F-actin. It can be observed that only the acroplaxome shows F-actin distribution

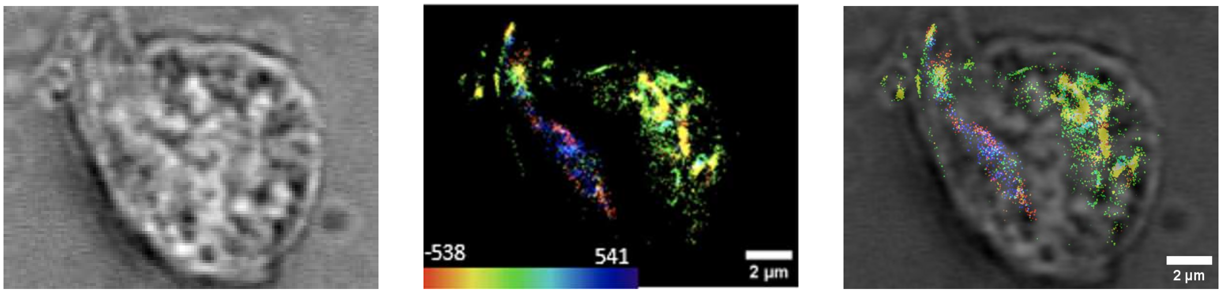

(a) (b) (c)

Figure 3.2: Actin structure in mouse spermatid at step 10 (a) Bright field image of a step 10 spermatid with background subtracted. (b) 3D STORM reconstructed image F-actin labeled with phalloidin-Alexa Fluor647 in spermatid cell shown in image a with the z-position information color coded.The reconstruction is colored according to the localization height as indicated in the color map. (c) Overlay of the bright field image a with the reconstructed image b. Scale bar is 2 μm

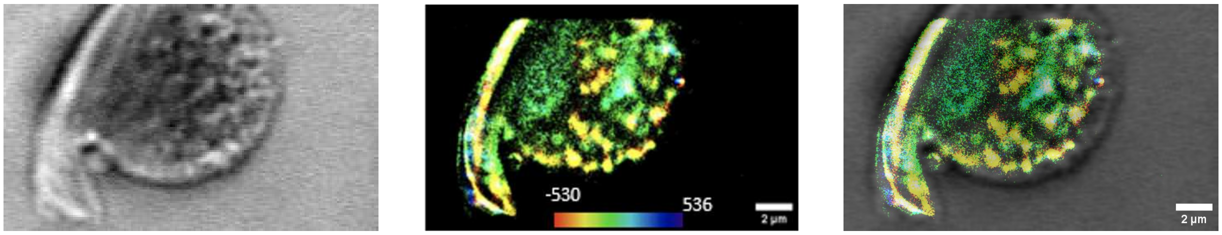

(a) (b) (c)

Figure 3.3: Actin structure in mouse spermatid at step 11 (a) Bright field image of a step 11 spermatid with background subtracted. (b) 3D STORM reconstructed image F-actin labeled with phalloidin-Alexa Fluor647 in spermatid cell shown in image a with the z-position information color coded. The reconstruction is colored according to the localization height as indicated in the color map. (c) Overlay of the bright field image a with the reconstructed image b. Scale bar is 2 μm

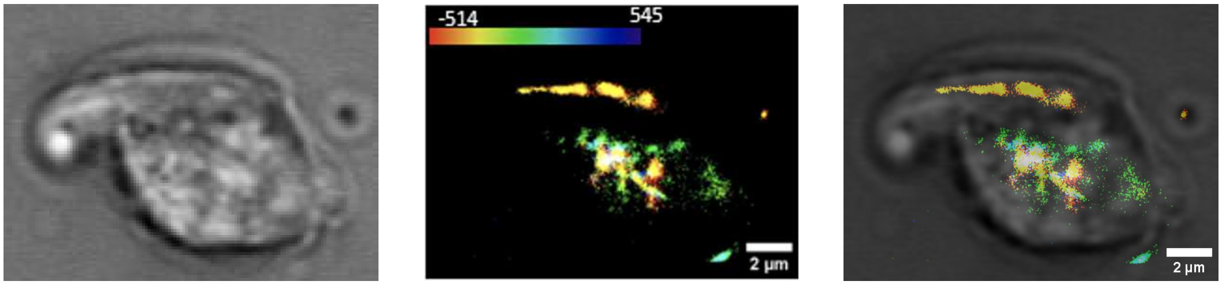

(a) (b) (c)

Figure 3.4: Actin structure in mouse spermatid at step 12 (a) Bright field image of a step 12 spermatid with background subtracted. (b) 3D STORM reconstructed image F-actin labeled with phalloidin-Alexa Fluor647 in spermatid cell shown in image a with the z-position information color coded.The reconstruction is colored according to the localization height as indicated in the color map. (c) Overlay of the bright field image a with the reconstructed image b. Scale bar is 2 μm

Fig 3.4 (a) shows a step 12 spermatid. On comparing images 3.4 (b) and 3.4 (c), it can be observed that the acroplaxome is present at the base of the nucleus. The uniform yellow and red structure of length 6 μm shows that F-actin is broadly distributed within the acroplaxome. Specific localizations of F-actin is observed in the manchette as yellow and red points of size 0.6 to 0.9 μm. In image 3.4 (b), the green localization close to the scale bar and the red point at the right of the image are fluorophores present on the coverslip, outside the cell, as can be observed in fig 3.4 (c). Fig 3.5 shows a step 13 spermatid. The structure to the right of the image in fig 3.4 (b) and (c) is the acrosome. It has detached partially from the cell during the mechanical agitation of the sample during preparation. From the color coding of the z positions, the machette is seen to be present at one end of the cell and gradually extending to at least one-third of the cell at the caudal region. On comparing image 3.4(c) and 3.5 (c), the manchette is observed to be reducing in diameter and is progressing down the cell and that the nucleus is getting shaped by the forces exerted by the acroplaxome and the manchette. It can be seen that the axoneme shows no F-actin. From fig 3.5 (c), the spermatid is seen to be almost devoid of cytoplasm, as is expected in the end stages of spermatid elongation or differentiation.

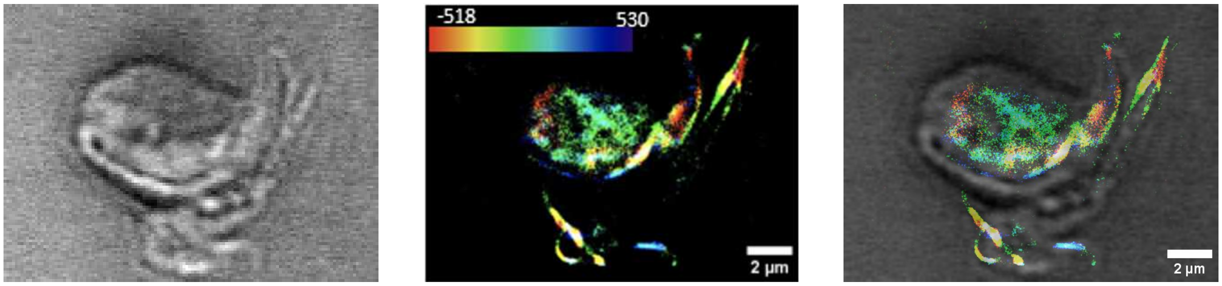

(a) (b) (c)

Figure 3.5: Actin structure in mouse spermatid at step 13 (a) Bright field image of a step 13 spermatid with background subtracted. It can be observed that the acrosome has partially detached from the anterior region of the cell (b) 3D STORM reconstructed image F-actin labeled with phalloidin-Alexa Fluor647 in spermatid cell shown in image a with the z-position information color coded. The reconstruction is colored according to the localization height as indicated in the color map. (c) Overlay of the bright field image a with the reconstructed image b. Scale bar is 2 μm

Chapter 4

Conclusion and Future work

In this thesis STORM was used as a tool to 3D localize the cytoskeleton in mouse spermatids. For this purpose, two set of experiments were conducted. The first one was to image αtubulin in spermatids. We observed that the manchette is an integral structure in elongating spermatids of steps 10 to 14 and that it disassemble at step 14. The αtubulin localizations in these spermatids were found to be interconnected in a mesh-like manner. It was observed that the manchette moves down the cell, reducing in diameter as the spermatids differentiate conforming that it is responsible for shaping the base of the nucleus and hence the spermatid head. The second set of experiments were conducted to image F-actin in spermatids. In order to do that, phalloidin stained Alexa Fluor 647 was used as phalloidin binds to F-actin and not G-actin and is excellent to use in aldehyde fixed cells. The results showed that the acroplaxome is rich in F-actin. 2D confocal images failed to image F-actin in manchette due to its poor sensitivity but our experiments showed that F-actin is present in the manchette. Moreover, the manchette and the acroplaxome were the only structures that showed an abundance of F-actin.

To the best of our knowledge, the cytoskeleton of spermatids has never previously been imaged with a super-resolution technique. While conducting the two set of experiments it was found that the results varied with the concentration of antibodies or molecules we stain the cells in the immunofluorescence protocol. After many trial and error, it was found that in imaging α tubulin, a primary antibody concentration of 1:200 in 1% BSA-PBS and a secondary antibody concentration of 1:700 dilution with 1% BSA-PBS , and an incubation time of 12 hours gives the desired rate of fluorophore blinking with minimum background signal and autofluorescence. The dilution of phalloidin conjugated Alexa Fluor 647 of 60 μl in 800 μl PBS incubated for 10 hours gave the best results. An incubation of over 10 hours showed to have excessive fluorescence thus generating much background signal and poor STORM reconstructions.

The astigmatism method we employed to expand the STORM technique to 3D capability poses a limited z range of 1 μm (-550 nm on one side and 550 nm on the other side). A spermatid cell has a width of around 3 μm, thus our imaging set-up was limited to obtaining about 1/3rd of the cell. This can be overcome using Tetrapod PSFs that outlines a tetrahedral shape in 3D as a function of the axial position of the fluorescing molecule [71, 72]. It has been optimized for single emitter localization by Fisher information maximization. There are two lobes to the tetrapod PSF that is separated by a distance that varies as a function of the emitter depth [73]. Depending on whether the emitter is above or beyond the focal plane, the axis along the separation of the two lobes rotates 90°. Experiment in Nehme et.al [74] used a Convolutional Neural Network (CNN) that optimally localizes the PSF and achieved an axial range of 5 μm. A phase mask is placed in the emission path of the microscope to encode each of the 3D point source to low-resolution 2D image. The CNN receives this 2D image of overlapping tetrapod PSFs and output a 3D grid that translate to 3D localizations.

In addition, multi-color imaging can be done by spectral demixing where two fluorescent probes are excited by the same laser wavelength and the overlapping emissions are seperated by dichroic splitter. Experiments [75–77] have used Alexa 647 and 700 as photoswitchable probes and band pass emission filters along with splitter dichroic to optimize crosstalk for spectral demixing and obtained separate populations of localization pairs. Extending that idea to this project would produce overlapping imaging of F-actin and tubulin, thus confirming that they are co-localized in the manchette structure. It can be also done by double labelling primary antibodies with an activator-reporter pair. The activator facilitates the photo-activation of the reporter, switching it between fluorescent and dark states by light of different wavelengths [78].

Bibliography

[1] Charles Coutton, Jessica Escoffier, Guillaume martinez, Christophe Arnoult, and Pierre F Ray. Teratozoospermia: spotlight on the main genetic actors in the human. *Human Reproduction Update*, 21(4):455–485, April 2015.

[2] Ya-Lan Wei and Wan-Xi Yang. The acroframosome-acroplaxome-manchette axis may function in sperm head shaping and male fertility. *Gene*, 660:28–40, 2018.

[3] N Kotaja. *Spermatogenesis, Mouse*, volume 6 of *Brenner's Encyclopedia of Genetics*. Elsevier, 2 edition, 2013.

[4] Maria Eugenia Teves and Eduardo R. S. Roldan. Sperm bauplan and function and underlying processes of sperm formation and selection. *Physiological reviews*, 102(1):7–60, January 2022.

[5] Jessica E. M. Dunleavy, Moira K. O'Bryan, Peter G. Stanton, and Liza O'Donnell. The cytoskeleton in spermatogenesis. *Reproduction*, 157(2):R53 – R72, 2019.

[6] Maria E. Teves, Eduardo R. S. Roldan, Diego Krapf, Jerome F. Strauss III, Virali Bhagat, and Paulene Sapao. Sperm differentiation: The role of trafficking of proteins. *International Journal of Molecular Sciences*, 21(10), May 2020.

[7] Christiane Pleuger, Mari S. Lehti, Jessica E. M. Dunleavy, Daniela Fietz, and Moira K. O'Bryan. Haploid male germ cells—the Grand Central Station of protein transport. *Human Reproduction Update*, 26(4):474–500, 04 2020.

[8] Abraham L. Kierszenbaum, Eugene Rivkin, and Laura L. Tres. Cytoskeletal track selection during cargo transport in spermatids is relevant to male fertility. *Spermatogenesis*, 1:221 – 230, 2011.

[9] Barry R. Zirkin and Erwin Goldberg. Spermatids. In Michael K. Skinner, editor, *Encyclopedia of Reproduction (Second Edition)*, pages 42–46. Academic Press, Oxford, second edition edition, 2018.

[10] Abraham L. Kierszenbaum, Eugene Rivkin, and Laura L. Tres. Acroplaxome, an f-actin–keratin-containing plate, anchors the acrosome to the nucleus during shaping of the spermatid head. *Molecular Biology of the Cell*, 14:4628–4640, November 2003.

[11] Abraham L. Kierszenbaum, Eugene Rivkin, and Laura L. Tres. The actin-based motor myosin va is a component of the acroplaxome, an acrosome-nuclear envelope junctional plate, and of manchette-associated vesicles. *Cytogenetic amd Genome Research*, 103:337–344, 2003.

[12] Abraham L. Kierszenbaum, Laura L. Tres, Eugene Rivkin, Ningling Kang-Decker, and Jan M. A. van Deursen. The acroplaxome is the docking site of golgi-derived myosin va/rab27a/bcontaining proacrosomal vesicles in wild-type and hrb mutant mouse spermatids. *Biology of Reproduction*, 70:1400–1410, January 2004.

[13] Abraham L. Kierszenbaum and Laura L. Tres. The acrosome-acroplaxome-manchette complex and the shaping of the spermatid head. *Archives of histology and cytology*, 67:271–84, 12 2004.

[14] Mari S. Lehti and Anu Sironen. Formation and function of the manchette and flagellum during spermatogenesis. *REPRODUCTION*, 151(4):R43 – R54, 2016.

[15] Kazuhiko Mochida, Laura L. Tres, and Abraham L. Kierszenbaum. Isolation of the rat spermatid manchette and its perinuclear ring. *Developmental Biology*, 200(1):46–56, 1998.

[16] Mark Bates, Sara Jones, and Xiaowei Zhuang. Stochastic optical reconstruction microscopy (STORM): A method for superresolution fluorescence imaging. *Cold Spring Harbor protocols*, June 2013.

[17] Mark Bates, Bo Huang, and Xiaowei Zhuang. Super-resolution microscopy by nanoscale localization of photo-switchable fluorescent probes. *Current Opinion in Chemical Biology*, 12:505–514, October 2008.

[18] Bo Huang, Hazen Babcock, and Xiaowei Zhuang. Breaking the diffraction barrier: super-resolution imaging of cells. *Cell*, 143(7):1047–58, December 2010.

[19] nature. Beyond the diffraction limit. *Nature Photonics*, 3(7):361–361, 2009.

[20] Eric Betzig, Jay K. Trautman, Timothy D. Harris, J. S. Weiner, and R. L. Kostelak. Breaking the diffraction barrier: Optical microscopy on a nanometric scale. *Science*, 251(5000):1468–1470, 1991.

[21] Sebastian van de Linde, Anna Löschberger A, Teresa Klein, Meike Heidbreder, Steve Wolter, Mike Heilemann, and Markus Sauer. Direct stochastic optical reconstruction microscopy with standard fluorescent probes. *Nature Protocols*, 6(7):991–1009, June 2011.

[22] Xinran Xu. *Super-resolution imaging and modeling of murine sperm during capacitation process*. PhD thesis, Colorado State University, 2019.

[23] Alexandros Pertsinidis, Yunxiang Zhang, and Steven Chu. Subnanometre single-molecule localization, registration and distance measurements. *Nature*, 466:647–51, 07 2010.

[24] Bo Huang, Wenqin Wang, Mark Bates, and Xiaowei Zhuang. Three-dimensional super-resolution imaging by stochastic optical reconstruction microscopy. *Science (New York, N.Y.)*, 319:810–3, 03 2008.

[25] Michael Rust, Mark Bates, and Xiaowei Zhuang. Sub-diffraction-limit imaging by stochastic optical reconstruction microscopy (storm). *Nature methods*, 3:793–5, 11 2006.

[26] Eric Betzig, George H. Patterson, Rachid Sougrat, O. Wolf Lindwasser, Scott Olenych, Juan S. Bonifacino, Michael W. Davidson, Jennifer Lippincott-Schwartz, and Harald F. Hess.

Imaging intracellular fluorescent proteins at nanometer resolution. *Science*, 313(5793):1642–1645, 2006.

[27] Ulrike Endesfelder and Mike Heilemann. Direct stochastic optical reconstruction microscopy (dstorm). *Methods in molecular biology*, 1251:263–76, 2015.

[28] Jianquan Xu, Hongqiang Ma, and Yang Liu. Stochastic optical reconstruction microscopy (storm). *Current Protocols in Cytometry*, 81(1):12.46.1–12.46.27, 2017.

[29] Mark Bates, Bo Huang, Graham T. Dempsey, and Xiaowei Zhuang. Multicolor super-resolution imaging with photo-switchable fluorescent probes. *Science*, 317(5845):1749–1753, 2007.

[30] Sebastian van de Linde, Anna Löschberger, Teresa Klein, Meike Heidbreder, Steve Wolter, Mike Heilemann, and Markus Sauer. Direct stochastic optical reconstruction microscopy with standard fluorescent probes. *Nature Protocols*, 6(7):991–1009, June 2011.

[31] Ursula Burner, Walter Jantschko, and Christian Obinger. Kinetics of oxidation of aliphatic and aromatic thiols by myeloperoxidase compounds i and ii. *FEBS Letters*, 443, 1999.

[32] Ursula Burner and Christian Obinger. Transient-state and steady-state kinetics of the oxidation of aliphatic and aromatic thiols by horseradish peroxidase. *Federation of European Biochemical Societies Letters*, 411:269–274, 1997.

[33] Ruth E. Benesch and Reinhold Benesch. Enzymatic removal of oxygen for polarography and related methods. *Science*, 118(3068):447–448, 1953.

[34] Ivan Rasnik, Sean A. McKinney, and Taekjip Ha. Nonblinking and long-lasting single-molecule fluorescence imaging. *Nature methods*, 3:891–3, 12 2006.

[35] Steve Wolterand Mark Schüttpelz, Marko Tscherepanow, Sebastian van de Linde, Mike Heilemann, and Markus Sauer. M. real-time computation of subdiffraction-resolution fluorescence images. *Jounal of Microscopy*, 237(1):12–22, January 2010.

[36] Mark Galassi, Jim Davies, James Theiler, Brian Gough, Gerald Jungman, Michael Booth, FabriceRossi, and Rhys Ulerich. Gsl-gnu scientific library: Reference manual. *Network Theory*, 01 2003.

[37] Sri Rama Prasanna Pavani, Michael A. Thompson, Julie S. Biteen, Samuel J. Lord, Na Liu, Robert J. Twieg, Rafael Piestun, and W. E. Moerner. Three-dimensional, single-molecule fluorescence imaging beyond the diffraction limit by using a double-helix point spread function. *Proceedings of the National Academy of Sciences*, 106(9):2995–2999, 2009.

[38] Gleb Shtengel, James A. Galbraith, Catherine G. Galbraith, Jennifer Lippincott-Schwartz, Jennifer M. Gillette, Suliana Manley, Rachid Sougrat, Clare M. Waterman, Pakorn Kanchanawong, Michael W. Davidson, Richard D. Fetter, and Harald F. Hess. Interferometric fluorescent super-resolution microscopy resolves 3d cellular ultrastructure. *Proceedings of the National Academy of Sciences*, 106(9):3125–3130, 2009.

[39] Grégory Clouvel, Audrius Jasaitis, and Xavier Levecq. Quasi-isotropic nanometric 3d resolution in palm/storm with the help of micao 3dsr. *Imagine Optic*, 2015.

[40] Eva Nogales and Gregory M. Alushin. Tubulin and microtubule structure: Mechanistic insights into dynamic instability and its biological relevance. In *Reference Module in Life Sciences*. Elsevier, 2017.

[41] Elizabeth I. Tang, Dolores D. Mruk, and C. Yan Cheng. Regulation of microtubule (mt)-based cytoskeleton in the seminiferous epithelium during spermatogenesis. *Seminars in cell & developmental biology*, 59:35–45, 2016.

[42] Ruoyu Cheng, Feng Zhang, Xiang Wo Meng Li, Yu-Wen Su, and Wei Wang. Influence of fixation and permeabilization on the mass density of single cells: A surface plasmon resonance imaging study. *Frontiers in Chemistry*, August 2019.

[43] Florian Hoff. How to prepare your specimen for immunofluorescence microscopy, 2022. [Online; accessed 4-September-2022].

[44] Kyuseok Im, Sergey Mareninov, M. Fernando Palma Diaz, and William H. Yong. An introduction to performing immunofluorescence staining: Methods and protocols. *Methods in molecular biology (Clifton, N.J.)*, 1897:299–311, 01 2019.

[45] abcam. Direct vs indirect immunofluorescence, 2022. [Online; accessed 4-September-2022].

[46] Alison J. Hobro and Nicholas I. Smith. An evaluation of fixation methods: Spatial and compositional cellular changes observed by raman imaging. *Vibrational Spectroscopy*, 91:31–45, 2017. Prominent Young Vibrational Spectroscopists.

[47] Monika Danchenko, Lucia Csaderova, Pierre Edouard Fournier, and Zuzana Sekeyova. Optimized fixation of actin filaments for improved indirect immunofluorescence staining of rickettsiae. *BMC Research Notes*, 12(1):657, 2019.

[48] abcam. Blocking for ihc, 2022. [Online; accessed 4-September-2022].

[49] Robert Sacher. Microscope immersion oil. *Microscopy Today*, 8(8):33–35, 2000.

[50] Wikipedia contributors. Oil immersion — Wikipedia, the free encyclopedia, 2022. [Online; accessed 4-September-2022].

[51] Nikon. Immersion oil – transparent high refractive index oil for microscopy, 2022. [Online; accessed 4-September-2022].

[52] ONI. Storm microscopy, 2022. [Online; accessed 5-September-2022].

[53] Ahmet Yildiz, Joseph N. Forkey, Sean A. McKinney, Taekjip Ha, Yale E. Goldman, and Paul R. Selvin. Myosin v walks hand-over-hand: single fluorophore imaging with 1.5-nm localization. *Science*, 300, June 2003.

[54] Ignacio Izeddin, Mohamed El Beheiry, Jordi Andilla, Daniel Ciepielewski, Xavier Darzacq, and Maxime Dahan. Psf shaping using adaptive optics for three-dimensional single-molecule super-resolution imaging and tracking. *Opt. Express*, 20(5):4957–4967, Feb 2012.

[55] Martin Ovesný, Pavel Křížek, Josef Borkovec, Zdeněk Švindrych, and Guy M. Hagen. ThunderSTORM: a comprehensive ImageJ plug-in for PALM and STORM data analysis and super-resolution imaging. *Bioinformatics*, 30(16):2389–2390, 05 2014.

[56] Michael J. Mlodzianoski, John M. Schreiner, Steven P. Callahan, Katarina Smolková, Andrea Dlasková, Jitka Santorová, Petr Ježek, and Joerg Bewersdorf. Sample drift correction in 3d fluorescence photoactivation localization microscopy. *Optics Express*, 19(16), August 2011.

[57] Wiley Analytical Science. Autofocus system from asi applied scientific instrumentation, 2022. [Online; accessed 5-September-2022].

[58] Applied Scientific Instrumentation. Crisp autofocus system, 2022. [Online; accessed 5-September-2022].

[59] Virali Bhagat. Spag17 is important for protein trafficking in mammalian afficking in mammalian spermiogenesis. Master's thesis, Virginia Commonwealth University, 2020.

[60] Tetsuji Soda, Yasushi Miyagawa, Shinichiro Fukuhara, and Hiromitsu Tanaka. Physiological role of actin regulation in male fertility: Insight into actin capping proteins in spermatogenic cells. *Reproductive Medicine and Biology*, 19(2):120–127, April 2020.

[61] Thomas Pollard and John Cooper. Actin, a central player in cell shape and movement. *Science (New York, N.Y.)*, 326:1208–12, 11 2009.

[62] Thomas A. Richards and Thomas Cavalier-Smith. Myosin domain evolution and the primary divergence of eukaryotes. *Nature*, 436(7054):1113–1118, 2005.

[63] Peter W. Gunning, Umesh Ghoshdastider, Shane Whitaker, David Popp, and Robert Charles Robinson. The evolution of compositionally and functionally distinct actin filaments. *Journal of Cell Science*, 128:2009 – 2019, 2015.

[64] Rajesh Arasada and Michael Schleicher. *Actin Cytoskeleton*, pages 5–8. Springer Berlin Heidelberg, Berlin, Heidelberg, 2006.

[65] Jaakko I Lehtimäki, Markku Hakala, and Pekka Lappalainen. Actin filament structures in migrating cells. *Handbook of experimental pharmacology*, 235:123–152, 2017.

[66] A. Wayne Vogl. Distribution and function of organized concentrations of actin filaments in mammalian spermatogenic cells and sertoli cells. volume 119 of *International Review of Cytology*, pages 1–56. Academic Press, 1990.

[67] Nikki P.Y. Lee and C. Yan Cheng. Ectoplasmic specialization, a testis-specific cell–cell actin-based adherens junction type: is this a potential target for male contraceptive development? *Human Reproduction Update*, 10(4):349–369, 07 2004.

[68] John A. Cooper. Effects of cytochalasin and phalloidin on actin. *The Journal of Cell Biology*, 105:1473–1478, October 1987.

[69] Francisco Capani, Thomas J. Deerinck, Mark H. Ellisman, Eric Bushong, Marketta Bobik, and Maryann E. Martone. Phalloidin-eosin followed by photo-oxidation: A novel method for localizing f-actin at the light and electron microscopic levels. *Journal of Histochemistry & Cytochemistry*, 49(11):1351–1361, 2001. PMID: 11668188.

[70] Puneet Gandhi and Richa Khare. A unique immunofluorescence protocol to detect protein expression in vascular tissues: Tacking a long standing pathological hitch. *Turkish Journal of Pathology*, 34:57–65, 2018.

[71] Yoav Shechtman, Steffen J. Sahl, Adam S. Backer, and W. E. Moerner. Optimal point spread function design for 3d imaging. *Phys. Rev. Lett.*, 113:133902, Sep 2014.

[72] Yoav Shechtman, Lucien Weiss, Adam Backer, Steffen Sahl, and William Moerner. Precise three-dimensional scan-free multiple-particle tracking over large axial ranges with tetrapod point spread functions. *Nano letters*, 15, 05 2015.

[73] Yoav Shechtman, Lucien Weiss, Adam Backer, Maurice Lee, and William Moerner. Multi-colour localization microscopy by point-spread-function engineering. *Nature Photonics*, 10, 08 2016.

[74] Elias Nehme, Daniel Freedman, Racheli Gordon, Boris Ferdman, Lucien Weiss, Onit Alalouf, Tal Naor, Reut Orange, Tomer Michaeli, and Yoav Shechtman. Deepstorm3d: dense 3d localization microscopy and psf design by deep learning. *Nature Methods*, 17:1–7, 07 2020.

[75] André Lampe, Volker Haucke, Stephan Sigrist, Mike Heilemann, and Jan Schmoranzer. Multi-colour direct storm with red emitting carbocyanines. *Biology of the cell / under the auspices of the European Cell Biology Organization*, 104:229–37, 12 2011.

[76] Leonid Andronov, Rachel Genthial, Didier Hentsch, and Bruno P. Klaholz. A spectral demixing method for high-precision multi-color localization microscopy. dec 2021.

[77] Andor. Multi-color direct storm with emccd camera technology, 2022. [Online; accessed 28-September-2022].

[78] Mark Bates, Bo Huang, Graham T. Dempsey, and Xiaowei Zhuang. Multicolor super-resolution imaging with photo-switchable fluorescent probes. *Science*, 317(5845):1749–1753, 2007.

Appendix A

Coating coverslips with Poly-L-lysine

This protocol is used for coating coverslips with Poly-L-lysine to promote adhesion of cultred spermatid cells onto coverslips

Materials:

- 1.5 ml centrifuge tubes
- Acetone
- Ethanol
- Deionized water
- 10% Poly-L-lysine
- 22x22 square coverslips
- glass coverslip holder

Procedure:

1. Wash the coverslips with acetone. Sonicate for 5 to 10 minutes.
2. Pour out the acetone and wash with ethanol. Sonicate for 5 to 10 minutes.
3. Pour out the ethanol and wash with deionized (DI) water. Sonicate for 5 to 10 minutes.
4. Pour out the DI water and wash with 10% Poly-L-lysine in DI Water. Incubate for 5 minutes.
5. Pour out the solution. Transfer the coverslips to a dry coverslip holder and dry them in an oven for 1 hour.
6. Use the coverslips the same day.

Appendix B

Preparing GLOX

The protocol is for the preparation of GLOX. It is a component of the imaging buffer added to sample before imaging. It is an oxygen scavenger and removes oxygen to prevent photobleaching. Since the enzymes oxidase and catalyze leads to acidification of the buffer over time, GLOX has to be prepared fresh every two weeks.

Materials:

- Glucose Oxidase from Aspergillus niger-Type VII, lyophilized powder,$\geq$ 100,000 units/g solid G2133- 250KU [Sigma-Aldrich]
- Catalase from bovine liver -lyophilized powder, $\geq$10,000 units/mg protein # C40-100MG [Sigma-Aldrich]
- Buffer A : 10 mM Tris (pH 8.0) + 50 mM NaCl

Procedure:

1. Measure the glucose oxidase. 14mg of oxidase gives 250 μl of GLOX solution.
2. Measure catalyze and make a dilution of 17 mg per 1 ml DI water. Add 50 μl of this for 250 μl GLOX.
3. Add 200 μ of Buffer A for 250 μl GLOX.
4. Use the GLOX solution within two weeks.

Appendix C

Collecting and fixing spermatid cells from mice

Spermatids are collected from at mice that is at least 5 weeks old. Sample preparation and cell fixation steps are listed in the protocol.

Materials:

- DNAse (StemCell 07469): stock buffer, 1 mg/ml in PBS
- Collagenase type IA (Sigma C9891)
- Dulbecco's Modified Eagle Medium (DMEM) #21063 [Invitrogen]
- Phosphate-Buffered Saline (PBS), 1×
- Sucrose
- Paraformaldehyde

Procedure:

1. Prepare isolation buffer for spermatids by mixing 5 μl of DNAse, 5ml of DMEM and 2.5 mg of collagenase in a conical tube.
2. Add 1 ml DMEM to an eppendorf tube and store on ice.
3. Euthanize a mouse of at least 5 weeks age and collect testes. Store the testes in the 1 ml DMEM solution.
4. Make a small vertical cut to each testis and squeeze the contents out using a tweezer into the isolation buffer.
5. Incubate the sample at 32°C for 30 minutes. Gently pipette the solution every 8 minutes during this incubation time to break the tissue but not the cells.

6. Centrifuge the sample at 1000 rpm for 5 minutes at 4°C. Aspirate the supernatant and add 5 ml PBS to the sample and shake gently to suspend the sample in PBS.
7. Repeat the step 6. Follow the protocol for the respective protein.

A) Tubulin:

8. Centrifuge the sample once again at 1000 rpm for 5 minutes and add freshly prepared fixative solution made of 0.1M Sucrose and 4% Paraformaldehyde in PBS and shake gently for 15 minutes.
9. Centrifuge the sample at 800 rpm for 5 minutes at 4°C. Aspirate the solution and wash with 5 ml PBS.
10. Repeat the step 8. Centrifuge again at 800 rpm for 5 minutes and add 2 ml PBS and suspend the cells by gently shaking.
11. Check the cell density with a sample slide and adjust the dilution with PBS if necessary.
12. Transfer the cells to Poly-L-lysine coated coverslips. Draw a circle with oil pen on the coverslips to make a hydrophobic boundary for the samples.
13. Pipette 50 μl of sample solution onto each coverslip. Wait for 25 to 35 minutes to allow the samples to semi-dry. Check by tilting the coverslips. The sample should not have solution running or dry. From this step make sure that the samples do not get dry.

B) Phalloidin

8. Centrifuge the sample once again at 1000 rpm for 5 minutes and add 2 ml PBS and suspend the cells by gently shaking.
9. Check the cell density with a sample slide and adjust the dilution with PBS if necessary.

10. Transfer the cells to Poly-L-lysine coated coverslips. Draw a circle with oil pen on the coverslips to make a hydrophobic boundary for the samples.

11. Pipette 50 μl of sample solution onto each coverslip. Wait for 25 to 35 minutes to allow the samples to semi-dry. Check by tilting the coverslips. The sample should not have solution running or dry. From this step make sure that the samples do not get dry.

Appendix D

Labelling the cells- Immunostaining protocol

The protocol discusses steps in immunostaining protocol for tubulin, and Alexa 647phalloidin to stain the cytoskeleton by binding to actin. The tubulin immunostaining follows indirect labelling.

Materials:

- Goat serum (VWR 101098-382)
- Phosphate-Buffered Saline (PBS), 1×
- Triton X-100
- Bovine Serum Albumin
- α tubulin - primary antibody
- anti-rabbit - secondary antibody
- 2-Mercaptoethanol # 63689-100ML-F [Sigma-Aldrich]
- Buffer B : 50 mM Tris-HCI (pH 8.0) + 10 mM NaCl + 10% Glucose
- GLOX solution (250 μl)
- Gluteraldehyde
- Cytoskeleton buffer
- Sodium Borohydride - $NABH_4$

Procedure:

A) Tubulin:

1. Permeabilize the cells with 1% Triton at room temperature for 5 minutes .
2. Wash the samples with 100 μl PBS three times without wait time in between.
3. Prepare blocking buffer with 10% Goat serum in PBS, 3% BSA and 0.2%Triton. Add 100 μl to each coverslip and incubate for 1 hour.
4. Prepare primary antibody solution of 1:200 dilution of α tubulin in 1% BSA in PBS and 10% Goat serum. Add 100 μl onto each coverslip.
5. Store the samples in an aluminum foil box overnight in a moisture chamber at 4°C.
6. After 12 hours of overnight incubation, wash the samples with 100 μl PBS three times with 10 minutes wait time.
7. In a dark room, prepare the secondary antibody solution of 1:700 dilution of anti-rabbit with 1% BSA in PBS and 10% Goat serum. Add 100 μl onto each coverslip and incubate for 1 hour at room temperature. From this step, make sure that the samples are not exposed to light.
8. Wash the samples with 100 μl PBS three times with 10 minutes wait time.
9. If not used immediately, store the samples in 100 μl PBS at 4°C until ready to be imaged.
10. Before imaging, aspirate the PBS solution from the samples and add 4 to 5 μl of imaging buffer made of 690 μl Buffer B, 7 μl of 2-mercaptoethanol and 7 μl of GLOX.
11. Mount the coverslip on a slide and image immediately.

B) Phalloidin:

1. Fix the cells with 0.3% glutaraldehyde and 0.25% Triton in Cytoskeleton Buffer (CB) for 2 minutes.
2. . Wash the samples with CB thrice with 5-minute wait time in between.

3. Add 100 μl of 2% glutaraldehyde in CB and wait for 15 minutes.
4. Wash with CB twice with a wait time of 10 minutes.
5. Add 100 μl of freshly prepared 1% NABH4 in PBS and incubate for 7 minutes.
6. Wash with CB twice with 5-minute wait time in between. 7
7. Prepare a fresh Phalloidin solution by adding 60 μl of Alexa Fluor-647 for Phalloidin and 800μl of PBS and add 100μl to each sample.
8. Store the samples in an aluminum foil box overnight in a moisture chamber at 4°C.
9. After 10 hours of overnight incubation, wash the samples with 100 μl PBS three times with 10 minutes wait time.
10. If not used immediately, store the samples in 100 μl PBS at 4°C until ready to be imaged.
11. Before imaging, aspirate the PBS solution from the samples and add 4 to 5 μl of imaging buffer made of 690 μl Buffer B, 7 μl of 2-mercaptoethanol and 7 μl of GLOX.
12. Mount the coverslip on a slide and image immediately.

Appendix E

Protocol for aligning a TIRF microscope

The imaging set-up uses TIRF microscope. The laser and microscope has to be aligned before every experiment to obtain good quality images. The protocol discusses the alignment of red laser beam. Violet laser (405 nm) is also used in the experiment for the purpose of reactivating flurophores.

(A) Aligning a LASER

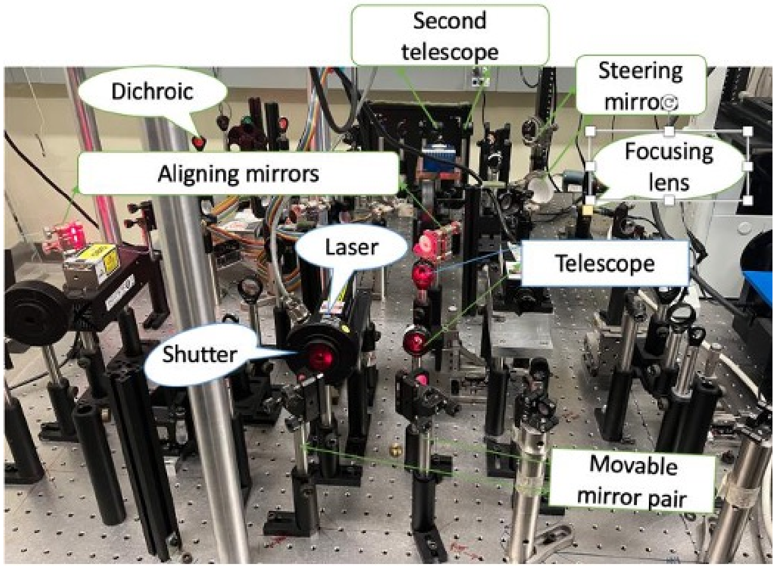

Figure E.1: Components of TIRF microscope.

Fig E.1 shows the components of the red laser in the TIRF room. The path of the laser beam is marked on the table, and it travels from the laser cavity to the microscope in the order in which the components are numbered in the protocol.

1. LASER- The laser emits light of wavelength 641.5 nm.

2. SHUTTER- This can be operated manually or through NIS elements software. An ND filter can be placed while aligning to reduce the intensity of light, but it must be placed at an angle such that the reflected beam does not travel back into the laser cavity.

3. MOVABLE MIRROR PAIRS- On the table, place the first mirror such that the laser beam reflects off its center and the mirror is angled at 45 degrees to its stand. Use an aperture for this alignment. Now place the second mirror such that the beam hits the center of the mirror and is also laterally and vertically aligned at all points between the two mirrors. Use a tall stand with a sticky note to check the alignment. If you notice that the beam is shifting, move the second mirror to a better location and use the knobs on the first mirror for fine adjustments.

4. TELESCOPE- Once the beam is aligned until the telescope, laser beam should be centered at the first telescopic lens. Use apertures to ensure that the beam is centered and that it maintains the same height and lateral position. Also check for reflections and make sure they align with the laser beam on the lens. Place the second lens of the telescope such that the distance between the lenses is the sum of their focal lengths. For alignment, use the knobs on the xyz stand that the second lens is mounted on.

The beam emerging from the telescope should be collimated. If the beam appears to be shrinking, the lenses are too far and if the beam expands, the lenses are too close together. Once the beam is collimated and is aligned laterally and vertically, move to the next step.

5. ALIGNING MIRRORS- To allow multiple lasers to illuminate the microscope, the LASERS follow the same path from the set of dichroics to the microscope as shown in Fig E.2. This protocol will refer to this section of shared path as the “main line”. The alignment microscope allows this shared path by aligning the beam along the main line.

The first aligning mirror should be placed such that it is at 45-degree angle to its stand and the beam is centered. The beam should be collimated and aligned at all points between the mirror and the second telescopic lens. If not, go back to section 4. The second mirror should have the beam centered and follow the alignment and collimation conditions. Use the knobs on the first mirror to make any fine adjustments.

6. DICHROIC-The dichroic passes only a specific wavelength. The beam should be centered at the dichroic as well.

(A.1) Aligning the “main line”:

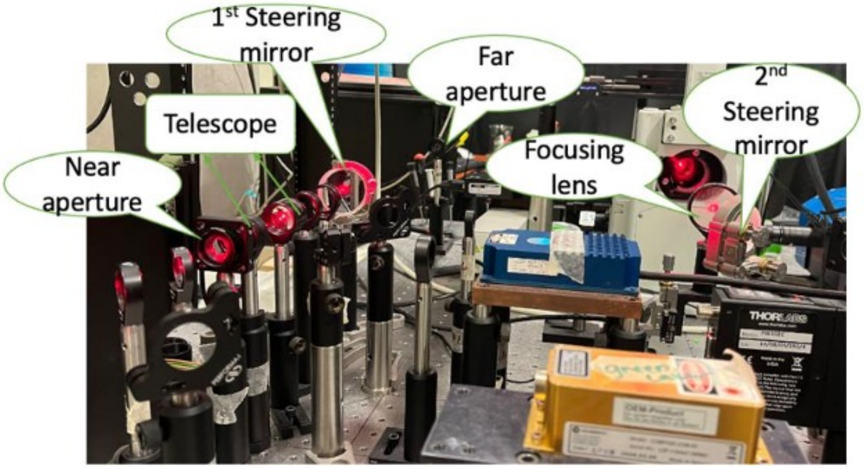

Figure E.2: The shared path of LASERs – “main line”

Due to drifts, the laser alignment may vary, especially at the main line and should be re-adjusted before imaging.

a) Remove the first steering mirror and the two telescopic lenses of the second telescope before aligning the laser through the main line.

b) There are two apertures in the main line as marked in Fig E.2. The steering mirror diagonal to the aperture is used to align the beam through it, that is, the aligning mirror on the right side of the table (next to the first telescope) in Fig E.1 is used for near aperture and the aligning mirror on the left side (before the dichroic) aligns the laser beam at the far aperture. If you see that the alignment gets only worse after a few iterations, switch the aligning mirrors- mirror on the left for near and the one on the right for far.

Use the right aligning mirror to center the beam at the near aperture. This will move the beam farther from the far aperture. Center the beam at the far aperture using the left aligning mirror. That will cause the beam to go off -center at near aperture. Adjust the aligning mirrors in this manner until the beam is centered at both the apertures.

7. SECOND TELESCOPE- Place the telescopic lenses such that the laser beam is centered at them both, aligned at all points between them and the lenses are at a distance equal to the sum of their focal lengths. Check for collimation and adjust the length of the telescope accordingly.

Once the beam appears to be collimated and aligned throughout the table, place the first steering mirror back such that the beam is centered on it. Remove the focusing lens from its stand and proceed to the next step.

(B) Aligning the microscope

a) Place an SM1 tube with an aperture on each end, on the objective holder to align the laser beam along the microscope.

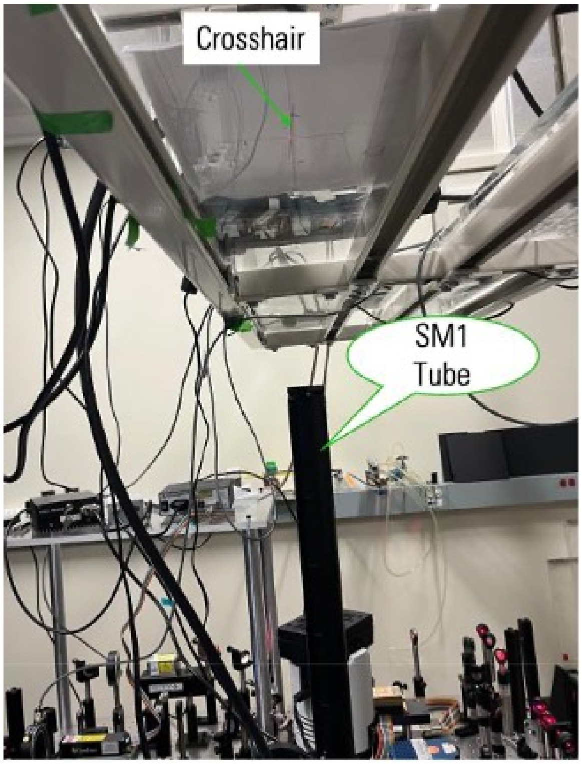

Figure E.3: Positioning the crosshair for reference

8. STEERING MIRRORS- The first steering mirror aligns the bottom aperture of the tube, and the second steering mirror aligns the top aperture. Close the near aperture in the main line to reduce the size of the beam.

b) Open and close the bottom aperture and check if the beam is centered and opens and closes uniformly. If not, you will see that one side of the beam disappears and appears earlier than the

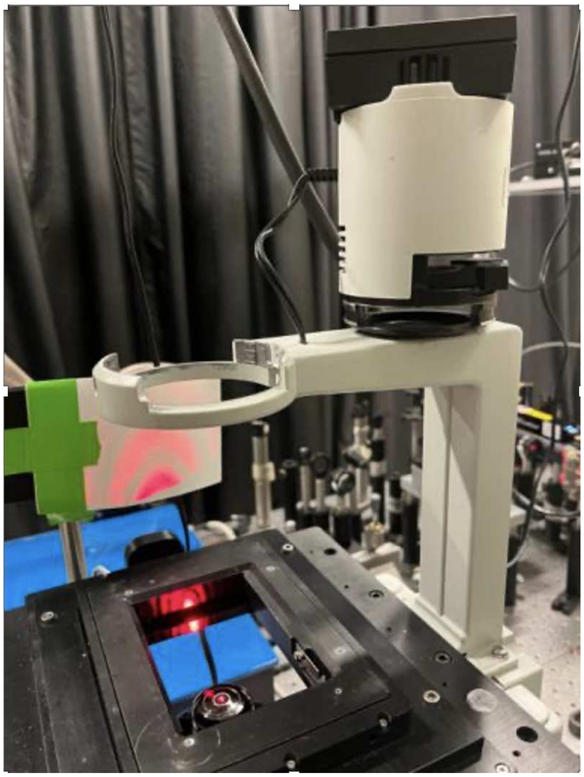

Figure E.4: Laser beam in close to TIRF

other sides and the center of the beam is not at the exact center of the aperture. Use the knobs on the first aligning mirror to center the beam at the bottom aperture.

c) Follow the same steps for aligning the top aperture and repeat the process until the beam passes through the center of both the apertures.

d) Once the apertures appear to open and close uniformly, place a piece of paper with a crosshair marked such that it is centered at the beam (red dot on Fig E.3) and do not move the paper afterwards as it is the reference to the desired position of laser beam.

e) Keep the focusing lens back in its position and replace the SM1 tube with a 100X objective.

9. FOCUSING LENS – Place an aperture on the focusing lens during alignment. The lens is placed on a micrometer that can be moved in the xyz direction.

f) Adjust the position of the focusing lens such that the beam is centered on it and its reflection aligns with the beam on the second aligning mirror.

g) Use the micrometer knobs to center the beam on the ceiling back to the crosshair. The beam will now be off center at the focusing lens but do not move the focusing lens or its knobs.

h) Use the first steering mirror to re-center the beam on the focusing lens. This will move the beam away from the crosshair. Use the second steering mirror to center the beam on the crosshair. Repeat these steps until the beam is centered at the focusing lens and at the crosshair.

i) Now use the knob at the side of the micrometer to move the laser beam towards the microscope to bring to 'close to TIRF'. Position it at the slide stand as shown in Fig E.4. The TIRF microscope is now aligned.

Appendix F

3D STORM Calibration Protocol

The protocol is used to prepare the calibration samples and perform the calibration experiment for MicAO optical optimization, and for obtaining the look up tables for 3D STORM reconstruction.

F.1 Preparing Calibration sample

Materials:

- 0.1 μm TetraSpeckTM fluorescent microspheres (Invitrogen 2155302)
- Acetone
- Ethanol
- Deionized water
- Phosphate-Buffered Saline (PBS), 1×
- 1.5 ml centrifuge tubes
- 22x22 square coverslips (Poly-lysine coating recommended)
- 75X25 Glass slides
- Fast dry nail polish
- Aluminum foil covered petridish

Procedure:

1. Clean coverslips using Acetone, ethanol and DI water as discussed in the first three steps of Appendix A- Coating coverslips with Poly-L-Lysine protocol.
2. In a centrifuge tube dilute Tetraspeck beads in 1:1000 dilution in PBS.

3. Sonicate the centrifuge tube.

4. Pipette 500 ml of the prepared sample 2onto a cleaned coverslip and incubate for 5 minutes.

5. Aspirate the beads solution leaving 15 to 30 μl on the coverslip.

6. Place the coverslip on the center of a slide using a tweezer, making sure that you place the sample side down on the coverslip. Gently press down the coverslip with a Kimwipe. Seal the edges with nail polish.

F.2 Calibrating the MicAO

1. Turn on the cooling system for the camera and then turn the camera, MCL Piezo and ASI on.

2. Open MicAO local and choose the baseline mirror shape file- closedloopCasao.has, from installation files.

3. Open NIS Elements and choose the imaging settings as shown in fig F.1 and ensure that the file path is correct. Save the images as Tiff files.

4. Select Time series under Acquisition tab and ensure that the imaging delay is 450ms, the Run Duration is continuous, and macro settings is in 'Execute after every phase' as shown in fig5.

5. Allow the system to warm up for 15 minutes.

6. In MicAO, open the Diagnostics tab to see the PSF of any selected bead.

7. Under Optimizations, choose Focus, D3th order spherical aberration and D5th order aberration, as shown in fig F.2.

8. Turn off the laser using shutter in NIS Elements, put an ND2 filter in the path of the red laser.

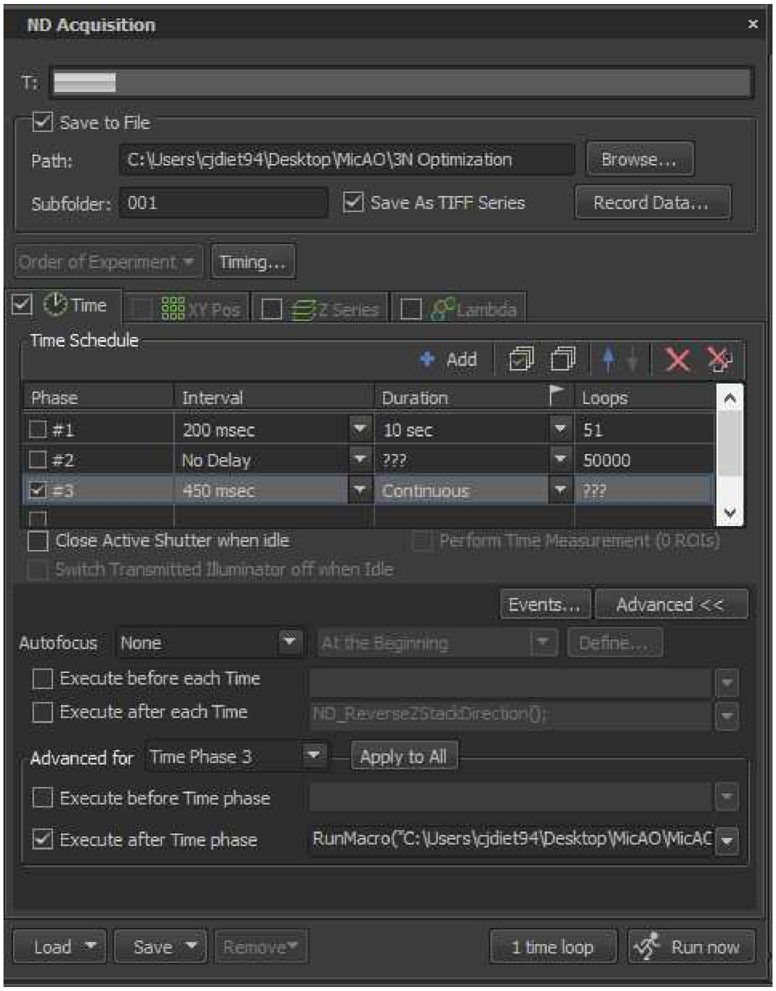

T:

☑ Save to File

Path: C:\Users\cjdiet94\Desktop\MicAO\3N Optimization

Subfolder: 001

☑ Save As TIFF Series

☑ Time ☐ XY Pos ☐ Z Series ☐ Lambda

Time Schedule

Phase	Interval	Duration	Loops
☐ #1	200 msec	10 sec	51
☐ #2	No Delay	???	50000
☑ #3	450 msec	Continuous	???
☐			

☐ Close Active Shutter when idle

☐ Perform Time Measurement (0 ROIs)

☐ Switch Transmitted Illuminator off when Idle

Autofocus: None — At the Beginning

☐ Execute before each Time

☐ Execute after each Time: ND_ReverseZStackDirection();

Advanced for: Time Phase 3

☐ Execute before Time phase

☑ Execute after Time phase: RunMacro("C:\Users\cjdiet94\Desktop\MicAO\MicAC

Figure F.1: Imaging settings for obtaining PSF

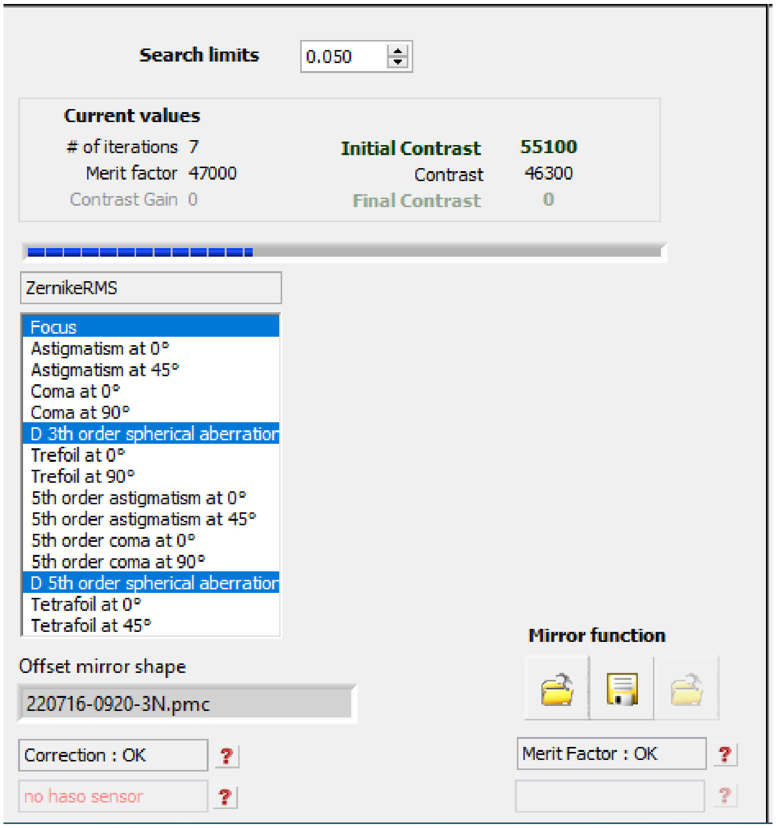

Search limits 0.050

Current values

\# of iterations 7
Merit factor 47000
Contrast Gain 0

Initial Contrast 55100
Contrast 46300
Final Contrast 0

ZernikeRMS

Focus
Astigmatism at 0°
Astigmatism at 45°
Coma at 0°
Coma at 90°
D 3th order spherical aberration
Trefoil at 0°
Trefoil at 90°
5th order astigmatism at 0°
5th order astigmatism at 45°
5th order coma at 0°
5th order coma at 90°
D 5th order spherical aberration
Tetrafoil at 0°
Tetrafoil at 45°

Offset mirror shape 220716-0920-3N.pmc

Mirror function

Correction : OK
no haso sensor
Merit Factor : OK

Figure F.2: MicAO settings to obtain PSF without aberrations

9. Put a drop of objective oil on 100x objective and turn off the light. Put the calibration sample (coverslip down) under the microscope and secure with slide clips. Bring the objective up until the oil interacts with the sample.

10. Set the exposure to 15ms and gain to 10 and turn on bright field light.

11. Find the surface by turning the focusing knobs of microscope and locating the position with maximum brightness.

12. Turn off the bright field light and set the exposure to 400ms and gain to 7. Click on Green play button in NIS Elements for live image window.

13. Locate an isolated bead with good fluorescence.

14. Adjust the ROI around the bead to 50x50 pixels and focus the bead.

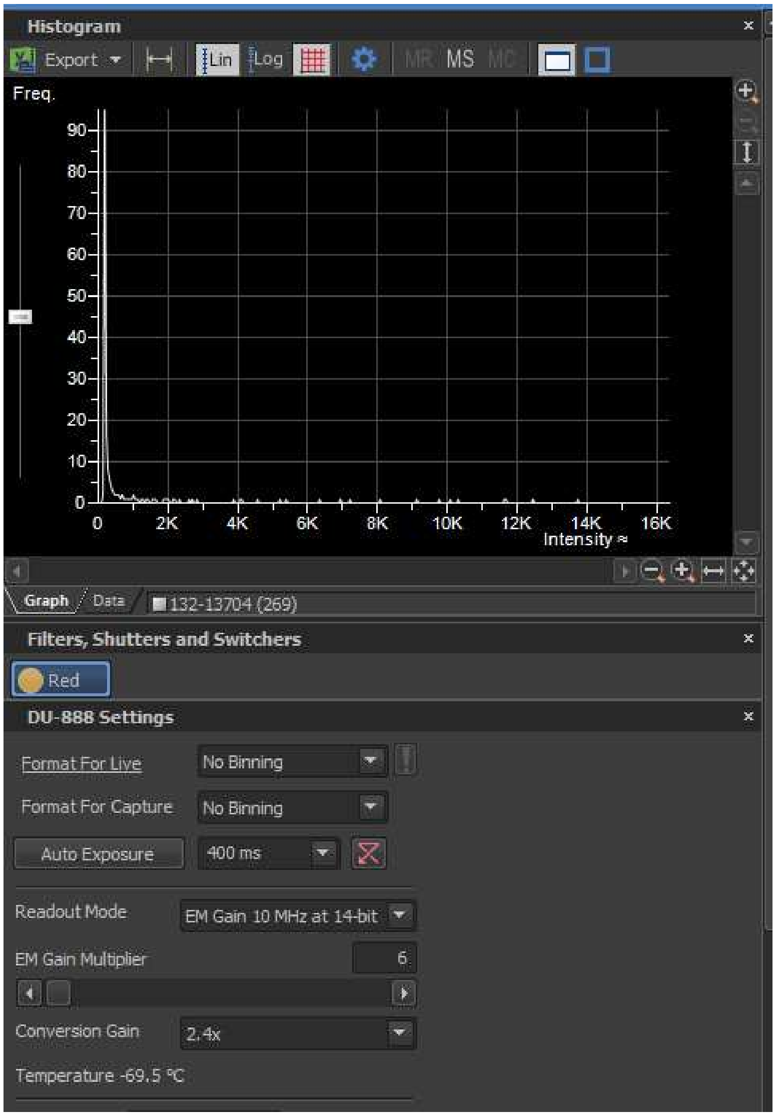

Format For Live: No Binning
Format For Capture: No Binning
Auto Exposure: 400 ms
Readout Mode: EM Gain 10 MHz at 14-bit
EM Gain Multiplier: 6
Conversion Gain: 2.4x
Temperature -69.5 ℃

Figure F.3: Gain and exposure settings for calibration

15. Adjust exposure between 400 to 450 ms and gain until the bead is not saturating but the histogram is utilized maximum as shown in fig F.3.

16. Under Acquisition, click on 'Run Now' and click on the yellow play button in MicAO to obtain PSF. Click on green checkmark after the optimizations are completed.

17. Compare the final contrast with the initial contrast. Check the PSF to see if it has improved. If it has and the final contrast is lower, the bead may be bleaching. If the bead is bleaching, move on to the next bead and repeat step 12 to 15.

18. Repeat steps 15 and 16 until the PSF is clean and spherical and the current optimization is not improving much. Make sure that the pistons in MicAO are not maxing out to -1 or +1 by checking mirror shape as shown in fig F.4.

Search limits 0.050

Current values
# of iterations 25
Merit factor 52100
Contrast Gain 0
Initial Contrast 53300
Contrast 51500
Final Contrast 0

ZernikeRMS

- Focus
- Astigmatism at 0°
- Astigmatism at 45°
- Coma at 0°
- Coma at 90°
- D 3th order spherical aberration
- Trefoil at 0°
- Trefoil at 90°
- 5th order astigmatism at 0°
- 5th order astigmatism at 45°
- 5th order coma at 0°
- 5th order coma at 90°
- D 5th order spherical aberration
- Tetrafoil at 0°
- Tetrafoil at 45°

Offset mirror shape 220716-0920-3N.pmc

Correction : OK

no haso sensor

Merit Factor : OK

		0.128	0.072	-0.254	0.173		
	-0.137	-0.018	-0.015	0.102	-0.001	0.117	
0.001	-0.001	0.067	-0.013	-0.023	0.022	-0.110	-0.441
0.055	0.165	-0.014	0.027	-0.001	-0.025	0.378	-0.027
-0.389	-0.000	-0.007	0.061	-0.007	0.086	0.032	-0.301
0.126	0.212	-0.072	-0.006	0.070	0.084	-0.222	-0.167
	-0.434	0.035	-0.107	-0.022	0.138	0.187	
		0.512	0.264	-0.064	-0.525		

mirao 52-e :
back side view

Figure F.4: Mirror shape in MicAO

19. Under Optimizations, select all options from Focus to Trefoil at 90° as shown in fig F.5. Repeat steps 12 to 17.

20. Once the PSF looks good, save the mirror shape file. Now select the mirror shape file you just saved and click on apply.

21. Select the Open Loop tab in MicAO and click on yellow play button. It will turn to a green check mark. Change the Astigmatism settings to -0.06 um as shown in Fig F.6.

22. Check the astigmatism of a bead by adjusting the focus. The bead should be in a perfect plus sign when in focus, as shown in fig F.7 a. When turning the focusing knobs, it should elongate and shrink only in horizontal in one direction of focus, as in fig F.7 b and only in vertical in the other direction of focus, as in fig F.7 c.

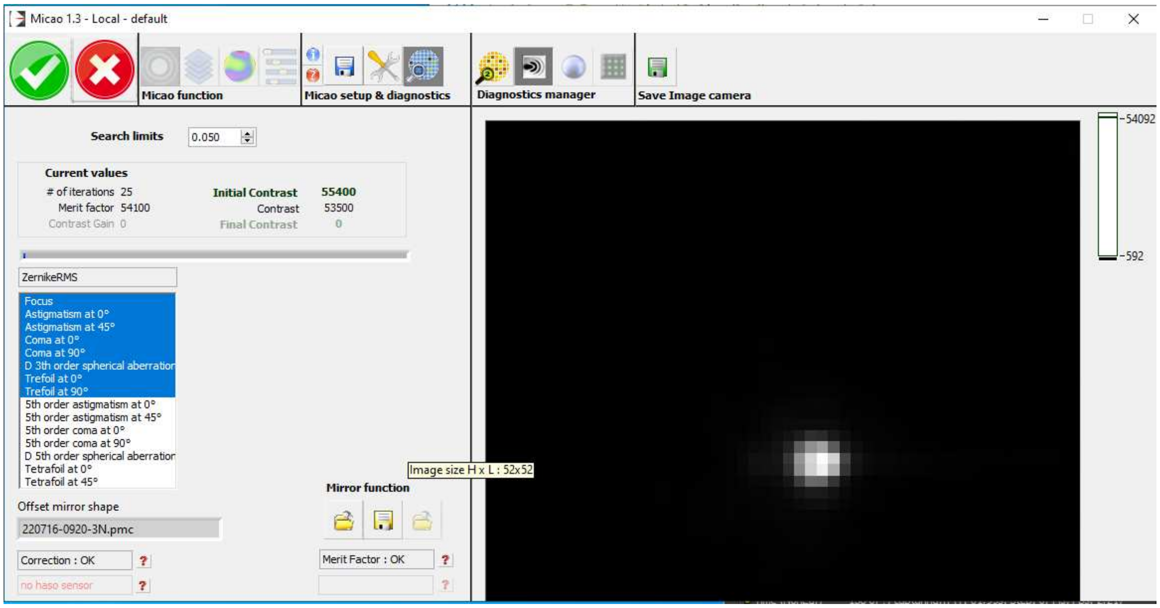

Search limits 0.050

Current values
# of iterations 25
Merit factor 54100
Contrast Gain 0
Initial Contrast 55400
Contrast 53500
Final Contrast 0

ZernikeRMS

Focus
Astigmatism at 0°
Astigmatism at 45°
Coma at 0°
Coma at 90°
D 3th order spherical aberration
Trefoil at 0°
Trefoil at 90°
5th order astigmatism at 0°
5th order astigmatism at 45°
5th order coma at 0°
5th order coma at 90°
D 5th order spherical aberration
Tetrafoil at 0°
Tetrafoil at 45°

Image size H x L : 52x52

Offset mirror shape 220716-0920-3N.pmc

Correction : OK

no haso sensor

Merit Factor : OK

Figure F.5: Settings for obtaining PSF

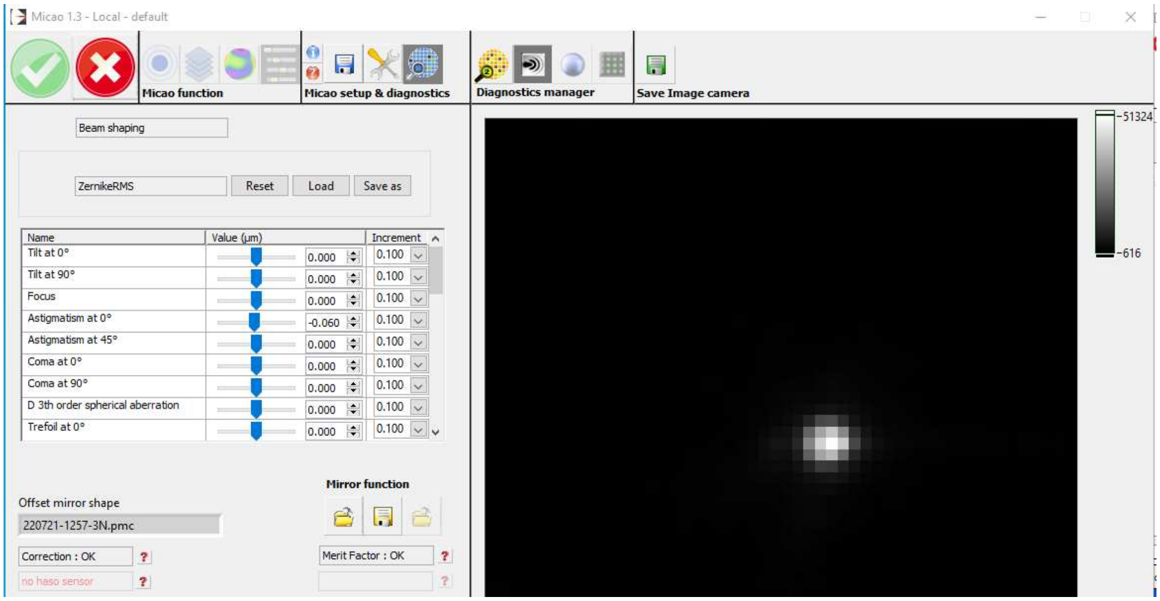

Beam shaping

ZernikeRMS

Name	Value (µm)	Increment
Tilt at 0°	0.000	0.100
Tilt at 90°	0.000	0.100
Focus	0.000	0.100
Astigmatism at 0°	-0.060	0.100
Astigmatism at 45°	0.000	0.100
Coma at 0°	0.000	0.100
Coma at 90°	0.000	0.100
D 3th order spherical aberration	0.000	0.100
Trefoil at 0°	0.000	0.100

Offset mirror shape 220721-1257-3N.pmc

Correction : OK

no haso sensor

Merit Factor : OK

Figure F.6: Astigmatism settings in MicAO

23. If the astigmatism does not look good, repeat steps 7 to 21 with a reference mirror shape that has worked well before.

24. Turn off the laser. Remove ND2 from the laser path. Change the imaging path and deselect Tiff option.

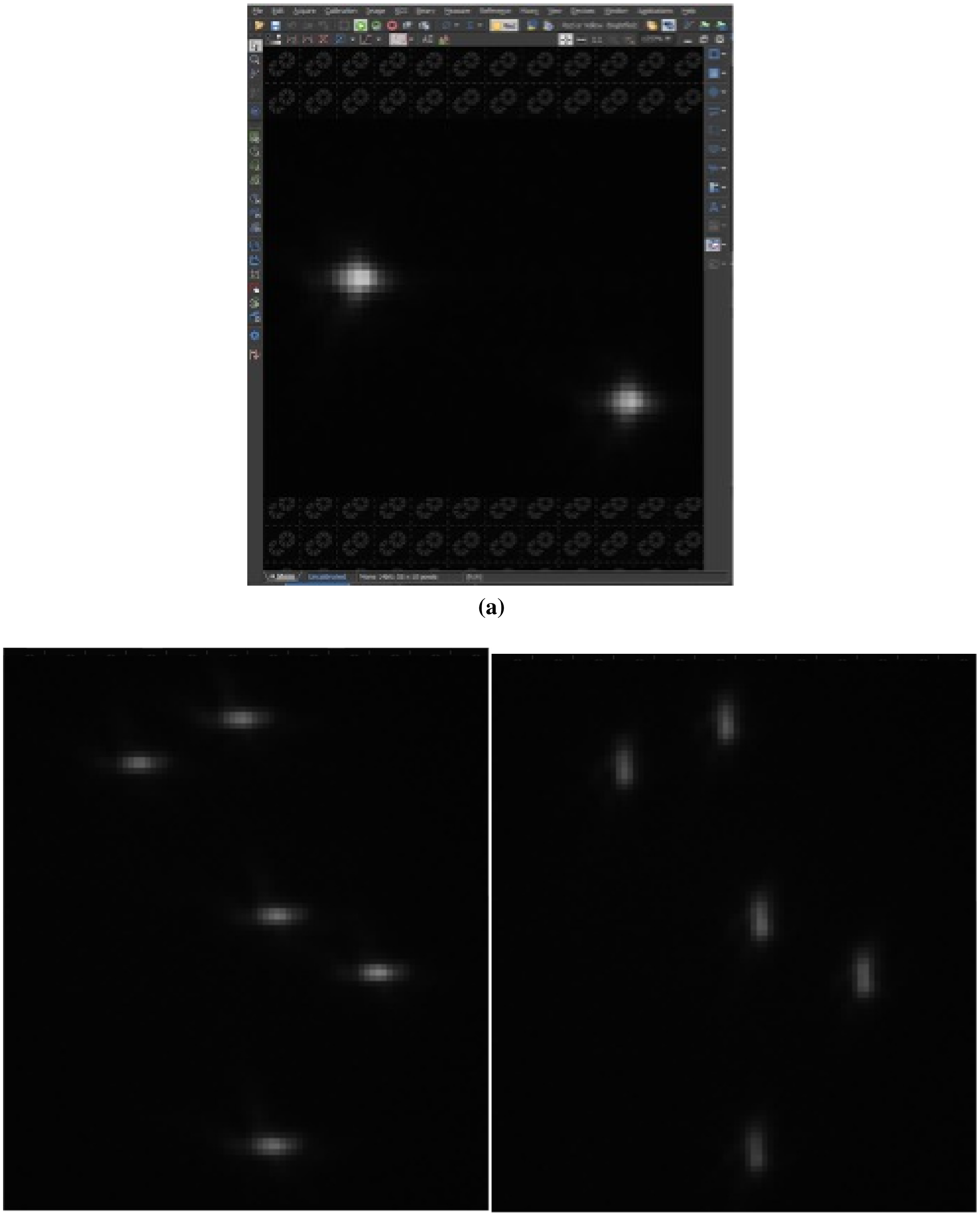

(a)

(b) (c)

Figure F.7: Checking the PSF of beads (a) Beads in focus (b) Beads elongated horizontally (c) Beads elongated vertically

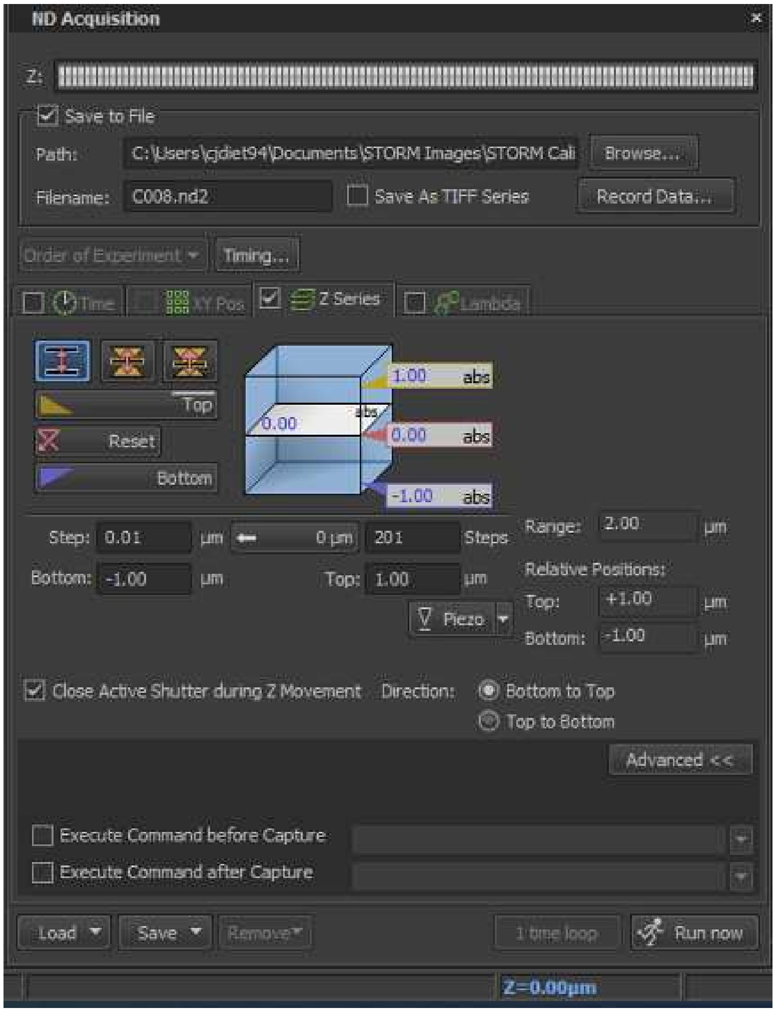

☑ Save to File
Path: C:\Users\cjdiet94\Documents\STORM Images\STORM Cali
Filename: C008.nd2
☐ Save As TIFF Series

☐ Time ☐ XY Pos ☑ Z Series ☐ Lambda

Step: 0.01 µm 0 µm 201 Steps
Bottom: -1.00 µm
Top: 1.00 µm
Piezo
Range: 2.00 µm
Relative Positions:
Top: +1.00 µm
Bottom: -1.00 µm

☑ Close Active Shutter during Z Movement
Direction: ● Bottom to Top
○ Top to Bottom

☐ Execute Command before Capture
☐ Execute Command after Capture

Figure F.8: Settings to capture calibration movies

25. Select only Z series option and make sure the settings are as shown in fig F.8.
26. Locate a group of 5 to 10 beads that are not overlapping but are close in proximity and draw and ROI around the group.
27. Adjust exposure between 400 to 450 ms and gain until the bead is not saturating but the histogram is utilized maximum as shown in fig 7. Click on ‘Run Now’ and note down the gain and exposure values for reconstruction.
28. Repeat steps 25 and 26 until you have about 10 good calibration movies.

Appendix G

Finding and imaging spermatid

The protocol is used to find spermatids on the sample and discusses the settings to obtain movies. The protocol uses the mirror shape and astigmatism settings from Appendix F.2 Calibrating the MicAO protocol.

1. Select Time series and make sure that the settings is 'No Delay' and 50000 loops, and the Advanced setting is deselected, as shown in fig G.1.

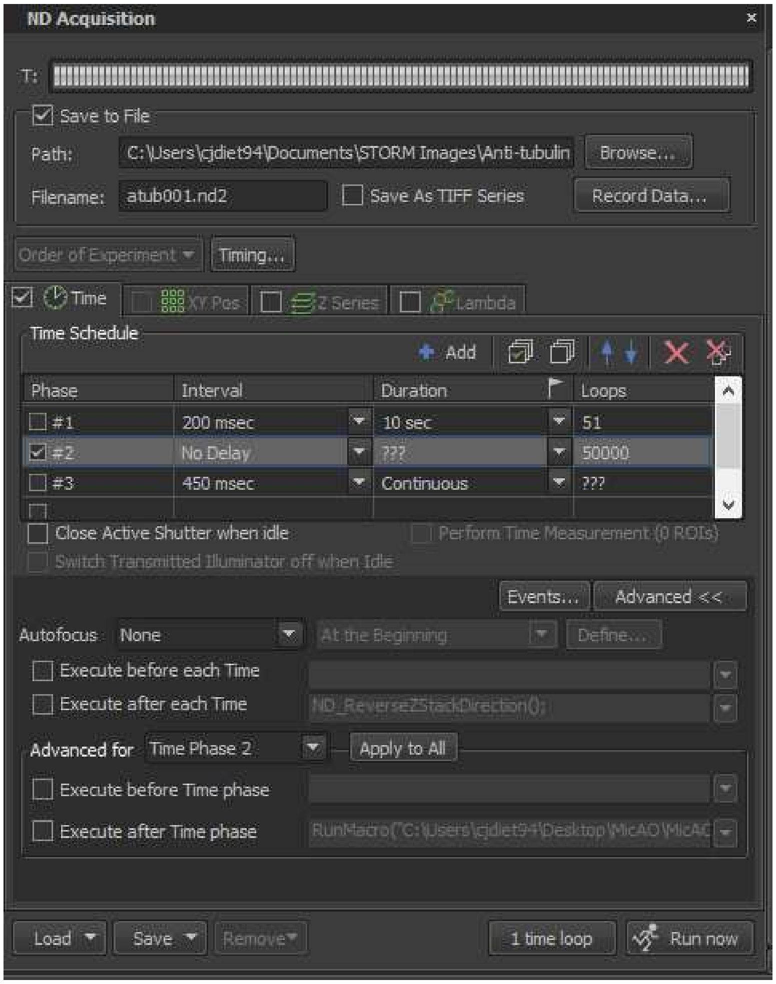

ND Acquisition

☑ Save to File

Path: C:\Users\cjdiet94\Documents\STORM Images\Anti-tubulin

Filename: atub001.nd2

☐ Save As TIFF Series

☑ Time ☐ XY Pos ☐ Z Series ☐ Lambda

Time Schedule

Phase	Interval	Duration	Loops
☐ #1	200 msec	10 sec	51
☑ #2	No Delay	???	50000
☐ #3	450 msec	Continuous	???
☐			

☐ Close Active Shutter when idle

☐ Perform Time Measurement (0 ROIs)

☐ Switch Transmitted Illuminator off when Idle

Autofocus: None

At the Beginning

☐ Execute before each Time

☐ Execute after each Time ND_ReverseZStackDirection();

Advanced for Time Phase 2

☐ Execute before Time phase

☐ Execute after Time phase RunMacro("C:\Users\cjdiet94\Desktop\MicAO\MicAC

Figure G.1: Time series settings for imaging cells

2. Open ASI console. Under MS 2000, select Connect, as shown in fig G.2 a. Click CRISP under ‘More’ options and the dialogue box will open as shown in fig G.2 b.

3. Turn on Violet laser and choose the filter 5 (no light passes through) from Thorlabs FW102C.

4. Set the exposure to 15ms and gain to 10ms. Turn on the bright field.

5. Clean the 100x objective and add fresh oil drop. Place the sample as done for calibration.

6. Locate the surface as explained in the ’Calibrating the MicAO’ protocol.

7. Find a spermatid in stage 10 to 14. Make sure that the cell is on the bottom of the cover slip by checking the focus in and out of the cell. Select ROI of maximum 99px height to reduce the image capture time.

8. Turn off the brightfield and turn on the laser. Adjust the gain to a maximum of 300. Adjust the focusing knobs such that you can see blinking and the fluorophores are focused (plus sign).

9. a) Once the cell is focused, click on Step 1 in ASI CRISP dialogue box, as seen in fig 14b. Turn the silver knob in the Autofocus box and check the LCD display of ASI MFC-2000 to get the largest ‘Sum’ and least negative error. Refer fig G.3. Click Step 2 and then click on Step 3. Click Lock. The focal plane should be the same as you had set.

   b) If it is not, or if the ASI maxes out to +0.5 or -0.5 in z, click Unlock and use the black knob on ASI MFC-2000, as seen in fig 15, to find the focusing plane again. Repeat step 9a.

10. Turn off the red laser. Turn on brightfield and take a picture of the ROI. Name it BFBefore (bright Field Before).

11. Turn off brightfield and put an ND2 filter in the laser path. Turn ON red laser. Take a picture of low fluorescence and name it Fluor.

12. Turn off the laser. Remove the ND2 filter from the path and turn on the laser. Click Run Now.

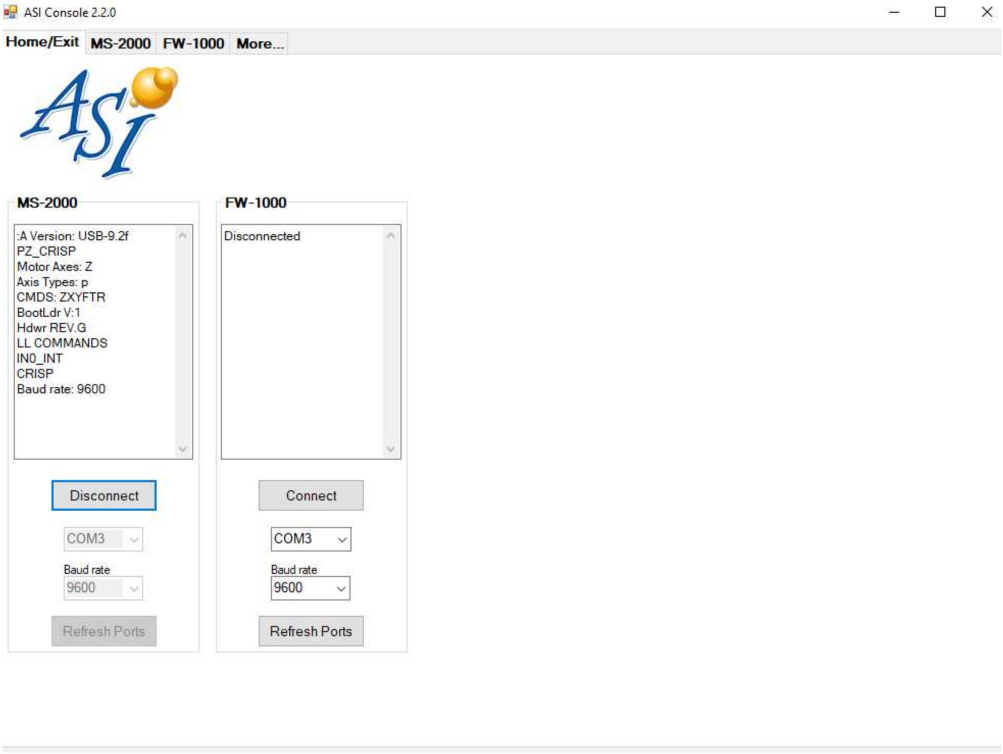

MS-2000

```
:A Version: USB-9.2f
PZ_CRISP
Motor Axes: Z
Axis Types: p
CMDS: ZXYFTR
BootLdr V:1
Hdwr REV.G
LL COMMANDS
IN0_INT
CRISP
Baud rate: 9600
```

COM3
Baud rate 9600

FW-1000

Disconnected

COM3
Baud rate 9600

(a)

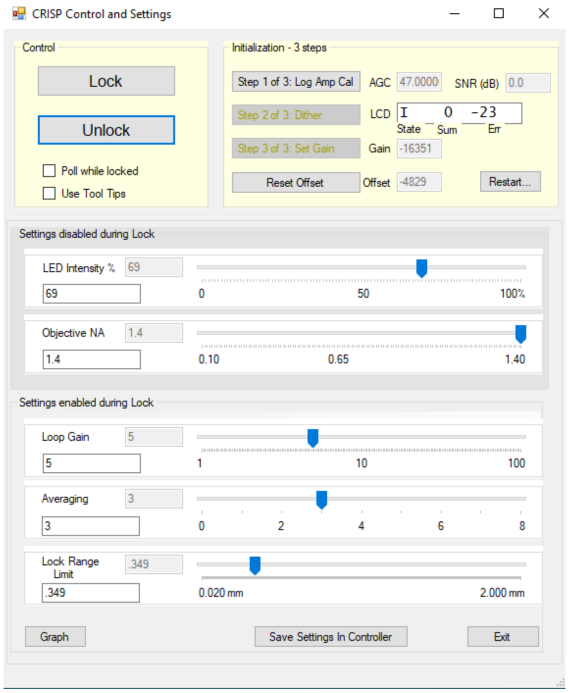

☐ Poll while locked
☐ Use Tool Tips

AGC 47.0000
SNR (dB) 0.0
LCD I 0 -23 (State Sum Err)
Gain -16351
Offset -4829

LED Intensity % 69 (0 – 50 – 100%)
Objective NA 1.4 (0.10 – 0.65 – 1.40)
Loop Gain 5 (1 – 10 – 100)
Averaging 3 (0 – 2 – 4 – 6 – 8)
Lock Range Limit .349 (0.020 mm – 2.000 mm)

(b)

Figure G.2: a) ASI home window (b) CRISP settings to adjust autofocus

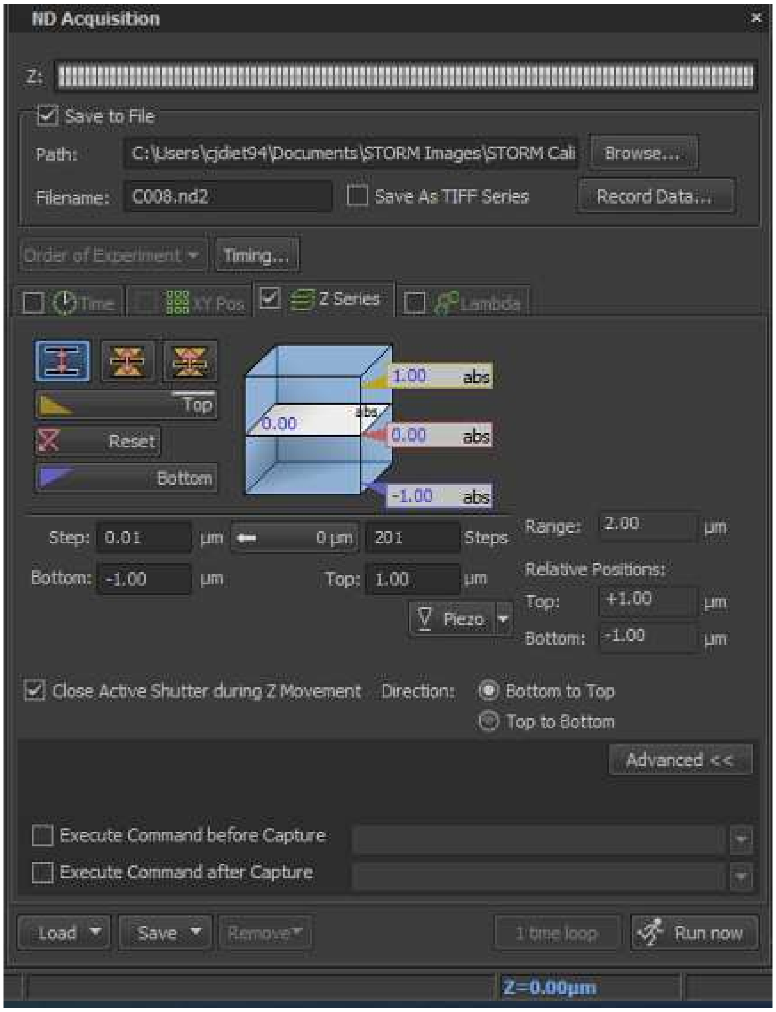

☑ Save to File

Path: C:\Users\cjdiet94\Documents\STORM Images\STORM Cali

Filename: C008.nd2

☐ Save As TIFF Series

☐ Time ☐ XY Pos ☑ Z Series ☐ Lambda

Step: 0.01 µm

201 Steps

Bottom: -1.00 µm

Top: 1.00 µm

Range: 2.00 µm

Relative Positions:

Top: +1.00 µm

Bottom: -1.00 µm

Piezo

☑ Close Active Shutter during Z Movement

Direction: ● Bottom to Top ○ Top to Bottom

☐ Execute Command before Capture

☐ Execute Command after Capture

Z=0.00µm

Figure G.3: ASI MFC 2000

13. Pay close attention to the ASI LCD display to see if it maxes out or is rapidly changing in z. Check the blinking in the live image window. If the rate reduces, change the filter in FW102C to filter4, and if needed increase to filter 3 and then filter 2 later.

14. After the 50000 frames have been collected, turn off the laser. Switch the violet laser filter to filter 5. Reduce the gain to 10. Turn on bright field and take a picture. Name it BFAfter (Bright Field After).

15. Move the slide to an isolated area with no particles on the coverslip and take a picture of the ROI to subtract background noise from BFB. Unlock the Autofocus.

16. Repeat steps 7 to 15 until its 2 hours after the imaging buffer was added to the sample.

17. Prepare a new sample and repeat steps 4 to 16.

Appendix H

Obtaining look up tables for Astigmatism method

This protocol makes use of ImageJ software to obtain the look up tables from the calibration movies obtained. ImageJ produces .yaml files based on the settings selected for reconstruction. The .yaml file that gives the best sigma curve is selected as the look up table to run the 3D reconstruction of spermatid movies.

1. Install NDi6 plug-in for ImageJ.
2. Select Plugins>NDi6>ND to Image6D and choose the ND2 file from the path.
3. Export the 201 frames (.tiff) to the desired path. Refer to fig H.1
4. Click File>Import>Image sequence
5. Select frames 30 to 170 and drag and drop them to the drop-down window as seen in fig H.2.
6. Check the ‘Visual stack’ box. Select Plugins> ThunderSTORM> 3Dcalibration> Cylindrical lens calibration, as shown in fig H.3.
7. From the new window, select Camera set up. Refer fig H.4. For the TIRF set up in Krapf lab, the Pixel size in nm is 130, Photoelectrons per A/D count is 16.23773, Base level A/D counts is 6.437. Type in the EM Gain for the calibration movie. Click on OK
8. For the rest of the settings, refer fig H.5. Click on Image Filtering, select Wavelet filter with B-spline order 3 and scale 2.0 from the drop-down menu.
9. Select ‘Local maximum’ as Method under Approximate localization of molecules and connectivity as 8-neighbourhood.
10. Select ‘Elliptic Gaussian w/angle’ under sub-pixel localization of molecules

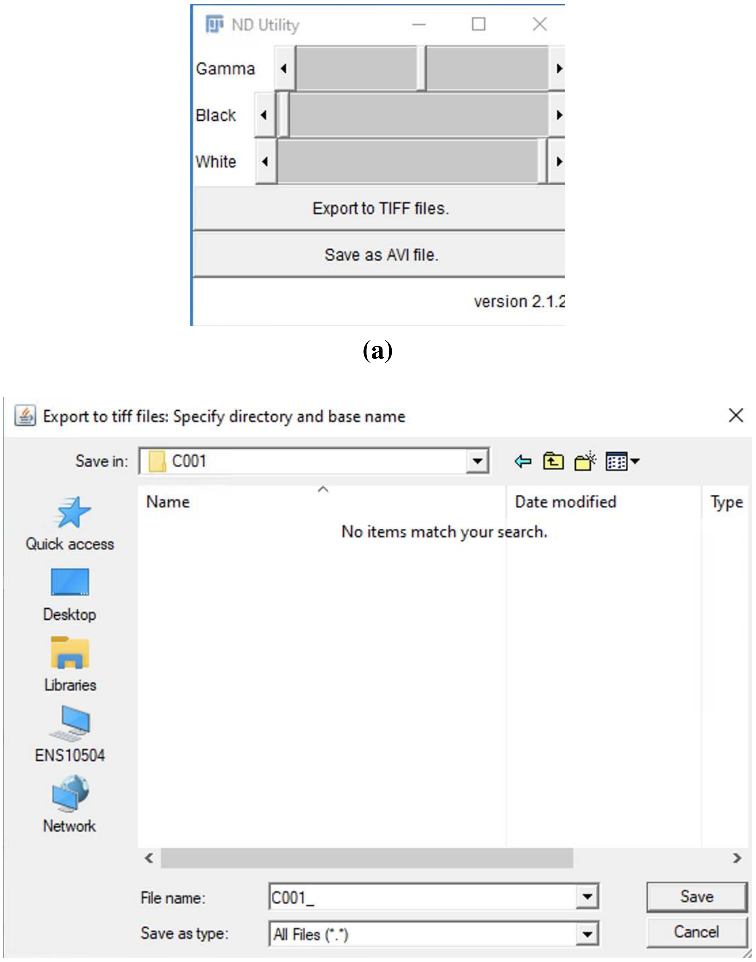

Save in: C001

No items match your search.

File name: C001_

Save as type: All Files (*.*)

(a)

(b)

Figure H.1: (a)Exporting to .tiff files. (b) Path to which files were exported

11. Choose Fitting radius[px] as 6, Fitting method as Least squares and Initial sigma[px] as 0.93. Choose 3D defocusing curve as ThunderSTORM.

12. Enter z stage step[nm] as 10 and z stage limit[nm] as 550.

13. Enter Peak intensity threshold as 1*std(Wave.F1) and click on Preview.

14. Check the beads in the preview and see if each of them has a single plus sign at its center. If there are plus signs in the background where beads are not present, as seen in fig H.6 a), increase the threshold value to 1.5, 2 and so on until only the beads are located with plus signs, as shown in fig H.6 b).

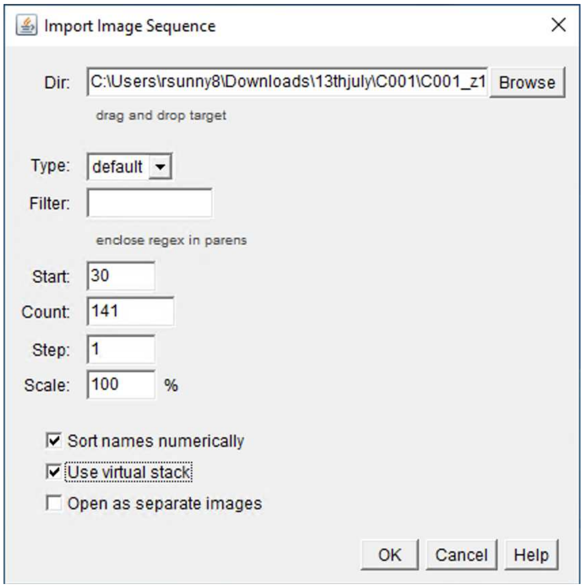

Import Image Sequence

Dir: C:\Users\rsunny8\Downloads\13thjuly\C001\C001_z1

drag and drop target

Type: default

Filter:

enclose regex in parens

Start: 30

Count: 141

Step: 1

Scale: 100 %

☑ Sort names numerically

☑ Use virtual stack

☐ Open as separate images

Figure H.2: Importing tiff files for calibration

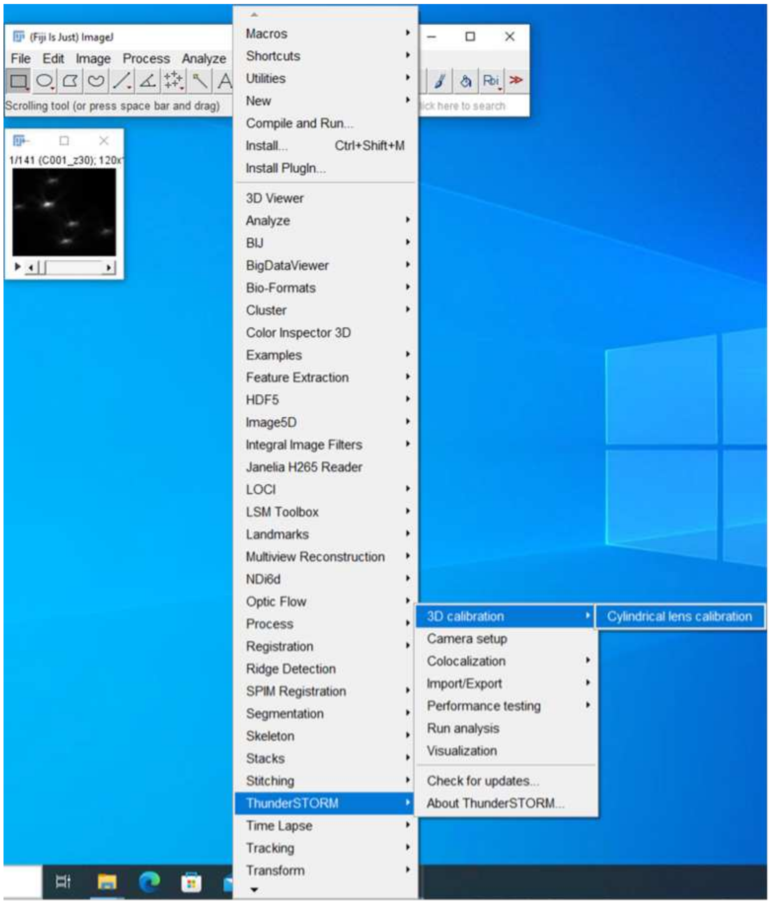

Figure H.3: Navigating to cylindrical lens calibration

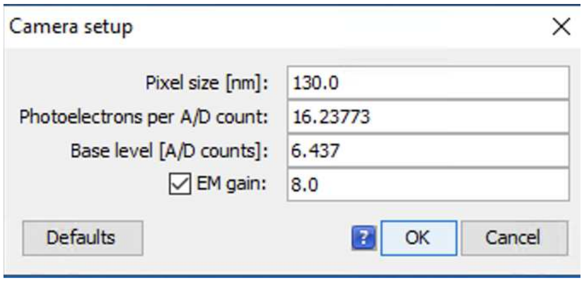

Pixel size [nm]: 130.0
Photoelectrons per A/D count: 16.23773
Base level [A/D counts]: 6.437
☑ EM gain: 8.0

Figure H.4: Camera settings for calibration

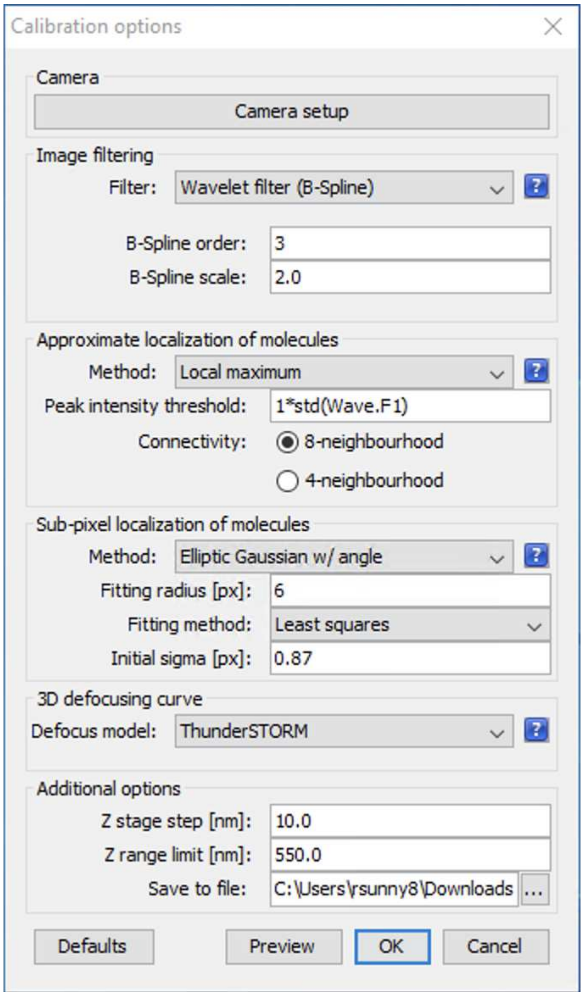

Filter: Wavelet filter (B-Spline)
B-Spline order: 3
B-Spline scale: 2.0
Method: Local maximum
Peak intensity threshold: 1*std(Wave.F1)
Connectivity: ● 8-neighbourhood ○ 4-neighbourhood
Method: Elliptic Gaussian w/ angle
Fitting radius [px]: 6
Fitting method: Least squares
Initial sigma [px]: 0.87
Defocus model: ThunderSTORM
Z stage step [nm]: 10.0
Z range limit [nm]: 550.0
Save to file: C:\Users\rsunny8\Downloads

Figure H.5: Settings to run 3D calibration

15. Choose ‘Save to file’ and choose the path to save yaml file, as shown in fig H.7.

16. Press OK to run the calibration.

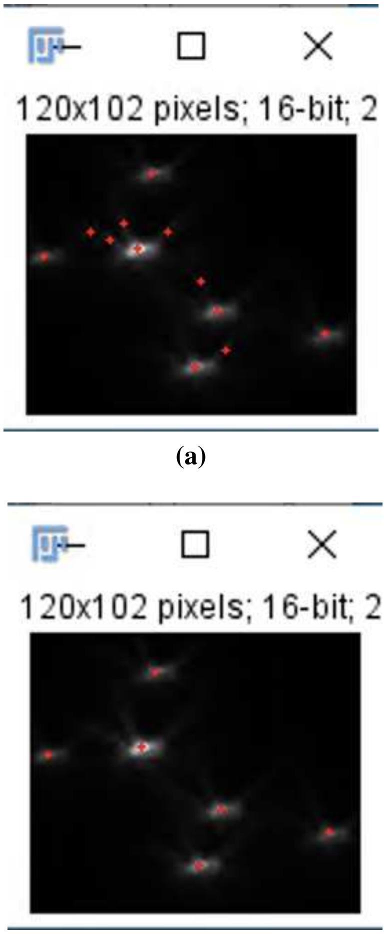

(a)

(b)

Figure H.6: Calibration preview (a) Calibration preview before adjusting the threshold (b) Calibration preview after adjusting peak intensity threshold

17. Observe the Sigma curves and save them. Repeat the steps for all calibration movies. Choose the one with the most symmetric sigma curves and is most centered at z. Refer fig H.8.

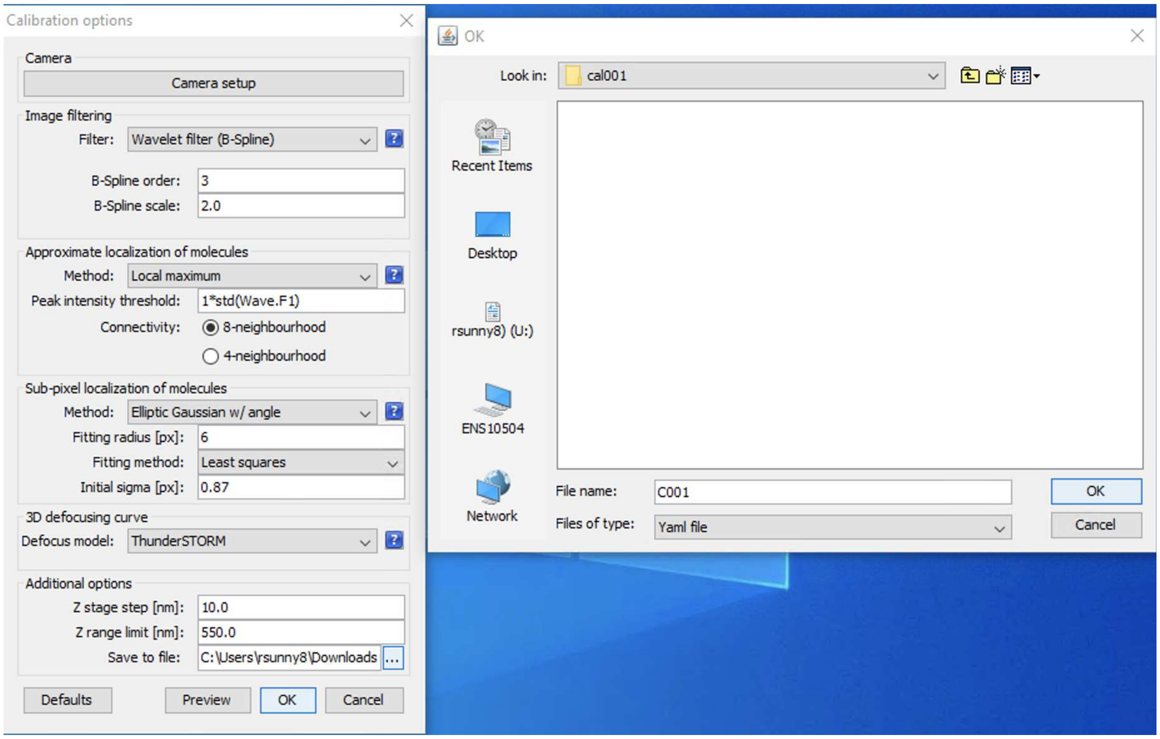

Image filtering

Filter: Wavelet filter (B-Spline)

B-Spline order: 3

B-Spline scale: 2.0

Approximate localization of molecules

Method: Local maximum

Peak intensity threshold: 1*std(Wave.F1)

Connectivity: ● 8-neighbourhood ○ 4-neighbourhood

Sub-pixel localization of molecules

Method: Elliptic Gaussian w/ angle

Fitting radius [px]: 6

Fitting method: Least squares

Initial sigma [px]: 0.87

3D defocusing curve

Defocus model: ThunderSTORM

Additional options

Z stage step [nm]: 10.0

Z range limit [nm]: 550.0

Save to file: C:\Users\rsunny8\Downloads

Look in: cal001

File name: C001

Files of type: Yaml file

Figure H.7: Path to save .yaml file

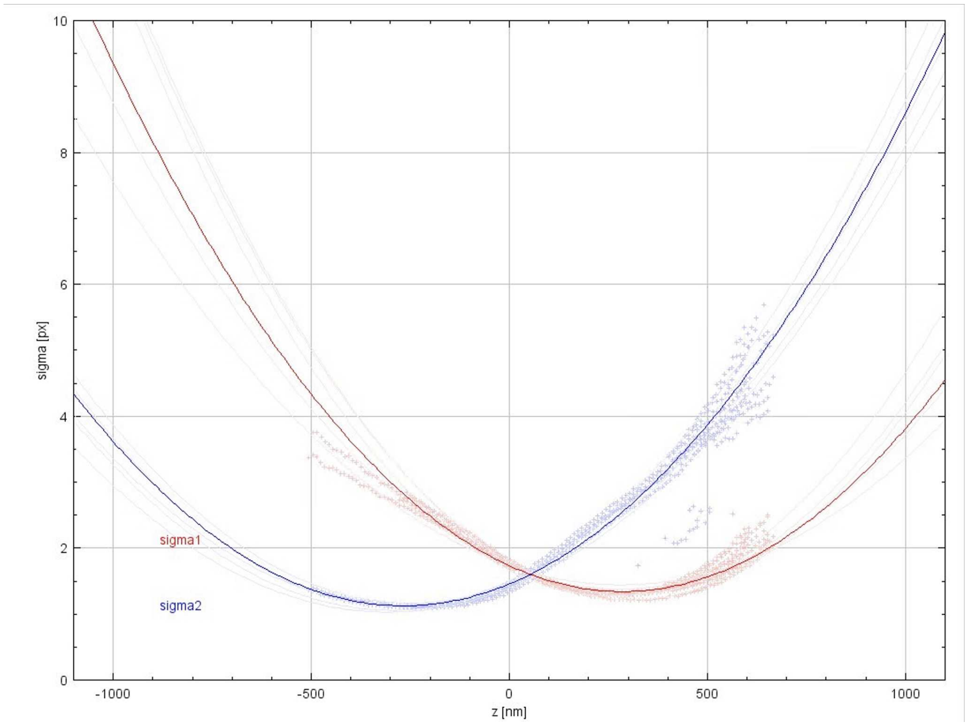

Figure H.8: Sigma curve

Appendix I

STORM 3D Reconstruction Protocol

The protocol uses ImageJ software, and discusses the steps to obtain 3D reconstruction from the spermatid movies collected according to the protocol in Appendix G- Finding and imaging spermatid. The LUT from Appendix H- Obtaining look up tables for Astigmatism method, is used in this protocol.

1. Drag and drop the .nd2 file to ImageJ toolbar. Click OK on the window opened as shown in fig I.1.

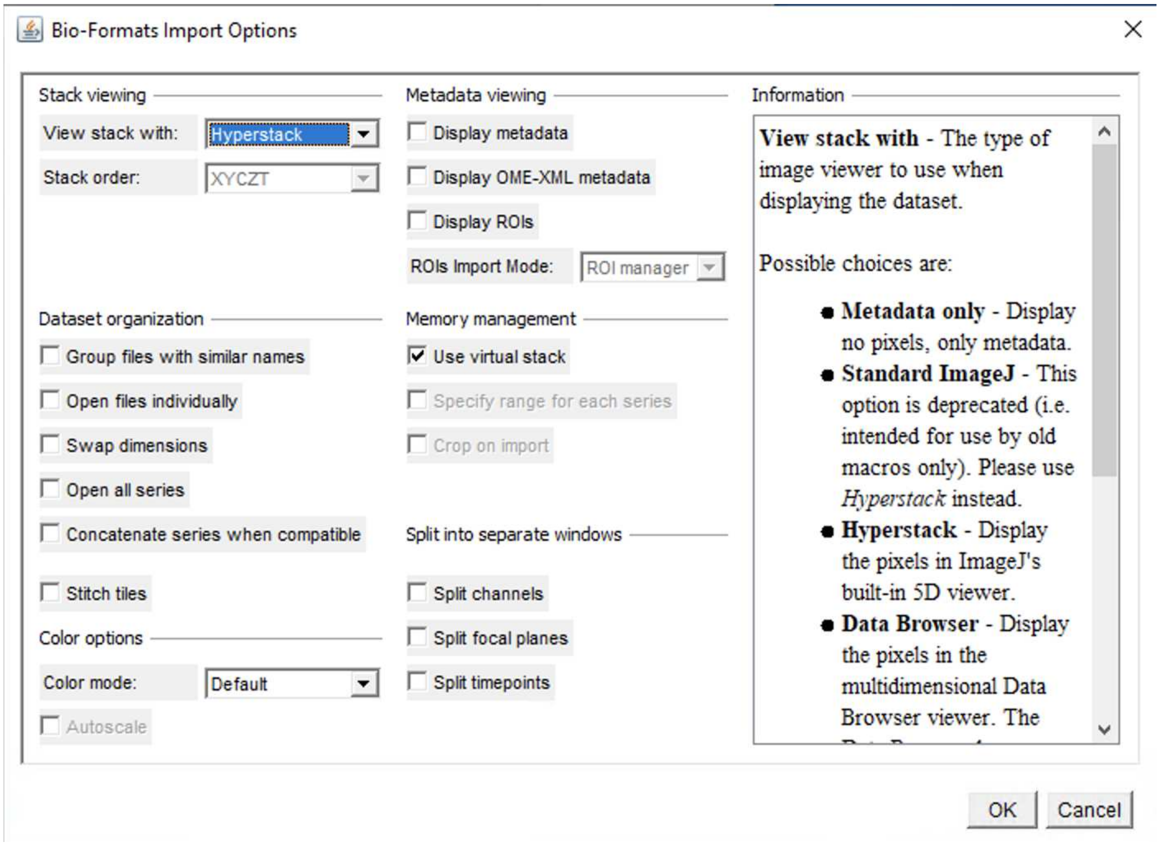

Bio-Formats Import Options

Stack viewing
View stack with: Hyperstack
Stack order: XYCZT

Dataset organization
☐ Group files with similar names
☐ Open files individually
☐ Swap dimensions
☐ Open all series
☐ Concatenate series when compatible
☐ Stitch tiles

Color options
Color mode: Default
☐ Autoscale

Metadata viewing
☐ Display metadata
☐ Display OME-XML metadata
☐ Display ROIs
ROIs Import Mode: ROI manager

Memory management
☑ Use virtual stack
☐ Specify range for each series
☐ Crop on import

Split into separate windows
☐ Split channels
☐ Split focal planes
☐ Split timepoints

Information

View stack with - The type of image viewer to use when displaying the dataset.

Possible choices are:

- **Metadata only** - Display no pixels, only metadata.
- **Standard ImageJ** - This option is deprecated (i.e. intended for use by old macros only). Please use *Hyperstack* instead.
- **Hyperstack** - Display the pixels in ImageJ's built-in 5D viewer.
- **Data Browser** - Display the pixels in the multidimensional Data Browser viewer. The

Figure I.1: Importing data to ThunderSTORM

2. Select Plugins>ThunderSTORM> Run analysis as shown in fig I.2.

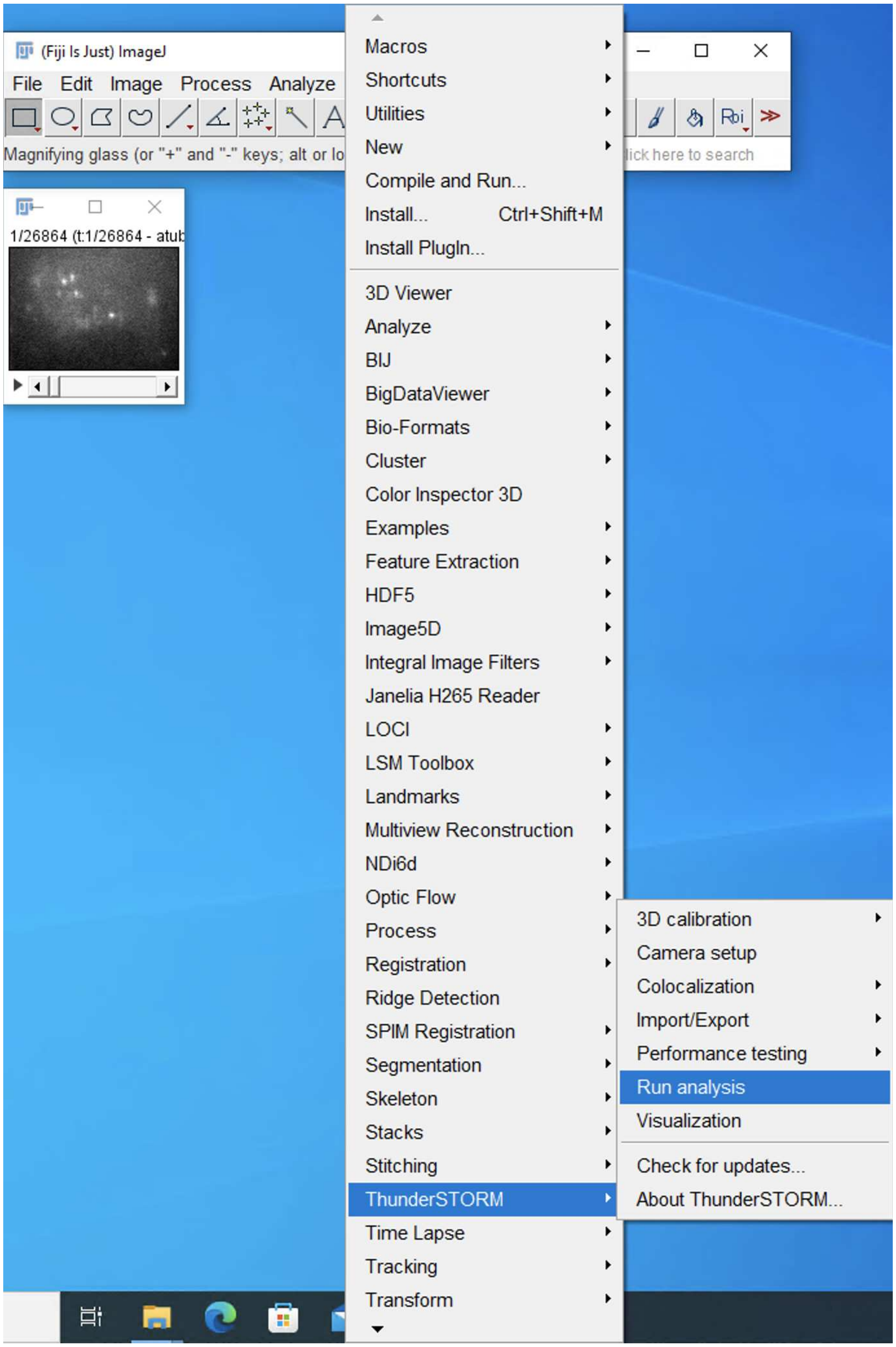

Figure I.2: Path to Run analysis

3. Set the parameters in camera set up as shown in fig I.3, and type in the gain you had recorded while imaging.

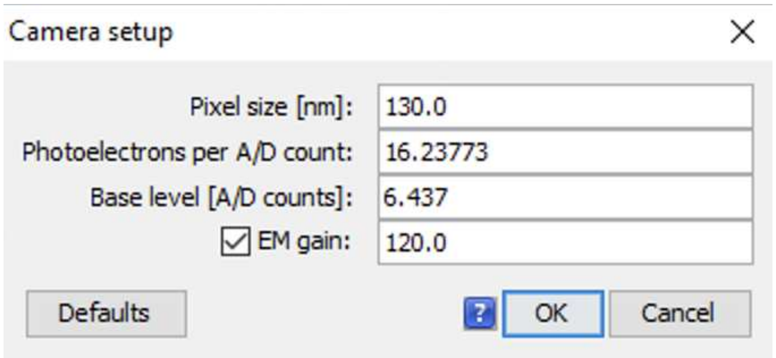

Pixel size [nm]: 130.0
Photoelectrons per A/D count: 16.23773
Base level [A/D counts]: 6.437
☑ EM gain: 120.0

Figure I.3: Camera setup for reconstruction

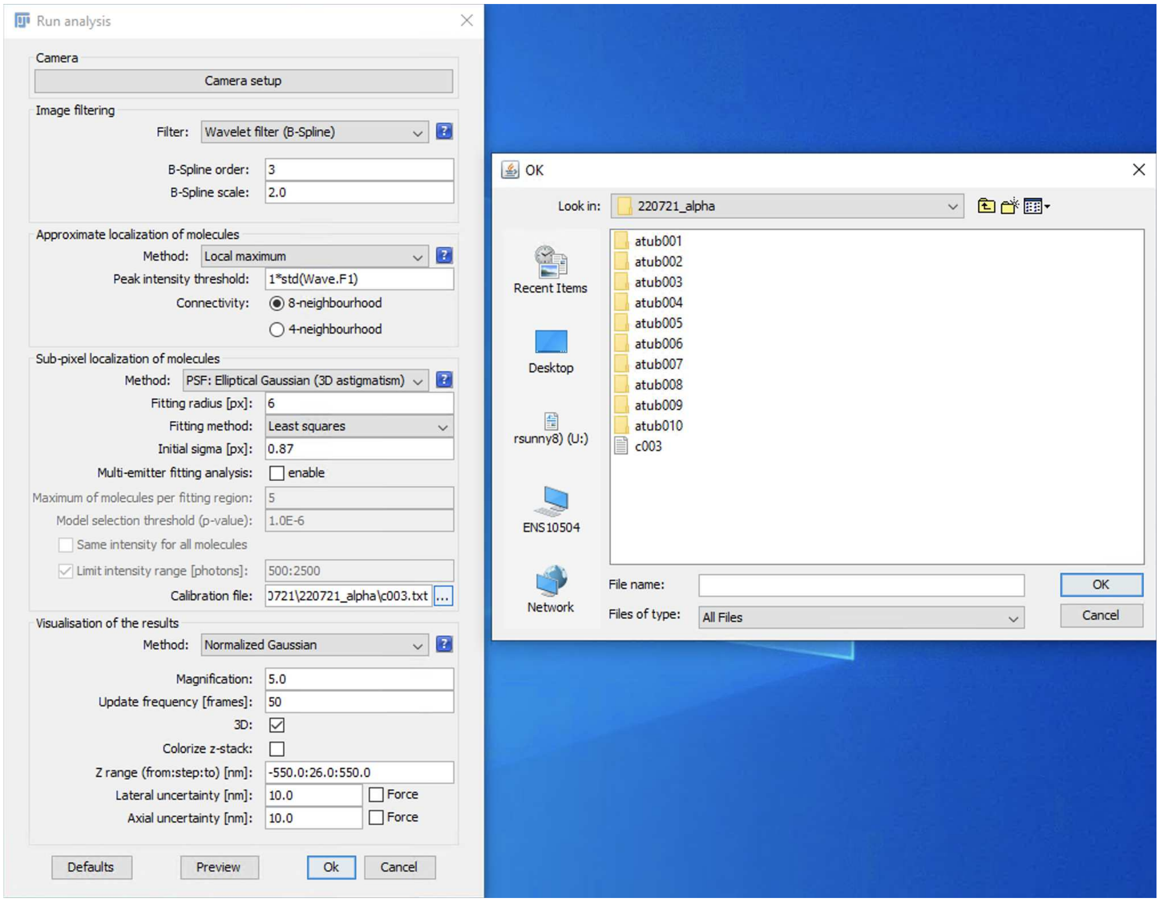

Filter: Wavelet filter (B-Spline)
B-Spline order: 3
B-Spline scale: 2.0
Method: Local maximum
Peak intensity threshold: 1*std(Wave.F1)
Connectivity: ● 8-neighbourhood ○ 4-neighbourhood
Method: PSF: Elliptical Gaussian (3D astigmatism)
Fitting radius [px]: 6
Fitting method: Least squares
Initial sigma [px]: 0.87
Multi-emitter fitting analysis: ☐ enable
Maximum of molecules per fitting region: 5
Model selection threshold (p-value): 1.0E-6
☐ Same intensity for all molecules
☑ Limit intensity range [photons]: 500:2500
Calibration file: 721\220721_alpha\c003.txt
Method: Normalized Gaussian
Magnification: 5.0
Update frequency [frames]: 50
3D: ☑
Colorize z-stack: ☐
Z range (from:step:to) [nm]: -550.0:26.0:550.0
Lateral uncertainty [nm]: 10.0 ☐ Force
Axial uncertainty [nm]: 10.0 ☐ Force

Look in: 220721_alpha

atub001
atub002
atub003
atub004
atub005
atub006
atub007
atub008
atub009
atub010
c003

File name:
Files of type: All Files

Figure I.4: General settings for 3 D reconstruction

4. Refer fig I.4 for the Run Analysis settings. Choose Wavelet filter (β spline) as imaging filter with order 3 and scale 2. Approximate localization of molecules: Select method as local minimum. The peak intensity threshold can be any value from 1. Use 'preview ' to choose the best value or set it as 1. The connectivity is 8-neighbourhood.

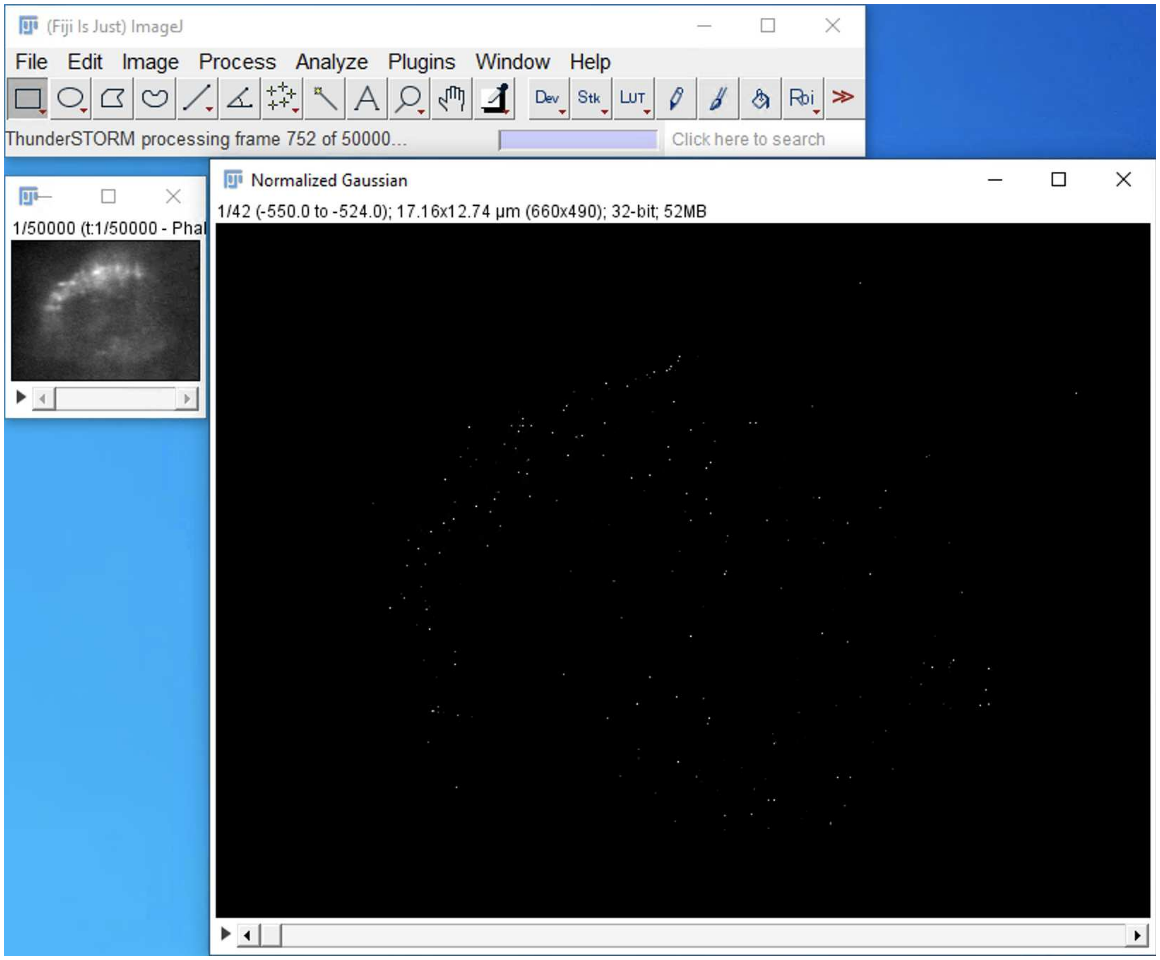

ThunderSTORM processing frame 752 of 50000...

1/50000 (t:1/50000 - Phal

1/42 (-550.0 to -524.0); 17.16x12.74 µm (660x490); 32-bit; 52MB

Figure I.5: Normalized Gaussian

5. Sub pixel localization of molecules: Since we are running 3D localization with astigmatism method, choose Elliptical Gaussian:3D astigmatism as the method, with fitting radius 3 and initial sigma 0.87. The initial sigma value depends on the emission wavelength of fluorophores, numerical aperture of the objective, pixel size of the system such that , Initial Sigma[px]= 0.25*$\lambda_{emission}$/(NA*pixel size). Since Alexa 647 has an emission wavelength of 671 nm, numerical aperture of the objective is 1.49 and pixel size is 130, initial sigma is 0.87 nm. Select the calibration file (.yaml or .txt) that gave the best sigma curve as discussed in Calibration protocol.

6. Visualization of the results: Choose Normalized Gaussian as the method with a magnification of 5 and update frequency (frames) as 50. Deselect Colorize z stack to reduce the time of

processing. The z range is chosen as -550 to 550. The step size is pixel size/ magnification, and hence is 130/5 = 26. Set axial and lateral uncertainty in nm as 10.

7. Click OK to run analysis. Normalized Gaussian window will open as seen in fig I.5, and the 50000 frames will be processed.

8. After the initial reconstruction , a table will be displayed as seen in fig I.6. Export this table. It can be imported any time by going to Plugins>ThunderSTORM>Import/Export>Import results.

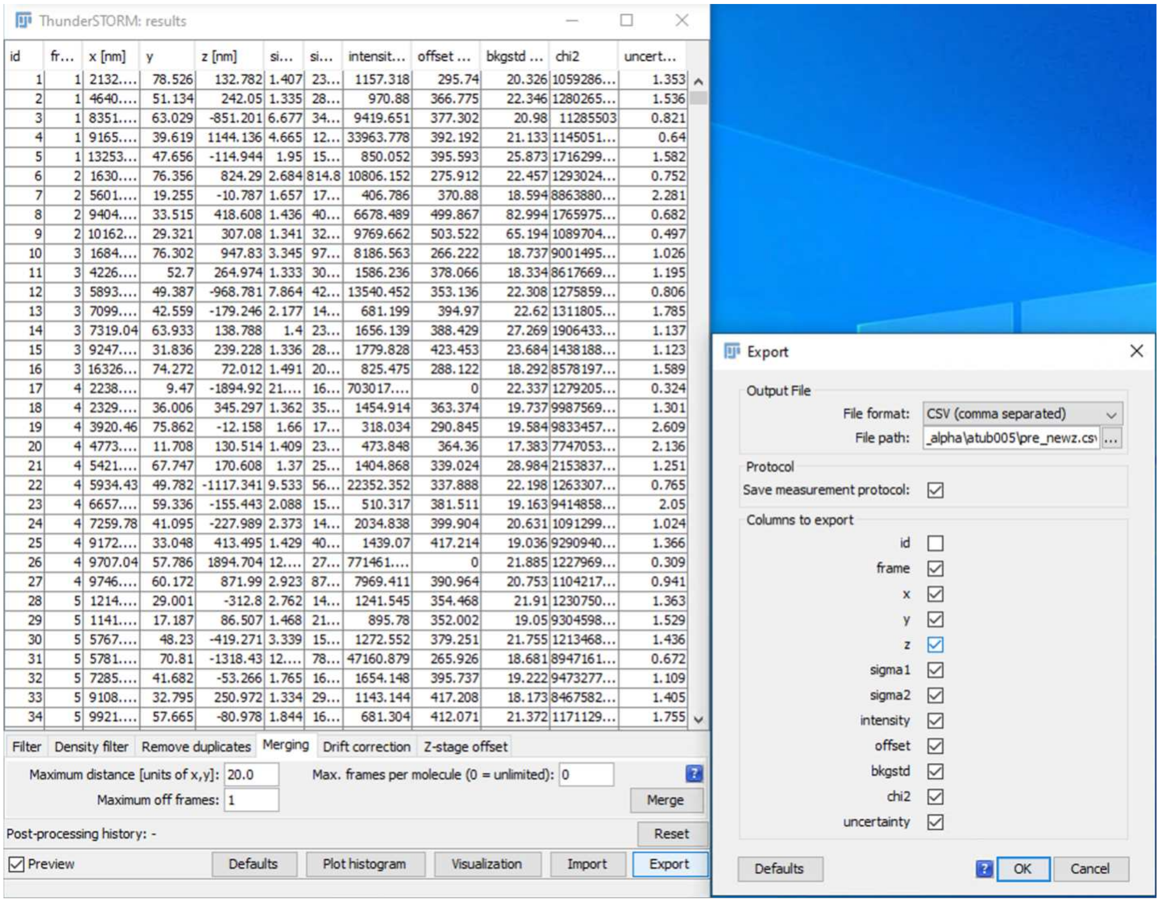

id	fr...	x [nm]	y	z [nm]	si...	si...	intensit...	offset ...	bkgstd ...	chi2	uncert...
1	1	2132....	78.526	132.782	1.407	23...	1157.318	295.74	20.326	1059286...	1.353
2	1	4640....	51.134	242.05	1.335	28...	970.88	366.775	22.346	1280265...	1.536
3	1	8351....	63.029	-851.201	6.677	34...	9419.651	377.302	20.98	11285503	0.821
4	1	9165....	39.619	1144.136	4.665	12...	33963.778	392.192	21.133	1145051...	0.64
5	1	13253...	47.656	-114.944	1.95	15...	850.052	395.593	25.873	1716299...	1.582
6	2	1630....	76.356	824.29	2.684	814.8	10806.152	275.912	22.457	1293024...	0.752
7	2	5601....	19.255	-10.787	1.657	17...	406.786	370.88	18.594	8863880...	2.281
8	2	9404....	33.515	418.608	1.436	40...	6678.489	499.867	82.994	1765975...	0.682
9	2	10162...	29.321	307.08	1.341	32...	9769.662	503.522	65.194	1089704...	0.497
10	3	1684....	76.302	947.83	3.345	97...	8186.563	266.222	18.737	9001495...	1.026
11	3	4226....	52.7	264.974	1.333	30...	1586.236	378.066	18.334	8617669...	1.195
12	3	5893....	49.387	-968.781	7.864	42...	13540.452	353.136	22.308	1275859...	0.806
13	3	7099....	42.559	-179.246	2.177	14...	681.199	394.97	22.62	1311805...	1.785
14	3	7319.04	63.933	138.788	1.4	23...	1656.139	388.429	27.269	1906433...	1.137
15	3	9247....	31.836	239.228	1.336	28...	1779.828	423.453	23.684	1438188...	1.123
16	3	16326...	74.272	72.012	1.491	20...	825.475	288.122	18.292	8578197...	1.589
17	4	2238....	9.47	-1894.92	21....	16...	703017....	0	22.337	1279205...	0.324
18	4	2329....	36.006	345.297	1.362	35...	1454.914	363.374	19.737	9987569...	1.301
19	4	3920.46	75.862	-12.158	1.66	17...	318.034	290.845	19.584	9833457...	2.609
20	4	4773....	11.708	130.514	1.409	23...	473.848	364.36	17.383	7747053...	2.136
21	4	5421....	67.747	170.608	1.37	25...	1404.868	339.024	28.984	2153837...	1.251
22	4	5934.43	49.782	-1117.341	9.533	56...	22352.352	337.888	22.198	1263307...	0.765
23	4	6657....	59.336	-155.443	2.088	15...	510.317	381.511	19.163	9414858...	2.05
24	4	7259.78	41.095	-227.989	2.373	14...	2034.838	399.904	20.631	1091299...	1.024
25	4	9172....	33.048	413.495	1.429	40...	1439.07	417.214	19.036	9290940...	1.366
26	4	9707.04	57.786	1894.704	12....	27...	771461....	0	21.885	1227969...	0.309
27	4	9746....	60.172	871.99	2.923	87...	7969.411	390.964	20.753	1104217...	0.941
28	5	1214....	29.001	-312.8	2.762	14...	1241.545	354.468	21.91	1230750...	1.363
29	5	1141....	17.187	86.507	1.468	21...	895.78	352.002	19.05	9304598...	1.529
30	5	5767....	48.23	-419.271	3.339	15...	1272.552	379.251	21.755	1213468...	1.436
31	5	5781....	70.81	-1318.43	12....	78...	47160.879	265.926	18.681	8947161...	0.672
32	5	7285....	41.682	-53.266	1.765	16...	1654.148	395.737	19.222	9473277...	1.109
33	5	9108....	32.795	250.972	1.334	29...	1143.144	417.208	18.173	8467582...	1.405
34	5	9921....	57.665	-80.978	1.844	16...	681.304	412.071	21.372	1171129...	1.755

Maximum distance [units of x,y]: 20.0
Max. frames per molecule (0 = unlimited): 0
Maximum off frames: 1

Post-processing history: -

☑ Preview

Output File
File format: CSV (comma separated)
File path: _alpha\atub005\pre_newz.cs

Protocol
Save measurement protocol: ☑

Columns to export
id ☐
frame ☑
x ☑
y ☑
z ☑
sigma1 ☑
sigma2 ☑
intensity ☑
offset ☑
bkgstd ☑
chi2 ☑
uncertainty ☑

Figure I.6: Preprocessing Look-up-table

9. First step in postprocessing is to remove duplicates. Click on Apply as seen in fig I.7. The Post processing history section will show when that step is finished.

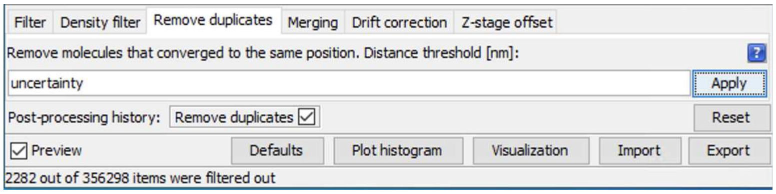

Remove molecules that converged to the same position. Distance threshold [nm]:

uncertainty

Post-processing history: Remove duplicates ☑

☑ Preview

2282 out of 356298 items were filtered out

Figure I.7: Removing duplicates from the initial reconstruction data

10. The second step is to filter out the range outside the calibration accuracy range of -550 to 550. To do this, click on Plot Histogram and choose z as the parameter, as shown in fig I.8.

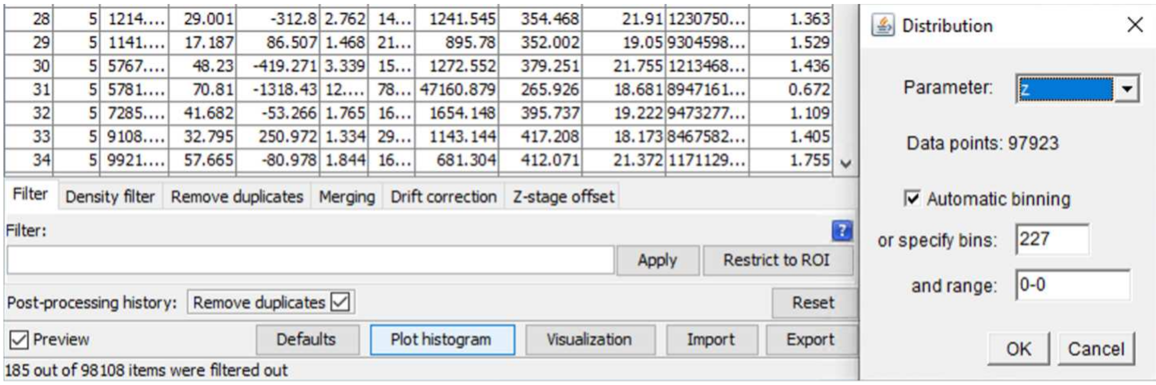

28	5	1214....	29.001	-312.8	2.762	14...	1241.545	354.468	21.91	1230750...	1.363
29	5	1141....	17.187	86.507	1.468	21...	895.78	352.002	19.05	9304598...	1.529
30	5	5767....	48.23	-419.271	3.339	15...	1272.552	379.251	21.755	1213468...	1.436
31	5	5781....	70.81	-1318.43	12....	78...	47160.879	265.926	18.681	8947161...	0.672
32	5	7285....	41.682	-53.266	1.765	16...	1654.148	395.737	19.222	9473277...	1.109
33	5	9108....	32.795	250.972	1.334	29...	1143.144	417.208	18.173	8467582...	1.405
34	5	9921....	57.665	-80.978	1.844	16...	681.304	412.071	21.372	1171129...	1.755

Filter:

Post-processing history: Remove duplicates ☑

☑ Preview

185 out of 98108 items were filtered out

Parameter: z

Data points: 97923

☑ Automatic binning

or specify bins: 227

and range: 0-0

Figure I.8: Plot histogram of reconstructed data

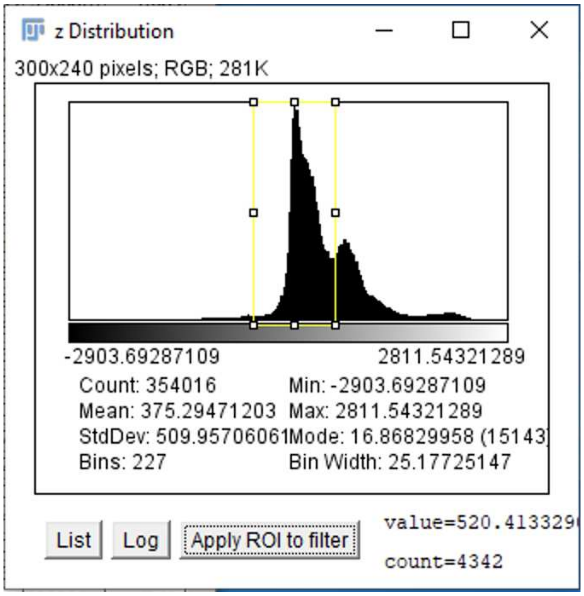

300x240 pixels; RGB; 281K

Count: 354016
Min: -2903.69287109
Mean: 375.29471203
Max: 2811.54321289
StdDev: 509.95706061
Mode: 16.86829958 (15143
Bins: 227
Bin Width: 25.17725147

value=520.413329

count=4342

Figure I.9: z distribution of the reconstructed data

11. A window will pop up as seen in fig I.9. Select the region with the highest peak and utilize up to 550 on either side of the peak. Click on ‘Apply ROI to filter’

12. The z range will be reflected in the Filter section. Click on Apply and the Restrict to ROI. The post-processing history section will reflect the changes as shown in fig I.10.

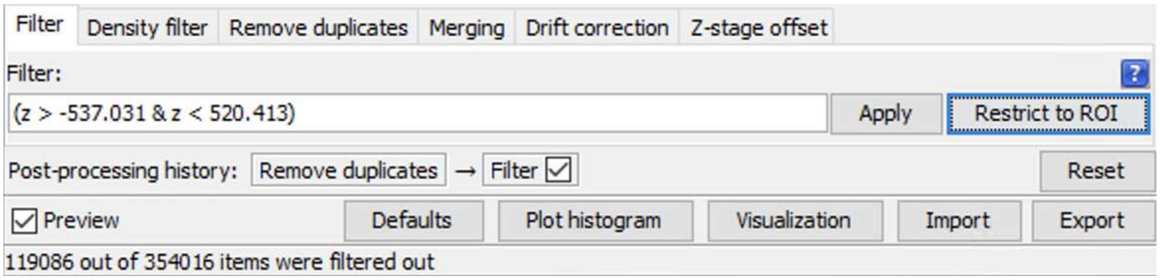

Filter: (z > -537.031 & z < 520.413)

Post-processing history: Remove duplicates → Filter ☑

☑ Preview

119086 out of 354016 items were filtered out

Figure I.10: Coarse z filtering

13. Click on visualization to view the stacks of reconstruction in each z height. Select Auto size by results to visualize Normalized Gaussian of truncated data. Click on ’Auto size by analysis’ to view the Normalized Gaussian with the same pixel width and height as the .nd2 movie. Select colorized z stack. Refer fig I.11.

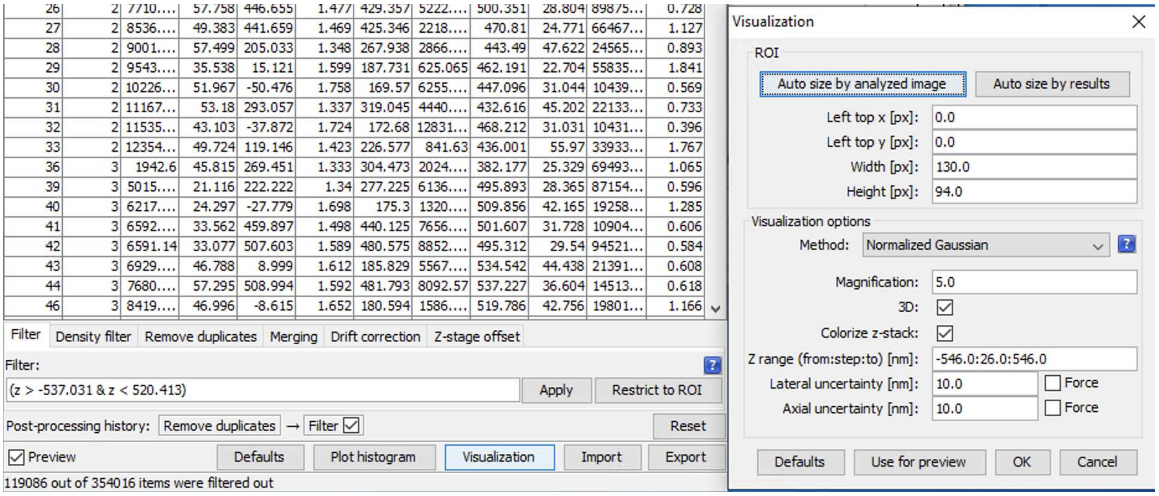

26	2	7710....	57.758	446.655	1.477	429.357	5222....	500.351	28.804	89875...	0.728
27	2	8536....	49.383	441.659	1.469	425.346	2218....	470.81	24.771	66467...	1.127
28	2	9001....	57.499	205.033	1.348	267.938	2866....	443.49	47.622	24565...	0.893
29	2	9543....	35.538	15.121	1.599	187.731	625.065	462.191	22.704	55835...	1.841
30	2	10226...	51.967	-50.476	1.758	169.57	6255....	447.096	31.044	10439...	0.569
31	2	11167...	53.18	293.057	1.337	319.045	4440....	432.616	45.202	22133...	0.733
32	2	11535...	43.103	-37.872	1.724	172.68	12831...	468.212	31.031	10431...	0.396
33	2	12354...	49.724	119.146	1.423	226.577	841.63	436.001	55.97	33933...	1.767
36	3	1942.6	45.815	269.451	1.333	304.473	2024....	382.177	25.329	69493...	1.065
39	3	5015....	21.116	222.222	1.34	277.225	6136....	495.893	28.365	87154...	0.596
40	3	6217....	24.297	-27.779	1.698	175.3	1320....	509.856	42.165	19258...	1.285
41	3	6592....	33.562	459.897	1.498	440.125	7656....	501.607	31.728	10904...	0.606
42	3	6591.14	33.077	507.603	1.589	480.575	8852....	495.312	29.54	94521...	0.584
43	3	6929....	46.788	8.999	1.612	185.829	5567....	534.542	44.438	21391...	0.608
44	3	7680....	57.295	508.994	1.592	481.793	8092.57	537.227	36.604	14513...	0.618
46	3	8419....	46.996	-8.615	1.652	180.594	1586....	519.786	42.756	19801...	1.166

Filter: (z > -537.031 & z < 520.413)

Post-processing history: Remove duplicates → Filter ☑

☑ Preview

119086 out of 354016 items were filtered out

Left top x [px]: 0.0
Left top y [px]: 0.0
Width [px]: 130.0
Height [px]: 94.0
Method: Normalized Gaussian
Magnification: 5.0
3D: ☑
Colorize z-stack: ☑
Z range (from:step:to) [nm]: -546.0:26.0:546.0
Lateral uncertainty [nm]: 10.0 ☐ Force
Axial uncertainty [nm]: 10.0 ☐ Force

Figure I.11: Visualization of filtered data with stacks in different z height

14. The next step is drift correction. Since there are no beads used in imaging the spermatids, choose Cross correlation method. On clicking » a window will open as seen in fig I.12 a. Choose number of bins as 5 and keep the magnification at 5. Observe the x and y drifts. If they are not monotonously increasing or decreasing, as seen in fig I.12 a, reduce the number of bins to 4, 3 and so on until they are, as seen in figure I.12 b.

15. Apply Density filter to the data to reduce the background noise. Choose the distance radius in nm as 25.0 and the maximum number of neighbors in the radius as 2. Refer fig I.13. These values may be adjusted after previewing the reconstructed data to obtain least noise.

16. The last step is to merge the data. Click on the Merging tab and select Merge, as shown in fig I.14.

17. Export the post processed data to the desired folder for future reference. Refer fig I.15.

18. Click on Visualization and choose Auto size by analysis. Save the Normalized Gaussian stack of images as .tiff file, as shown in fig I.16. Click on Image>Type>RGB.

19. Select Image>Stack>z project to see the z projection or select Image>Stack>3D projection to see the rotation movie. Refer fig I.17 for the 3D projection settings.

20. Add scale to the z projection or 3D projection by selecting Analyze> Set scale and then choosing Analyze>Tools> Scale bar. Refer to fig I.18a and I.18b.

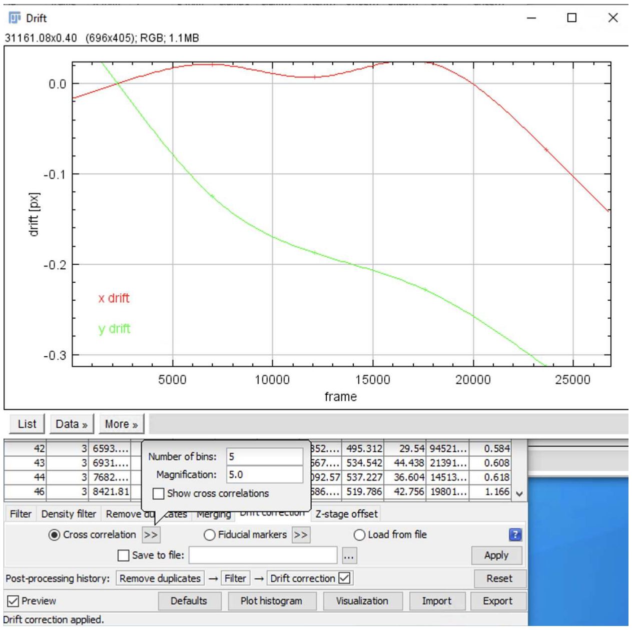

31161.08x0.40 (696x405); RGB; 1.1MB

42	3	6593....	52....	495.312	29.54	94521...	0.584
43	3	6931....	67....	534.542	44.438	21391...	0.608
44	3	7682....	92.57	537.227	36.604	14513...	0.618
46	3	8421.81	86....	519.786	42.756	19801...	1.166

Number of bins: 5
Magnification: 5.0
☐ Show cross correlations

● Cross correlation ○ Fiducial markers ○ Load from file
☐ Save to file:
Post-processing history: Remove duplicates → Filter → Drift correction ☑
☑ Preview
Drift correction applied.

(a)

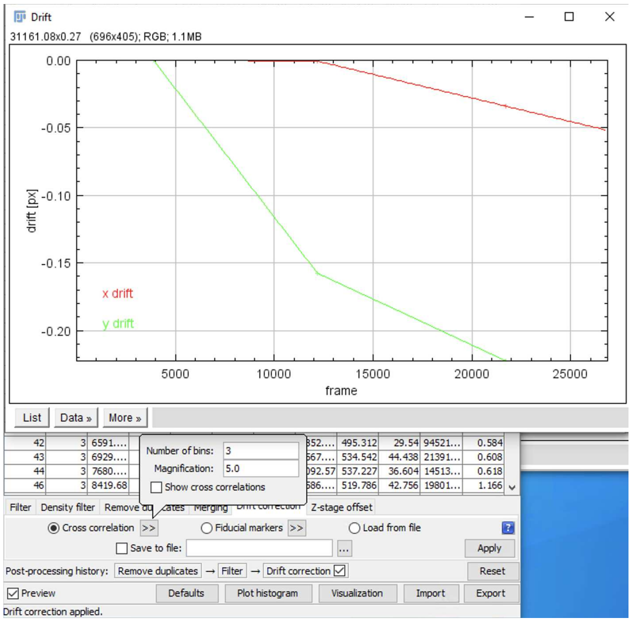

31161.08x0.27 (696x405); RGB; 1.1MB

42	3	6591....	52....	495.312	29.54	94521...	0.584
43	3	6929....	67....	534.542	44.438	21391...	0.608
44	3	7680....	92.57	537.227	36.604	14513...	0.618
46	3	8419.68	86....	519.786	42.756	19801...	1.166

Number of bins: 3
Magnification: 5.0
☐ Show cross correlations

● Cross correlation ○ Fiducial markers ○ Load from file
☐ Save to file:
Post-processing history: Remove duplicates → Filter → Drift correction ☑
☑ Preview
Drift correction applied.

(b)

Figure I.12: Drift correction (a) xgraph with x drift going from positive to negative slope (b) x and y drifts monotonously decreasing

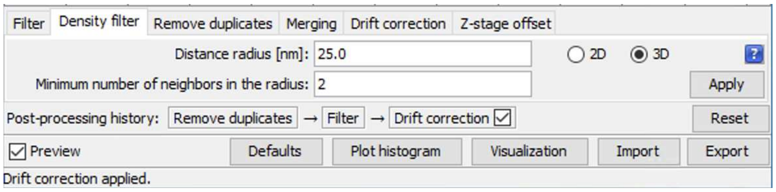

Distance radius [nm]: 25.0 ○ 2D ● 3D

Minimum number of neighbors in the radius: 2

Post-processing history: Remove duplicates → Filter → Drift correction ☑

☑ Preview

Drift correction applied.

Figure I.13: Density filter settings

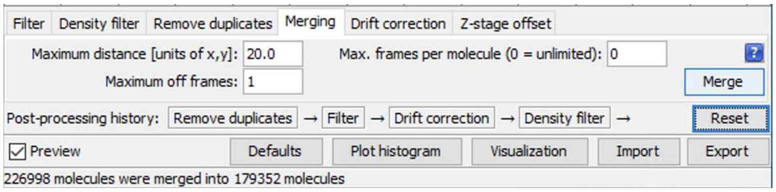

Maximum distance [units of x,y]: 20.0

Max. frames per molecule (0 = unlimited): 0

Maximum off frames: 1

Post-processing history: Remove duplicates → Filter → Drift correction → Density filter →

☑ Preview

226998 molecules were merged into 179352 molecules

Figure I.14: Merging of post processed data

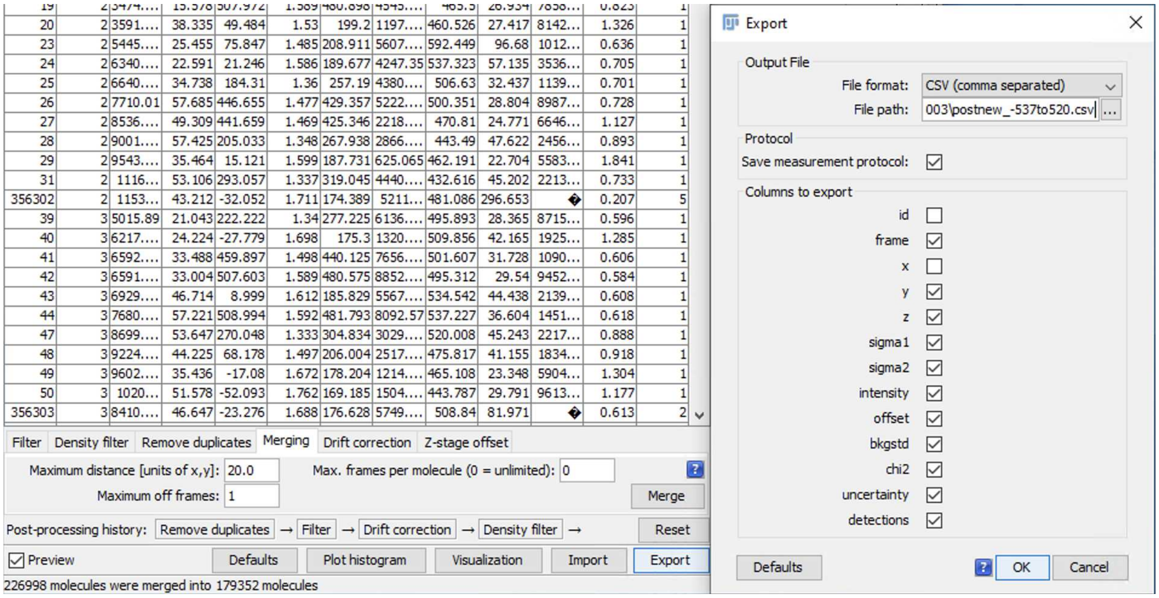

20	2	3591....	38.335	49.484	1.53	199.2	1197....	460.526	27.417	8142...	1.326	1
23	2	5445....	25.455	75.847	1.485	208.911	5607....	592.449	96.68	1012...	0.636	1
24	2	6340....	22.591	21.246	1.586	189.677	4247.35	537.323	57.135	3536...	0.705	1
25	2	6640....	34.738	184.31	1.36	257.19	4380....	506.63	32.437	1139...	0.701	1
26	2	7710.01	57.685	446.655	1.477	429.357	5222....	500.351	28.804	8987...	0.728	1
27	2	8536....	49.309	441.659	1.469	425.346	2218....	470.81	24.771	6646...	1.127	1
28	2	9001....	57.425	205.033	1.348	267.938	2866....	443.49	47.622	2456...	0.893	1
29	2	9543....	35.464	15.121	1.599	187.731	625.065	462.191	22.704	5583...	1.841	1
31	2	1116...	53.106	293.057	1.337	319.045	4440....	432.616	45.202	2213...	0.733	1
356302	2	1153...	43.212	-32.052	1.711	174.389	5211...	481.086	296.653	�	0.207	5
39	3	5015.89	21.043	222.222	1.34	277.225	6136....	495.893	28.365	8715...	0.596	1
40	3	6217....	24.224	-27.779	1.698	175.3	1320....	509.856	42.165	1925...	1.285	1
41	3	6592....	33.488	459.897	1.498	440.125	7656....	501.607	31.728	1090...	0.606	1
42	3	6591....	33.004	507.603	1.589	480.575	8852....	495.312	29.54	9452...	0.584	1
43	3	6929....	46.714	8.999	1.612	185.829	5567....	534.542	44.438	2139...	0.608	1
44	3	7680....	57.221	508.994	1.592	481.793	8092.57	537.227	36.604	1451...	0.618	1
47	3	8699....	53.647	270.048	1.333	304.834	3029....	520.008	45.243	2217...	0.888	1
48	3	9224....	44.225	68.178	1.497	206.004	2517....	475.817	41.155	1834...	0.918	1
49	3	9602....	35.436	-17.08	1.672	178.204	1214....	465.108	23.348	5904...	1.304	1
50	3	1020...	51.578	-52.093	1.762	169.185	1504....	443.787	29.791	9613...	1.177	1
356303	3	8410....	46.647	-23.276	1.688	176.628	5749....	508.84	81.971	�	0.613	2

Maximum distance [units of x,y]: 20.0

Max. frames per molecule (0 = unlimited): 0

Maximum off frames: 1

Post-processing history: Remove duplicates → Filter → Drift correction → Density filter →

☑ Preview

226998 molecules were merged into 179352 molecules

Output File

File format: CSV (comma separated)

File path: 003\postnew_-537to520.csv

Protocol

Save measurement protocol: ☑

Columns to export

id ☐

frame ☑

x ☐

y ☑

z ☑

sigma1 ☑

sigma2 ☑

intensity ☑

offset ☑

bkgstd ☑

chi2 ☑

uncertainty ☑

detections ☑

Figure I.15: Exporting post processed data

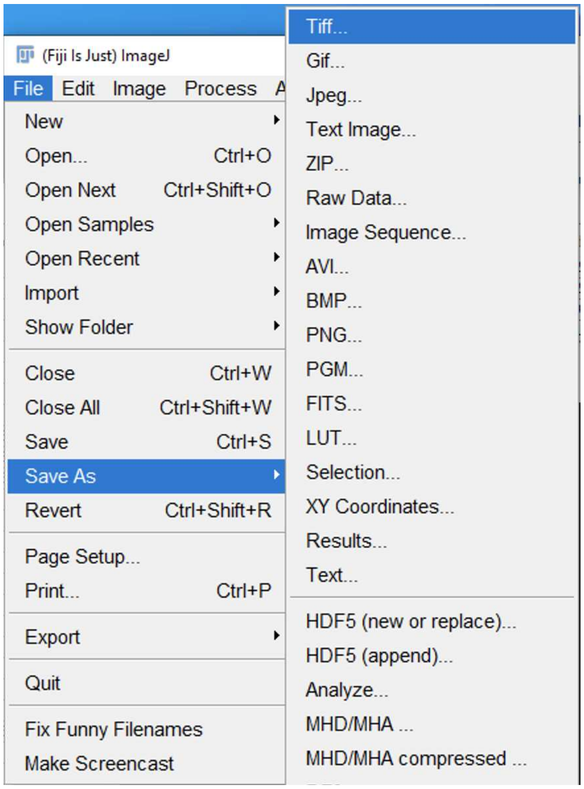

Figure I.16: Exporting post processed stack of data viewed as Normalized Gaussian as .tiff file

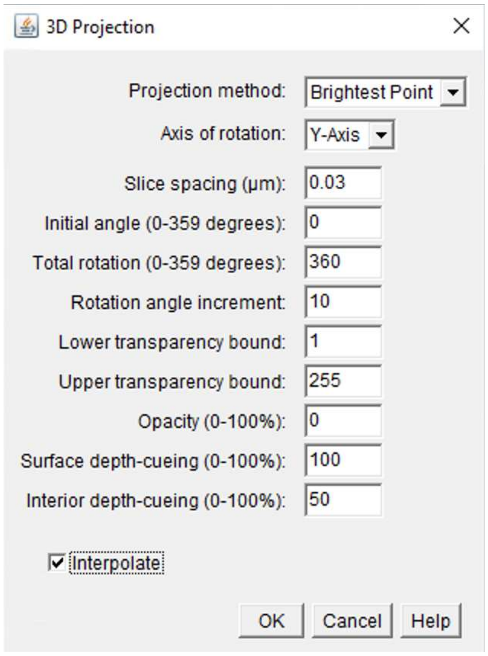

Projection method: Brightest Point

Axis of rotation: Y-Axis

Slice spacing (µm): 0.03

Initial angle (0-359 degrees): 0

Total rotation (0-359 degrees): 360

Rotation angle increment: 10

Lower transparency bound: 1

Upper transparency bound: 255

Opacity (0-100%): 0

Surface depth-cueing (0-100%): 100

Interior depth-cueing (0-100%): 50

☑ Interpolate

Figure I.17: 3D projection settings

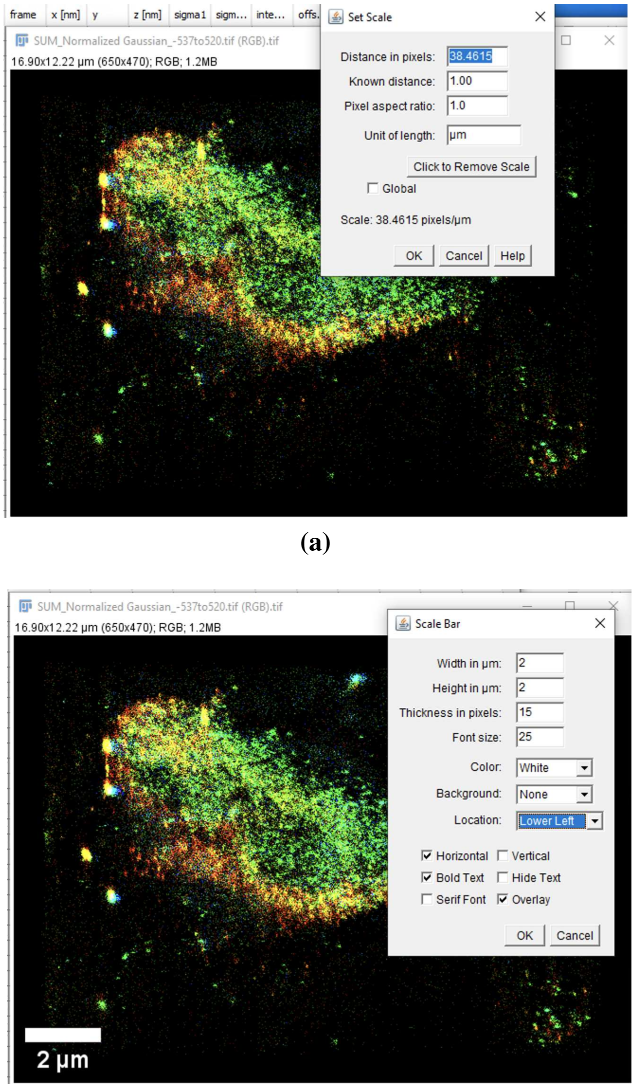

SUM_Normalized Gaussian_-537to520.tif (RGB).tif

16.90x12.22 µm (650x470); RGB; 1.2MB

Set Scale

Distance in pixels: 38.4615

Known distance: 1.00

Pixel aspect ratio: 1.0

Unit of length: µm

☐ Global

Scale: 38.4615 pixels/µm

(a)

SUM_Normalized Gaussian_-537to520.tif (RGB).tif

16.90x12.22 µm (650x470); RGB; 1.2MB

Scale Bar

Width in µm: 2

Height in µm: 2

Thickness in pixels: 15

Font size: 25

Color: White

Background: None

Location: Lower Left

☑ Horizontal ☐ Vertical

☑ Bold Text ☐ Hide Text

☐ Serif Font ☑ Overlay

(b)

Figure I.18: Adding scale bar (a) Setting scale parameters (b) Settings to place the scale bar